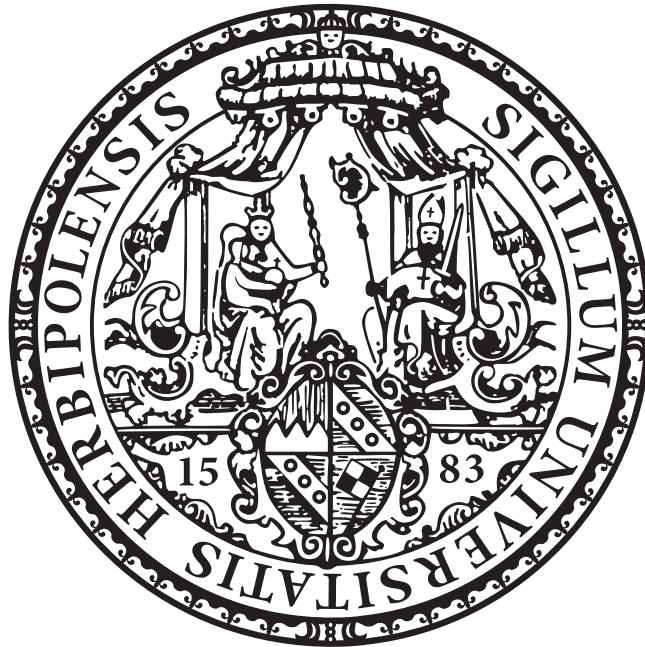


Transient Phenomena and Ionic Kinetics in Hybrid Metal Halide Perovskite Solar Cells

Dissertation zur Erlangung des
naturwissenschaftlichen Doktorgrades
der Julius-Maximilians-Universität Würzburg



vorgelegt von:
Mathias Fischer
aus Tuttlingen
Würzburg 2022



Eingereicht am: _____

bei der Fakultät für Physik und Astronomie

1. *Gutachter:* Prof. Dr. Vladimir Dyakonov

2. *Gutachter:* Dr. habil. Torsten E.M. Staab

3. *Gutachter:*

der Dissertation

Vorsizende(r): _____

1. *Prüfer:* Prof. Dr. Vladimir Dyakonov

2. *Prüfer:* Dr. habil. Torsten E.M. Staab

3. *Prüfer:*

im Promotionskolloquium

Tag des Promotionskolloquiums: _____

Doktorurkunde ausgehändigt am: _____

Contents

1. Introduction	1
2. Light harvesting with Hybrid Halide Perovskites	5
2.1. Physical properties of Perovskites	5
2.1.1. Crystall structure	5
2.1.2. Ion transport	8
2.1.3. Optoelectronic properties of perovskite semiconductors	11
2.2. Perovskites in photovoltaic applications	13
3. Concepts in light harvesting semiconductor devices	17
3.1. Working principle of a solar cell	17
3.2. Basic equations	18
3.2.1. Charge carrier density voltage relation	19
3.3. Mechanisms of thermal equilibration	21
3.3.1. Radiative recombination	22
3.3.2. Shockley-Read-Hall	23
3.3.3. Surface recombination	24
3.3.4. Diffusion	25
3.4. Current-Voltage characteristics	26
3.4.1. Detailed balance limit	28
3.4.2. Transient and Hysteresis properties	30
4. Methods	35
4.1. Materials	35
4.2. Device Preparation	39
4.3. Electrical device characterization techniques	43
4.3.1. Complex Impedance Spectroscopy	43
4.3.2. Open Circuit Voltage Decay	45
4.4. Drift-Diffusion simulations	49
4.4.1. Mathematical model	49

4.4.2. Courtiers numerical scheme	51
4.4.3. Implementation	55
5. Ionic contributions to capacitive space charge properties	63
5.1. Introduction	64
5.2. Mott-Schottky analysis	65
5.3. Capacitance profiling	72
5.4. Conclusion	74
6. Ionic Traces in Transient Open Circuit Voltage Decay	77
6.1. Introduction	78
6.2. Simulation Conditions	79
6.3. Open Circuit Voltage Dynamics	81
6.3.1. Ionic concentration measurement	88
6.3.2. Diffusivity measurement	92
6.4. Experimental factorization of the ionic conductivity	95
6.5. Conclusions	97
7. Summary	99
7.1. Zusammenfassung	100
Bibliography	103
Abbreviations	125
A. Publications and Conference Contribution	129
B. Danksagung	131

Introduction

1

The rise of renewable energies

The availability of abundant resources is an essential pillar on which modern societies are based. Therefore, the depletion of resources is accompanied by the disappearance of the cultures that depend on them, unless a substitute is found. The failure to sustainably manage existing resources is perhaps best illustrated by the example of Easter Island. Studying pollen contained in soil samples, it has been shown that the disappearance of the local high culture was accompanied by steady deforestation^[1], which follows the hypothesis that the inhabitants deprived themselves of their own means of subsistence^[2]. Cultures on Easter Island, which is less than 200 km² in size, were isolated from the rest of the world and, consequently, so were the ecological effects of their behavior. Today, in the 21st century, globalization has taken place and the scale of natural resource usage escalated to the point where the resulting environmental impacts are visible all over the world. Large-scale deforestation, especially of tropical forests, is only one part of a larger problem manifested in the symptom of global warming. The average global temperature has shown a rapid increase since the mid-20th century, caused mainly by large-scale anthropogenic emissions of carbon dioxide (CO₂) and methane (CH₄) into the atmosphere but also by other so-called greenhouse gases. These gases share the property of absorbing infrared light while being transparent to higher energy radiation such as visible light, allowing the earth's crust to absorb energy from the sun while preventing the emission of thermal radiation to space. This effect adds up to an increase in the earth's temperature, as already considered by Svante Arrhenius in 1896^[3]. Since then, the CO₂ concentration in the earth's atmosphere has increased by 46 % from 280 ppm^[4] to more than 410 ppm today^[5] and the CH₄ concentration shows a similar trend, accompanied by an increase in earth' surface temperature of ~ 1 °C^[6]. In response to the looming climate challenge, 191 of 197 member states have now ratified the so-called *Paris Agreement*, which aims to limit the global temperature increase to 1.5 °C degrees above pre-industrial levels.^[7] Food production and the energy sector, with mobility, electricity and heat as the most

important subsets, are often cited as the main drivers of this development. Most nations focus on the energy sector when it comes to reducing greenhouse gas emissions, as the use of technology is associated with fewer political consequences than regulations affecting everyone's personal habits such as food intake. In the expansion of new power plants, renewable energy sources such as wind and photovoltaics (PVs) were subsidized in particular and the resulting scale effects made them to the cheapest sources of electricity available today^[8,9]. Hence, even the poorest countries can aim for energy autonomy in the electricity sector. According to BP's Statistical Review of World Energy^[10] the global annual growth rate in renewable energy production from the 2008 - 2018 was on average $\sim 16\%$ indicating an exponential trend. In 2019, 10 EJ renewable energy was produced. The global primary energy consumption on the other hand was 590 EJ with an annual growth rate of 1.6%. Under the assumption of constant growth rates it is possible to transform the energy sector to purely renewable energy sources within 30 years. Such simple extrapolations however have to be taken with care, as they do not consider technological and fundamental thermodynamic limits.

State of photovoltaics

The fundamental upper efficiency limit of solar radiation conversion is given by thermodynamics in form of the Carnot efficiency of a heat engine and can simply be calculated from the temperatures of the environment (300 K) and solar radiation (6000 K) to 95%.^[11,12] At present, wind energy and photovoltaics are the main contributors to renewable electricity supply.^[10] From environmental, ecological and thermodynamic aspects photovoltaics may likely be superior over wind energy. The increasing harvesting of wind for human purposes already faces first fundamental limitations. It recently has been shown that wind farms can reduce the capacity of neighboring downwind farms by 20% or more, even if they are 40 km away from each other.^[13] This fact illustrates that there is only a limited pool of available wind energy that can be shared. On top of that, merely 0.7% of the absorbed solar radiation is indirectly converted into kinetic wind energy^[14] while the maximum possible conversion efficiency of a wind turbine is 60%^[15]. Therefore, the full process can surely be considered as inefficient. It is also important to note that rainfall and life forms such as plants also demand for wind energy in order to continue to exist and ultimately to ensure the food production of mankind. Although it is unlikely that a shortage of wind will actually become a real problem in the

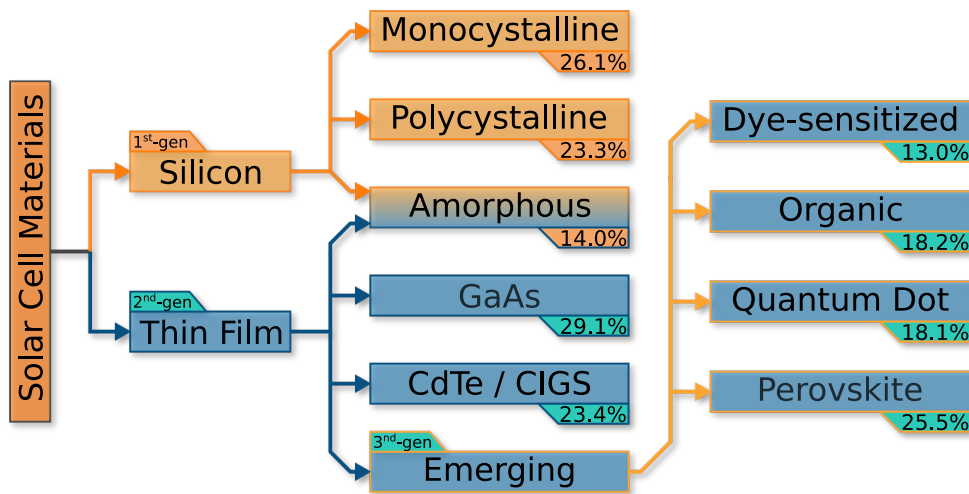


Figure 1.1.: Solar cell materials and their best research efficiencies provided by NREL^[16]

near future, it should be bared in mind that the same has been thought 100 yeas ago in the case of anthropogenic emissions of CO₂. From this perspective it would be better to aim for PVs which up to now is the technology with the best solar radiation to electrical powerpower conversion efficiency (PCE). However, solar cells as quantum converters are far from being perfect thermal engines and suffer from much more limitations. Accordingly, different materials and technological concepts are used, and sometimes combined, to extract the maximum power out of each photon.

An overview of established and emerging material systems is given in Figure 1.1, where material systems are divided into silicon (Si) based and thin film technologies. Since silicon is essential in the semiconductor device industry, its processing technologies have been industrialized and optimized on a large scale, which can be considered as a possible reason for its success and dominance in the PV market. The theoretical thermodynamic PCE of silicon (Si) is 32.3 %^[17], it may be lower depending on the exact band gap and technological details. The best Si-based solar cell achieves a PCE of 26.7% under 1 sun illumination and was built as heterojunction^[18], which illustrates that there is not much room left for improvement on a material basis. While in practice such efficiencies are quite sufficient, Si suffers from a comparably low absorption coefficient and usually needs to be about 100 μm thick to absorb all relevant solar radiation. Therefore, a variety of alternative material systems are being pursued in which a few 100 nm layer thicknesses are sufficient to absorb all relevant sunlight. These so-called thin-film technologies require only a fraction of the material input and thus promise lower material

costs.

Semiconductors that are well suited for thin film solar cells are gallium arsenide (GaAs), cadmium telluride (CdTe) and copper indium gallium (di)selenide (CIGS). Among these, epitaxial grown GaAs holds the record PCE among solar cell materials with 29.1 %^[8,16,19], but the hardly scalable manufacturing process and the rare gallium makes this material inherently expensive and thus is not considered as a material for large-area PV. Similar concerns about availability exist for indium and tellurium in the already commercially available CIGS and CdTe modules, which on the other hand makes them also attractive for recycling^[20].

The promise of abundant materials and scalable production have attracted attention to concepts called 3rd-generation solar cells. The first devices of this type use organic molecules to absorb sunlight, making them at least partially processible from solutions and thus usually even printable, with the absorber consisting only of abundant carbon, nitrogen, hydrogen and sulfur. They are divided into two branches with blurred boundaries, dye-sensitized solar cells (DSSCs) and organic photovoltaics (OPVs). Both concepts were first realized more than 30 years ago.^[21,22]

DSSCs have not seen much improvement in the last 25 years, so PCE is at a record 13 %^[16] so far. However, OPVs got a big boost from the replacement of fullerene-based electron acceptor materials with small molecules^[23,24] and have already overcome the 18 % barrier^[25]. The technology with the fastest progress in the last decade has been perovskite solar cells (PSCs). First introduced in 2009 with a PCE of 3.8 % in DSSCs, PSCs have emancipated technologically and can achieve high efficiencies with transport materials from both DSSCs and OPVs. Their previous PCE record is at 25.6 %^[26] and several companies have already started the commercialization of PSCs.

Outline of the thesis

This thesis aims for better understanding of device physicals aspects of PSCs and phenomena closely related to internal redistribution of ionic charge. In chapter 2 a generic overview over the fundamental properties of lead halide perovskite semiconductors and solar cells is provided. Chapter 3 accumulates the fundamental approximations and concepts relevant for experiments and device modeling as outlined in chapter 4.

Light harvesting with Hybrid Halide Perovskites

The aim of this chapter is to present the main physical features of perovskites. In the first part, structural properties are explained which are not only relevant for defect physics but also for the occurrence of ionic migration. In a further section, optoelectronic aspects and the application in solar cells are presented.

2.1 Physical properties of Perovskites

Originally, the term perovskite merely referred to the mineral calcium titanate (CaTiO_3) which forms a characteristic crystal structure. Since a variety of other material compositions have been found to share the same structural properties. Today, perovskites have gained a technological importance in a broad field of applications like high permittivity materials, piezo electrics^[27], superconductors^[28], gas sensors^[29] and of course semiconductors in solar cells. The reason for this wide range of applications lies in the remarkable crystal structure, which allows great flexibility and tunability of most material properties, making the structure essentially the only common property among the various perovskites so the word perovskite is commonly used to refer to the crystal structure only.

2.1.1 Crystall structure

Perovskites have a stoichiometry of ABX_3 . It adopts a crystal structure formed by B ions coordinated octahedrally with X ions. These octahedra are located at the corners of a cube enclosing a central A ion. A schematic illustration of the lattice is shown in Figure 2.1. The choice of A, B and X underlays two boundary conditions: overall charge neutrality and their size. The criterion of charge neutrality can be expressed as $q_A +$

$q_B + 3 q_X \stackrel{!}{=} 0$ with the ionic charges, also referred to as oxidation states, $q_{\{A,B,X\}}$ which can be achieved in many different ways. In case for the PV applications most relevant lead halide perovskites the halides oxidation state q_X equals one. This leads to the only possible ternary charge combination of $A^+Pb^{2+}[X^-]_3$. Because of the possibility for A^+ being an organic cation as in methylammonium lead iodide $[CH_3NH_3]^+Pb^{2+}[I^-]_3$, these kind of materials are often referred to as hybrid lead halide perovskites because they have both, organic and inorganic components.

Whether the size, or more precisely the ionic radii $r_{\{A,B,X\}}$ of the the individual constituents fit in a stable perovskite lattice can be estimated from the Goldschmidt tolerance factor t_G ^[30] and the octahedral factor μ_O ^[31]

$$t_G = \frac{r_A + r_X}{\sqrt{2} (r_B + r_X)} \quad (2.1) \quad \mu_O = \frac{r_B}{r_X}. \quad (2.2)$$

Values of $0.81 \leq t_G \leq 1.11$ and $0.44 < \mu_O < 0.90$ predict the formation of a stable halide perovskite lattice. For $0.81 < t_G < 1.0$, the formation of a highly symmetric cubic structure is expected, while for lower values tetragonal and orthorhombic variants occur.^[32]

The most important A cations for PV applications are methylammonium ($[CH_3NH_3]^+$, abbreviated MA^+ , $r_{MA^+} \approx 1.8 \text{ \AA}$), formamidinium ($[NH_2CH=NH_2]^+$, abbreviated. FA^+ , $r_{FA^+} \approx 1.9$ to 2.5 \AA) and caesium (Cs^+ , $r_{Cs^+} \approx 1.7 \text{ \AA}$). In high-efficiency cells, only lead(II) (Pb^{2+} , $r_{Pb^{2+}} \approx 1.8 \text{ \AA}$) is used as the cation B, but the replacement of Pb^{2+} by tin(II) (Sn^{2+} , $r_{Sn^{2+}} \approx 1.1 \text{ \AA}$) is still the subject of ongoing research. Possible anions X are chlorine (Cl^- , $r_{Cl^-} \approx 1.8 \text{ \AA}$), bromine (Br^- , $r_{Br^-} \approx 2.0 \text{ \AA}$) and iodine (I^- , $r_{I^-} \approx 2.2 \text{ \AA}$), although really only the latter two proved useful for PV applications.^[32-34]

However, the concept of an ionic radius is only an approximation in which the ions are treated as solid spheres occupying a certain volume in a lattice, and thus its exact value depends on the lattice and its symmetry. As the lattice expands with increasing temperature and lower pressure, so do the ionic radii, resulting in a change in the tolerance factor. Indicating that the crystal symmetry is subject to pronounced temperature- and pressure-dependent phase transitions.^[35-37] The exact temperature and pressure conditions of these phase transitions depend strongly on the exact material composition, which in principle can be an almost arbitrary alloy of the components listed in Figure

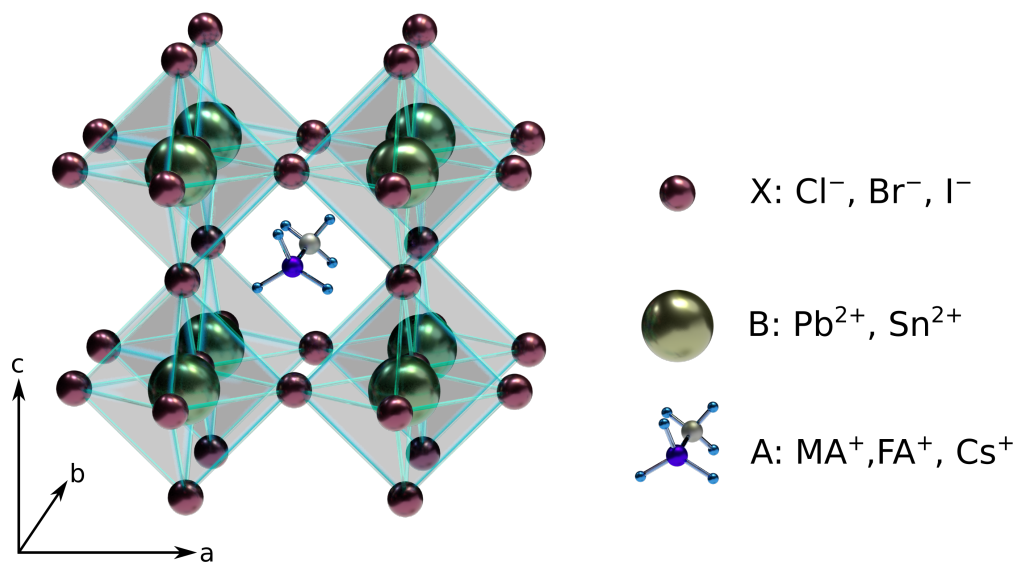


Figure 2.1.: Simplified illustration of the perovskite crystal structure. Depending on the temperature, the actual constituents and the final composition the lattice may be tilted resulting in a non cubic symmetry with different lattice constants along the directions a , b and c . The most relevant ionic components are listed on the right hand side of the figure. The relative size of the ions shown does not correspond to the actual proportions and has been adjusted for clarity.

2.1. Due to the extraordinary stability towards phase segregation these materials are also sometimes referred to as solid solutions.^[38–40] Pure compositions, in which A, B and X each consist of a single component and can thus be prepared in a very controlled stoichiometric manner, are therefore of particular importance from the point of view of a device physics. Accordingly, phase transitions and intrinsic electrical and optical properties are best studied for pure perovskites^[33], while high efficiency solar cells are nowadays almost exclusively made out of alloyed perovskites^[41]. The possibility to alloy the different constituents allows for tunable lattice constants and consequently a tunable band gap E_g as outlined in section 2.1.3. The archetypic methylammonium lead iodide MAPbI_3 shows a tetragonal symmetry at room temperature with the three lattice constants $a = b = 8.86 \text{ \AA}$ and $c = 12.66 \text{ \AA}$. It forms a cubic phase only at temperatures above 327 K with $a = b = c = 6.33 \text{ \AA}$, whereas its bromine based analog methylammonium lead bromide (MAPbBr_3) already forms such a cubic symmetry and a narrower crystal lattice with $a = b = c = 5.90 \text{ \AA}$ at room temperature.^[42,43] Another important feature of these perovskites is the possibility to substitute the A cation with a long chained amine. This makes it possible to hinder the formation of a 3D lattice and to obtain low-dimensional

2D, 1D or even 0D objects^[44,45]. These structures exhibit quantum properties that made them particularly interesting to use in light emitting diodes (LEDs), even before perovskites were found to be useful in PV applications^[46].

2.1.2 Ion transport

It was formally shown in 1983 that ion migration at room temperature in the halide perovskites CsPbCl_3 and KMnCl_3 occurs especially in the presence of electric fields.^[47] This, for semiconductors, exceptional property causes a variety of effects in all kinds of characterization techniques. In particular, a resulting anomalous current-voltage hysteresis makes even the simplest experiments, such as the determination of the correct PCE, a challenging task.^[48,49] As a result, much attention has been paid to ion migration in PSCs and many related phenomena. A huge dielectric constant at low frequencies^[50,51], light-induced halide segregation^[52], degradation^[53], and self-polarization^[54] are just a few examples of the variety of effects caused by ionic charge redistribution. Besides impurities, the common mechanism of ion migration in solid-state materials is lattice vacancy-mediated transport. Schottky and Frenkel defects are well-known manifestations of lattice vacancies. While vacancies in the form of Schottky defects imply a non-stoichiometric composition, Frenkel defects retain stoichiometry as interstitial ions leaving vacancies in the crystal lattice. Frenkel defects play a special role as they are an intrinsic material property ruled by thermodynamics and thus can be thermally excited.^[55] The existing vacancies in the lattice can now be filled by a neighboring ion, which in turn leaves a vacancy at its original position. In presence of a driving force, e.g. an electric field, this leads to a vacancy migration comparable to hole conduction in conventional semiconductors. As might be expected, ionic conduction occurs mainly at grain boundaries where numerous vacancies are inherently present.^[56] In addition, the solvation of ions can take place due to environmental influences such as moisture and act as an additional contribution to the ionic mobility.^[57,58] However, it can be shown that even in single crystals such an ionic contribution to the conductivity is present.^[59] Therefore, it is nowadays established that this phenomenon is an intrinsic material property, which occurs not only at grain boundaries but also in the volume.^[60–62]

Activation of ionic conductivity

The density of mobile ionic charge carriers N_{ion} is related to the vacancy formation energy E_{ion}^F , density of lattice and interstitial sites N_L and N_L' by Equation 2.3, with T and k_B to be the temperature and Boltzmann constant respectively.^[61] The final ability of the material to conduct ionic charge however is also ruled by the diffusivity D_{ion} of the respective ion specie. It is related to the diffusion constant D_{ion}^0 by the activation energy of diffusion E_{ion}^D as expressed in Equation 2.4

$$N_{ion} = \sqrt{N_L N_L'} e^{-E_{ion}^F/k_B T} \quad (2.3) \quad D_{ion} = D_{ion}^0 \cdot e^{-E_{ion}^D/k_B T} \quad (2.4)$$

The actual values of the respective activation energies depend strongly on the underlying migration pathways of the ionic species involved and may vary between crystal compositions and phases. Consequently, the equations 2.3 and 2.4 must be considered as approximations within a narrow temperature range.

Taking advantage of the classical Einstein relation, connecting mobility μ to a diffusion coefficient D by

$$D = \mu k_B T / q, \quad (2.5)$$

the ionic conductivity σ_{ion} can be rewritten from terms of an ionic mobility μ_{ion} as

$$\begin{aligned} \sigma_{ion} &= q \mu_{ion} N_{ion} = \frac{q^2 D_{ion} N_{ion}}{k_B T} \\ &= \frac{q^2 D_{ion}^0 \sqrt{N_L N_L'}}{k_B T} e^{-(E_{ion}^F + E_{ion}^D)/k_B T}, \end{aligned} \quad (2.6)$$

where all ions are assumed to carry only a single elementary charge q . It is clear from equation 2.6 that the knowledge of the temperature dependence of σ_{ion} alone is insufficient to reliably assign activation energies to an underlying diffusion or formation process as it can only measure the sum of both. Indeed, different ionic species may contribute to σ_{ion} via different migration pathways, each of which may have a specific E_{ion}^D or E_{ion}^F . The main paths of vacancy-mediated ion migration within the lattice are shown in Fig. 2.2 using MAPbI₃ as an example. The halide ion X has the shortest possible migration distance, namely the path along the PbX₆⁴⁻ octahedron (X1 and X2 in Fig. 2.2a and b). Its activation energy in MAPbI₃ was first calculated by Eames et al.^[62] using density

functional theory (DFT) to be $E_{ion}^D(X1) = 0.58$ eV. In this process, the paths X1 and X2 in Fig. 2.2b are not clearly distinguished. Other studies found significantly different activation energies for iodine vacancy migration in the 0.1 to 0.6 eV, which also varied between paths X1 and X2.^[63–66] The shortest migration paths for Pb^{2+} vacancies are within the BX plane of the crystal (B1 and B2 in Fig. 2.2b), calculated in the 0.8 to 2.3 eV and thus consistently too high to contribute to ion migration at room temperature.^[62,63,66] The E_{ion}^D of methylammonium (cation) (MA or MA^+) cation vacancy migration determined in several DFT studies are in the range of 0.5 to 0.84 eV (path A in 2.2c), and thus between the activation energy of iodine and lead ion vacancy diffusion.

The partly wide spread in DFT calculated values of E_{ion}^D likely originates from the

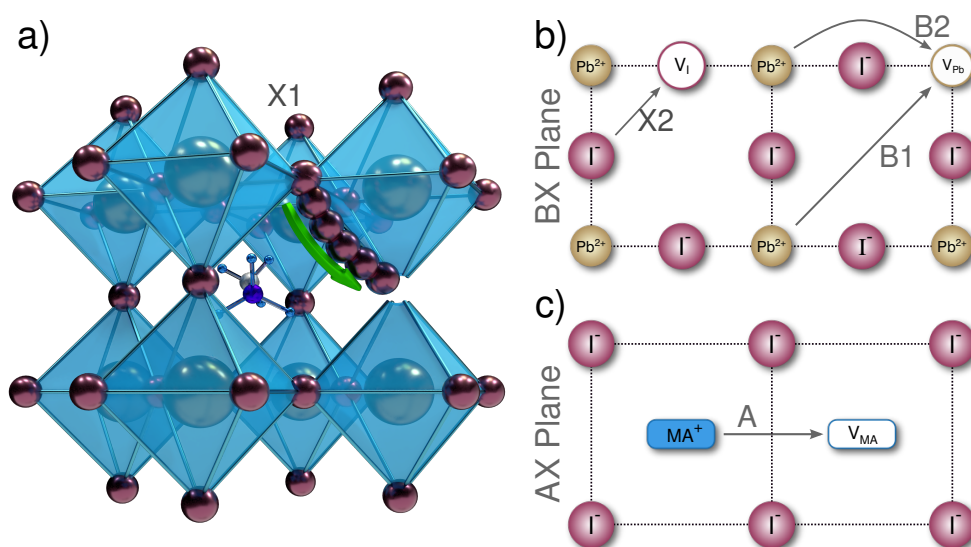


Figure 2.2.: Illustration of vacancy mediated ion movement in example of MAPbI₃. **a)** I⁻ migration along the corner of a PbI₆⁴⁻ octahedron (X1). **b)** Movement within the crystals BX plane (<110> direction). I⁻ can jump into a nearby vacancy V_I along X2, Pb²⁺ can fill a lead vacancy V_{Pb} via the paths B1 and B2. **c)** MA⁺ migration along path A within the AX plane.

complexity introduced by the organic MA cation which is not symmetric regarding rotations. As a result the lattice constants are dispersed due to orientation of the MA⁺ dipole and presence of vacancies.^[34,67] As DFT can only be computed efficiently on relatively small grids, semi empirical corrections are often applied in order to render such dispersions.^[34] In addition, the vast number of possible ionic migration mechanisms makes it extremely challenging from an experimental point of view to observe a theoretically proposed ionic migration mechanism in isolation. Thus, most experimental studies

are satisfied with the determination of the activation energy of the ionic conductivity and the assignment of the involved ionic species, for instance by comparing different material compositions.^[68–72] By combining the theoretical and experimental studies, it can be considered certain that halide migration is the main driver of ion migration in lead halide perovskites.

2.1.3 Optoelectronic properties of perovskite semiconductors

Excitonic properties

Although perovskites for photovoltaic applications made their debut in dye-sensitized solar cells, the mechanism underlying charge transport and extraction is similar to the band transport of free charge in classical semiconductors^[73]. While in organic and dye-sensitized solar cells absorbed photons mainly create excitons which have to be split afterwards^[74,75], excitonic properties are only found in perovskites at low temperatures, high E_g , or with very specific, mostly fully inorganic, material compositions of low dielectric constant^[76]. In MAPbI₃ the exciton binding energy was determined to be far below 20 meV in the tetragonal phase at room temperature^[76–80], which makes it reasonable to assume that excitons are not present in metal organic halide perovskites under operation conditions where the thermal energy is much higher ($k_B T \approx 25.7$ meV at $T = 300$ K). The inorganic counterparts however don't share this property and reveal quite high exciton binding energies ((103 ± 8) meV in CsPbI₃^[81]). The circumstance that all efficiency records were achieved only with perovskites containing mainly organic cations is largely due to the fact that the charge carriers are already separated at the time of generation due to the low exciton binding energies. In the case of organic solar cells, energy must first be applied to separate the excitons, which subsequently makes it unavailable as electrical energy resulting in a reduced PCE.

Band structure

Essentially all lead halide perovskites show a direct band gap. For MAPbI₃ a value slightly varying around $E_g = (1.60 \pm 0.05)$ eV can be found in literature^[42,82–84]. As already hinted in section 2.1.1 the E_g can be tuned by the material composition. The

material composition and the band gap are connected by the lattice spacing as visualized on figure 2.3.

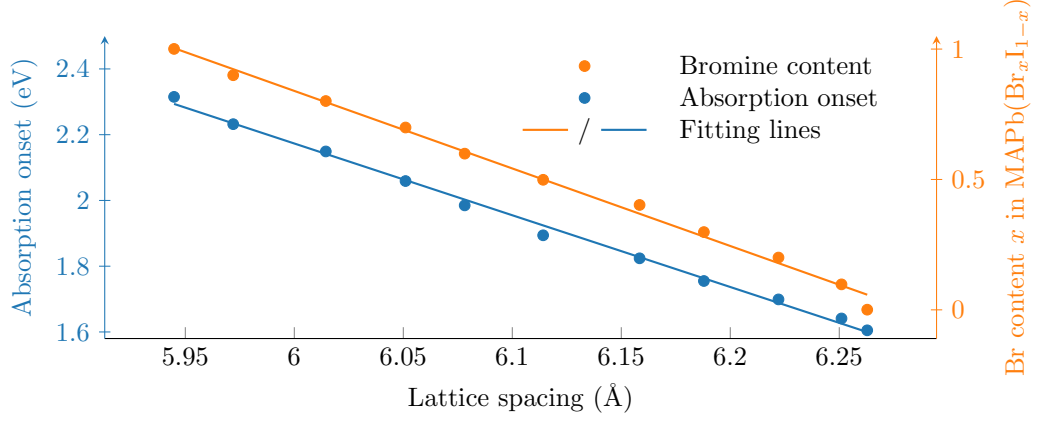


Figure 2.3.: Correlation of the absorption onset energy (approximate E_g) and composition with the lattice spacing in [200] direction, compiled from data provided by Hocke et al.^[52]. The direct connection between absorption onset energy, bromine content and the lattice spacing is clearly visible.

Besides the band gap energy the dispersion relation $E_{e/h}(k)$ of the conduction band (CB) / valence band (VB) are also characterized by their curvature in k space, precisely the second derivative of the energy at the minimum / maximum, which defines the effective mass of electrons (m_e^*) and holes (m_h^*) according to Equation 2.7.

$$m_{e/h}^* = \hbar^2 \left(\frac{\partial^2 E_{e/h}(k)}{\partial k^2} \right)^{-1}, \quad (2.7) \quad m_{eff}^* = \sqrt{m_e^* m_h^*}, \quad (2.8)$$

where \hbar is the reduced Plank's constant. Nowadays many studies regarding the actual value of $m_{e/h}^*$ are available. From a theoretical perspective, the effective masses can be directly derived from DFT calculations for each energy band individually. The experimentalists however are often restricted to statements about single bands or a joint effective mass m_{eff}^* according to Equation 2.8 as the individual masses are difficult to measure directly. In summary, the vast majority of findings can be condensed in to the statement that $m_{eff}^* \approx m_e^* \approx m_h^* \approx (0.2 \pm 0.05) m_0$ ^[82,85-88], where m_0 is the free electron mass. Only slight deviations can be found depending on the actual crystal phase

and material composition.

The band structure of lead halide perovskite is almost exclusively formed by the lead (Pb^{2+}) and halide ions. In case of MAPbI_3 the $\text{Pb}(6s)\text{-I}(5p)$ σ -antibonding orbital is thereby responsible for the VB maximum, where approximately 70% of the density of states (DOS) originate from the $\text{I}(5p)$ orbitals^[89] and is located 5.3 to 5.46 eV below the vacuum level^[90,91]. The CB minimum is formed by $\text{Pb}(6s)\text{-I}(5p)$ orbitals^[89,92] with a energy of 3.7 to 3.86 eV below the vacuum level^[90,91]. The organic MA cations form σ bonds deep in the valence band, so their contribution is restricted to structural interactions and it is meanwhile common ground that the electronic properties originate largely from the $[\text{PbI}_6]^{4-}$ octahedrons. Nevertheless can disorder caused by thermal fluctuations of the cation orientation result in a deformation of the $[\text{PbI}_6]^{4-}$ cage, leading to different positions and curvature of the CB minimum / VB maximum and even to a slightly indirect band gap of 1.6 eV^[90,93,94]. Accordingly, the role of the organic cation can not be fully neglected. Indirect band gaps however also attributed to spin orbit coupling induced Rashba splitting^[95-97]. There are also concerns that the disordered nature of the MA dipoles suggest that spin orbit coupling is not a dominating effect.^[97] Accordingly, there is still an ongoing discussion if and to what extend such slightly indirect band gaps, 60 meV below the direct transition^[96], would be relevant under operation conditions. Additionally, these indirect valleys in band energies are relatively close to the direct transition in k space so these effects are considered to be rather small any way.

2.2 Perovskites in photovoltaic applications

Perovskite solar cells consist out of a stack of different layers. Each of these layers fulfill a special purpose which in the end allows for an efficient light to electricity conversion. The quantity of published transport materials suitable for the fabrication of PSCs is hard to keep track of, even for experts.^[98] The most generic device configuration is depicted in Figure 2.4. Up to now all devices use a glass substrate coated with a transparent conductive oxide (TCO) layer of approximately 100 nm thickness. It serves as bottom electrode which has to be electrically conductive and transmissive for light at same time.

Not many materials share such a property and indium tin oxide (ITO) as well as fluorine doped tin oxide (FTO) are the only relevant materials applied for this purpose in commercialized technology. Thereby the former is more common while the latter shows better chemical, mechanical and thermal stability^[99] where both can be used in PSCs. For the top electrode a metal is applied, as besides of good electrical conductivity it also reflects transmitted photons back to the absorbing perovskite layer. The main difference of PSCs to classical solar cell devices is that instead of doping the perovskite, selective transport layers are applied to separate generated holes from the electrons. This concept was adopted from the OPV and dye sensitized solar cells and effectively circumvented fundamental problems when it comes down to perovskite doping and homo junctions^[100].

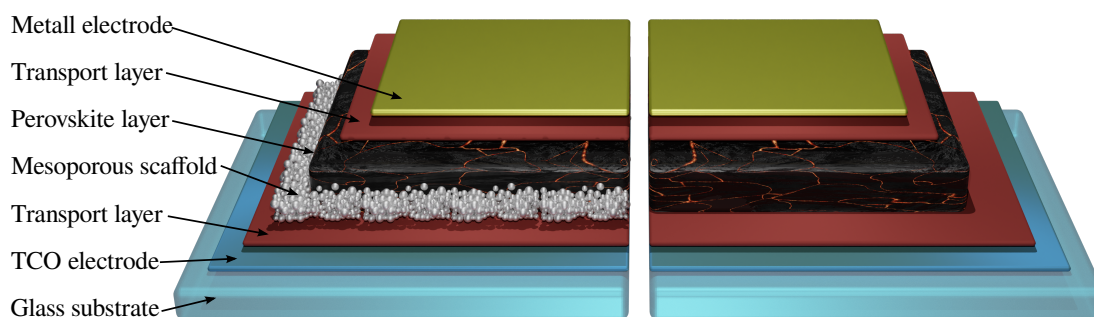


Figure 2.4.: Generic representation of the two most important device configurations used for PSCs. They they split up in *mesoporous* (left) and *planar* (right) configurations.

Another concept originally developed in the context of dye sensitized solar cells is the application of a mesoporous metal oxide layer, which is used to increase the surface area supporting separation of low mobility charge carriers^[101]. The purpose of this layer in PSCs lies more in its contribution to a good film morphology rather than to actual charge separation and transport^[84]. Consequently, a PSC can also be built fully without such mesoporous layers in a so called *planar* configuration. If the metal or the TCO electrode acts as anode or cathode is defined by the choice of the transport layers. The arrangement where the TCO acts as cathode/anode is referred as n-i-p/p-i-n configuration. Which of these is used, often depends on the experience available with the materials in the respective laboratories. The material most commonly used in n-i-p devices is titanium dioxide (TiO_2) as a compact layered electron transport material (ETM) with the mesoporous scaffold also made out of TiO_2 on top. The processing of these layers is a quite complicated and challenging process and is exclusively performed on FTO

electrodes as this material, in contrast to ITO, is capable of handling the 400 to 500 °C needed for the high temperature pyrolysis and sintering steps during the preparation of these layers.

The scaffold then is infiltrated and capped with perovskite as light absorber material. The organic molecule abbreviated with spiro–MeOTAD is among the most frequently used hole transport layer (HTM) materials in n-i-p devices. Finally, a gold electrode serves as anode, but other metals are also possible but often subject to irreversible chemical reactions, especially with the halogenide ions diffusing out from the perovskite layer. Different materials are used for solar cells in p-i-n configuration where the TCO electrode acts as anode. In principle, nickel oxide can be used as HTM^[102,103] and it is also possible to create a mesoporous scaffold out of this material^[102]. However, most progress in the performance of p-i-n devices was made with (poly)triaryl amine based organic semiconductors instead of the metal oxides by complete absence of a mesoporous layer. As ETM, a stack of blocking layers and fullerene based acceptors is used, because the sintering steps needed for the fabrication of a TiO₂ layer makes it hardly possible to process this material on top of already fabricated perovskite. Another reason why transport layers can not simply be flipped between n-i-p and p-i-n configurations is that PSCs are usually solution processed and therefore the whole process relies on the use of orthogonal solvents for consecutively deposited layers as outlined in section 4.2.

Concepts in light harvesting semiconductor devices

This section features the essential physical connections in semiconductor diodes and provides a comprehensive description of the functionality of a solar cell as foundation for modeling (see chapter 4.4). The relationships between internal parameters, such as charge carrier density and recombination rates, along with external ones, like the current density and voltage, is put into perspective.

3.1 Working principle of a solar cell

Solar cells convert light into electrical energy by means of the photovoltaic effect. The mechanism is based on the principle that light can be regarded not only as an electromagnetic wave but also as quantized energy packages, which are called photons in this context. Each of these photons can be assigned a specific energy

$$E_{ph} = h \frac{c}{\lambda}, \quad (3.1)$$

which depends on the wavelength λ and speed c of the light λ and Planck's constant h .^[104] Even if this connection, explained by Albert Einstein in 1905^[105], may not seem very profound, the opposite is actually the case and brought him 1921 the Nobel Prize in physics.

A solar cell is simply a device that facilitates the energy contained in the photon to be harnessed in an electrical form. This conversion can be divided into basic steps depicted in Figure 3.1, which will be discussed in the following. The process starts with the absorption of a photon (Fig. 3.1①), this way an electron in the VB is excited to a higher energetic state in the CB. Such an excited electron always generates a positively charged hole in the VB, the process is also referred to as charge carrier generation. For absorption to take place in an ideal semiconductor, the photon energy must correspond to the

energetic distance $E_c - E_v$ between two energetic states, the band edges of the CB and VB. This distance also defines the band gap E_g . If the photon energy is greater than E_g , the excess is transferred by thermalization to the semiconductor material (Fig. 3.1②), which consequently heats up. Since there are ideally no available energy states with energies between E_c and E_v , the semiconductor is transparent for photons with $E_{ph} < E_g$. By using selective materials for only one type of charge carrier as an electrode, it is possible to extract holes separated from electrons (Fig. 3.1③), thus the solar cell is building up voltage upon exposure to light. If for some reason this extraction is too slow or not effective enough, the generated charge carriers will recombine before being separated and energy harvesting is not possible (Fig. 3.1④).

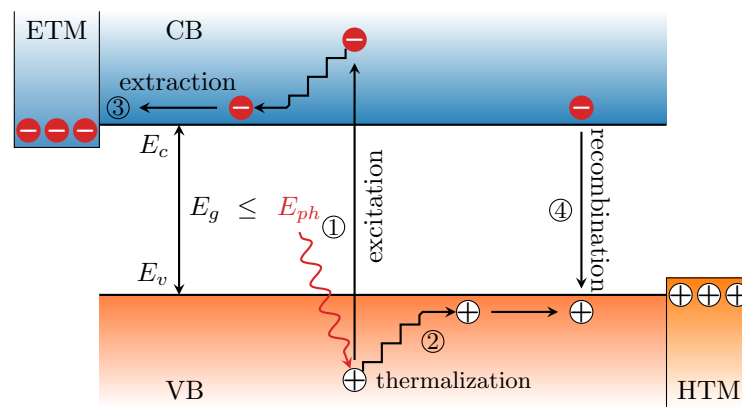


Figure 3.1.: Illustration of the basic processes in a solar cell of the band gap E_g . ① A photon of the energy E_{ph} excites an electron into the conduction band of the energy E_c and leaves a hole. ② Excess energy is thermalized. ③ Charge is extend by selective layers. ④ If the charge extraction is not effective enough, the excited charge carriers recombine.

3.2 Basic equations

The main equations for describing the static and dynamic behavior of solar cells under external influences, such as the application of a voltage or optical excitation, are presented in the following. These external perturbations are always to be understood as a displacement of the internal charge carrier density out of its thermal equilibrium. The way back to equilibrium is described in terms of the material properties by a set of partial

differential equations which describe the electrostatic interactions of the charge carriers among each other, as well as their spatial and temporal change in number.

3.2.1 Charge carrier density voltage relation

The overall kinetics in a solar cell is determined by the prevailing charge carrier density in the different layers of the solar cell. Every semiconductor in thermal equilibrium has a certain density of free electrons n_0 and holes p_0 in their respective energy bands. For intrinsic semiconductors they are equal to the intrinsic carrier density $n_i = n_0 = p_0$. The origin of n_i is found in the thermal excitation of electrons in the VB to the CB. Electrons are fermions, hence their probability to occupy a certain state of energy E is given by the Fermi-Dirac distribution.

$$f(E, T) = \frac{1}{e^{(E-E_F)/k_B T} + 1} \stackrel{E-E_F \gg 2k_B T}{\approx} e^{-(E-E_F)/k_B T}. \quad (3.2)$$

The approximation made in here is typically conducted for intrinsic or weakly doped semiconductors where the Fermi level E_F is close to the center of the band gap and thus several $k_B T$ away from the band edge. The Fermi level, also known as chemical potential, marks the energy at which a state is occupied with probability $f(E_F, T) = 1/2$ and can be interpreted as the energy needed to remove one electron from the system. In order to find an answer to the question how much charge carriers are located in a certain energy band the number of available states $g_{C/V}$ in the CB/VB has to be integrated over their probability of occupation $f(E, T)$. For the parabolic dispersion of a three-dimensional electron gas with 2-fold spin degeneracy the density of states is a function of energy: [55,106]

$$g_{C/V}(E) = \frac{1}{2\pi^2} \left(\frac{2m_e^*}{\hbar^2} \right)^{3/2} \sqrt{E}. \quad (3.3)$$

Together with the Boltzmann approximation in Equation 3.2 it allows for an analytical solution of the resulting integrals for the carrier densities in thermal equilibrium

$$n_0 = \int_{E_C}^{\infty} g_C(E) f(E) dE \quad (3.4) \quad \text{and} \quad p_0 = \int_{-\infty}^{E_V} g_V(E) f(E) dE, \quad (3.5)$$

where E_C / E_V is the energy of the CB/VB minimum / maximum. The result allows to

express the equilibrium carrier concentration via an effective density of states N_C / N_V for the CB/VB, which shows a slight temperature dependence

$$n_0 = 2 \left(\frac{2\pi m_e^* k_B T}{h^2} \right)^{3/2} e^{(E_F - E_C)/k_B T} = N_C \cdot e^{(E_F - E_C)/k_B T} \quad (3.6)$$

$$p_0 = 2 \left(\frac{2\pi m_h^* k_B T}{h^2} \right)^{3/2} e^{(E_V - E_F)/k_B T} = N_V \cdot e^{(E_V - E_F)/k_B T}. \quad (3.7)$$

The N_C and N_V are the numbers of effectively available states at the thermal energy present. An important observation at this point is that the product of Equation 3.6 and 3.7 results in a mass action law which connects the intrinsic carrier concentration to the band gap $E_g := E_V - E_C$

$$n_i^2 = n_0 \cdot p_0 = N_C N_V \cdot e^{-E_g/k_B T}, \quad (3.8)$$

and is independent of E_F . The ratio between N_C and N_V rules the position of E_F in undoped semiconductors as it follows from the condition $n_0 = p_0$ by rearranging Equation 3.6 and 3.7 to

$$E_F = \frac{1}{2}(E_V + E_C) + \frac{1}{2}k_B T \ln \left(\frac{N_V}{N_C} \right). \quad (3.9)$$

Although Equation 3.6 and 3.7 refer to the thermal equilibrium, the generic derivation via 3.4 and 3.5 can also be used in the unequilibrated context, where a voltage or exposure to light is present. This way the so called quasi Fermi level (QFL) for electrons E_{Fn} and holes E_{Fp} are defined, relating N_C and N_V to the total electron n and hole p densities

$$n = N_C \cdot e^{(E_{Fn} - E_C)/k_B T} \quad (3.10) \quad \text{and} \quad p = N_V \cdot e^{(E_V - E_{Fp})/k_B T}. \quad (3.11)$$

In this case the $n \cdot p$ product stays a function of the respective Fermi levels. The quasi Fermi levels represent the energy needed to remove a charge carrier from the system when it is out of equilibrium. This allows to rearrange the product of Equation 3.10 and 3.11 and write the energy needed to remove an electron and inserting it into the position of a hole

$$E_{Fn} - E_{Fp} = E_g + k_B T \ln \left(\frac{np}{N_C N_V} \right) \geq qV. \quad (3.12)$$

This corresponds to the maximum energy that can be extracted from a charge carrier in a solar cell^[107] and is called quasi Fermi level splitting (QFLS). Ideally, the $n \cdot p$ product is constant along the active layer of the solar cell and thus sets the voltage V measurable at outer contacts. However, real devices often suffer from additional losses near the interface of different layers resulting in a lower voltage measurable externally at the electrodes^[108,109]. It has to be kept in mind that Equation 3.12 is only valid as long as the (quasi) Fermi level is not close to the band edge ($N_C > n$ or $N_V > p$). Otherwise a more accurate estimate of the (quasi) Fermi levels for parabolic bands is available^[106,110]

$$E_{Fn} - E_{Fp} \approx E_g + k_B T \left[\ln \left(\frac{np}{N_C N_V} \right) + 2^{-3/2} \left(\frac{n}{N_C} + \frac{p}{N_V} \right) \right] \quad (3.13)$$

but almost never relevant under solar cell operation conditions. In many cases, only the additional charge carriers that are present in addition to the intrinsic ones are of relevance. The so called excess charge carrier densities can be calculated by rewriting Equation 3.12 while taking advantage of Equation 3.8 to

$$np - n_i^2 = n_i^2 \left(e^{(E_{Fn} - E_{Fp})/k_B T} - 1 \right) \approx n_i^2 \left(e^{qV/k_B T} - 1 \right). \quad (3.14)$$

3.3 Mechanisms of thermal equilibration

The time frame it takes for an excited semiconductor to go back into its thermal equilibrium is primarily characterized by a specific rate, which strongly depends on the mechanism of equilibration. In that regard, excess charge carrier recombination with its rate R can be seen as the most important process, as it is partly an intrinsic process and therefore fundamentally unavoidable. However, it can be separated into different recombination mechanisms which are illustrated in Figure 3.2. Depending on the prevailing charge carrier density, material quality, band structure and device configuration, some processes may dominate over others. The aim of this section is to give a brief overview of the most commonly observed processes.

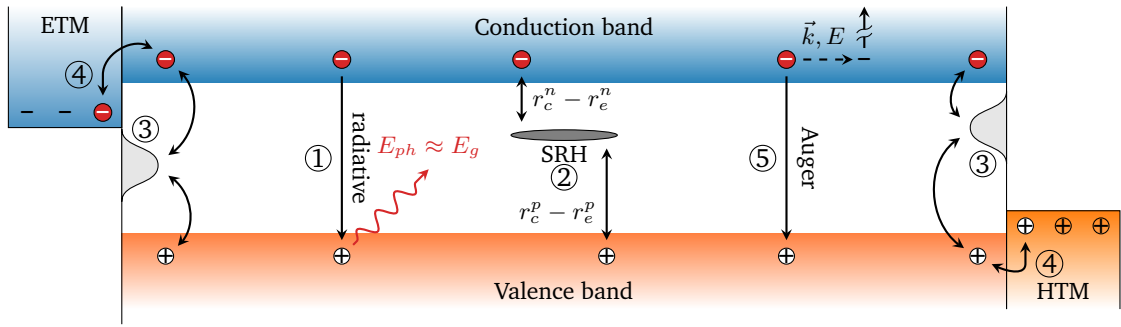


Figure 3.2.: Overview of important recombination mechanisms in semiconductors. Unavoidable radiative recombination ① of an electron-hole pair releases a photon where E_{ph} is ruled by the band gap. At low carrier concentrations this process is usually ruled out by trap assisted Shockley-Read-Hall recombination ②, where the recombination rate is set by the net emission and capture rates. This process is especially relevant at material interfaces and is used to model surface recombination ③. The charge carrier densities on both sides of the interface underlie a *detailed balance* ④. Auger recombination ⑤ becomes relevant at high carrier densities as a three particle process in which momentum and energy are conserved.

3.3.1 Radiative recombination

As the inverse process of optical band to band absorption, radiative recombination is not only inevitably present in a semiconductor out of its thermal equilibrium, it is also directly coupled with the absorption coefficient of the material. Such a recombination event (Fig. 3.2①) demands the presence of an electron and a hole at the same time. Consequently, the probability for a recombination event is the product of the probability of a hole and an electron being at a common location times a prefactor. This results in an expression for the radiative recombination rate

$$R_{rad}^* = k_{rad} \cdot np, \quad (3.15)$$

introducing the radiative rate constant k_{rad} . As long as this is the only recombination process present R_{rad}^* must match the thermal generation rate G_{th} in thermal equilibrium and $R_{rad}^* = G_{th} = k_{rad} \cdot n_0 p_0 = k_{rad} \cdot n_i^2$ holds. Finally, the radiative excess carrier recombination rate can be written as

$$R_{rad} = R_{rad}^* - G_{th} = k_{rad} \cdot (np - n_i^2). \quad (3.16)$$

In an intrinsic semiconductor where $n = p$, radiative recombination scales with $\mathcal{O}(n^2)$, this is a second order recombination process. A direct semiconductor has typically more than 4 orders of magnitude higher values of k_{rad} than indirect ones, where band-to-band transitions are limited by temperature. The true value of k_{rad} in metal halide perovskites is still under debate as the high absorption coefficient, a comparably sharp band edge and light trapping makes reabsorption of emitted photons very likely^[111,112], thus only a fraction of the occurring recombination events can be detected externally. As a result, the externally measured k_{rad}^{ext} ($(1.0 \times 10^{-11}$ to $4.8 \times 10^{-11}) \text{ cm}^3 \text{ s}^{-1}$ for MAPbI₃) appears to be lower than the rate present internally k_{rad}^{int} ($(2.0 \times 10^{-10}$ to $9.4 \times 10^{-10}) \text{ cm}^3 \text{ s}^{-1}$ for MAPbI₃).^[85,113,114] This so called photon recycling mechanism results in an out coupling of only 6 % of the internally generated photons^[85] and can be considered as beneficial for a high PCE in solar cells^[111] but are of less relevance if other recombination mechanisms become dominant^[113].

3.3.2 Shockley-Read-Hall

The Shockley-Read-Hall (SRH) recombination models a recombination mechanism in presence of a single energetic trap state in between the band gap, which can trap and emit charge carriers (Fig. 3.2②). It is derived from treating the processes of emission $r_e^{n/p}$ and capture $r_c^{n/p}$ of holes and electrons as statistically independent.^[115,116] The trap state of energy E_t is characterized by its volume density N_t and capture cross sections for electrons σ_n and holes σ_p with thermal velocity ν_{th} . The recombination rate for this process is given by the net transition rate and reads

$$R_{SRH} = \frac{\sigma_n \sigma_p \nu_{th} N_t \cdot (np - n_i^2)}{\sigma_n \left[n + n_0 \exp\left(\frac{E_t - E_i}{k_B T}\right) \right] + \sigma_p \left[p + p_0 \exp\left(\frac{E_i - E_t}{k_B T}\right) \right]}. \quad (3.17)$$

When an energetic distribution of trap states $N_t(E_t)$ is assumed, integration over E_t is needed. However, strictly speaking, this negates a possible charge exchange within among the traps which are energetically and spatially close to each other.^[117] Similar as in Equation 3.16, it is proportional to the excess carrier density $np - n_i^2$ where the sign determines whether generation or recombination takes place. As the expression for the SRH recombination rate has many free parameters, commonly some approximations

are made. By assuming that the trap is close to the center of the band gap ($E_t \approx E_i$), Equation 3.17 reads

$$R_{SRH} = \frac{np - n_i^2}{\tau_p n + \tau_n p + \kappa}, \quad (3.18)$$

where $\tau_{n/p} = 1/\sigma_{n/p}\nu_{th}N_t$ is the electron or hole life time, respectively. The term $\kappa = (\tau_p n_0 + \tau_n p_0)$ is usually negligibly small under forward bias conditions where $n \gg n_0$ and $p \gg p_0$ and thus can be safely ignored in most cases. In intrinsic semiconductors, this process scales with $\mathcal{O}(n)$ implying that it will be dominated at high carrier concentrations by second order processes like radiative recombination. However, it is worth having a look on the edge case where $E_t - E_i \gg k_B T$ by approximating $\sigma_n \approx \sigma_p \approx \sigma$ and $n_0 \approx p_0 \approx n_i$ simplifying Equation 3.17 to

$$R_{SRH} = \frac{\sigma\nu_{th}N_t \cdot (np - n_i^2)}{n + p + 2n_i \cosh\left(\frac{E_t - E_i}{k_B T}\right)} \stackrel{|E_t - E_i| \gg k_B T}{\approx} \frac{\sigma\nu_{th}N_t \cdot (np - n_i^2)}{2n_i \cosh\left(\frac{E_t - E_i}{k_B T}\right)}. \quad (3.19)$$

It becomes clear that for trap energies far off from the mid gap energy this becomes effectively a second order process ($\mathcal{O}(n^2)$) in intrinsic semiconductors. However, it also requires large N_t and σ in order to become dominant over the radiative recombination process and therefore usually is not considered to be relevant in perovskites.

3.3.3 Surface recombination

Surface recombination describes an often increased recombination rate at material interfaces. This phenomenon can be attributed to material stress and an increased number of lattice defects due to dangling bonds at this location, leading to a large number of trap states (Fig. 3.2③). When using organic transport layers, the penetration of minority carriers into a transport layer of poor selectivity can also be approximated by surface recombination, since the minority carriers recombine very quickly with the majority charge in such doped layers and therefore won't travel further than a few nanometers in to the transport layer. Accordingly a two dimensional surface trap density N_t^* is assumed and Equation 3.18 is rewritten to

$$R_{sur} = \frac{\overleftarrow{n} \overrightarrow{p} - n_i^2}{\overleftarrow{n}/v_p + \overrightarrow{p}/v_n + \kappa^*}, \quad (3.20)$$

where $v_{n/p} = \sigma_{n/p} \nu_{th} N_t^*$ is the electron or hole surface recombination velocity and $\kappa^* = (n_0/v_p + p_0/v_n)$. The R_{sur} has to be considered different at the HTM and ETM interface because of different trap densities leading to different values of ν_n and ν_p . The \leftarrow/\rightarrow indicate that the quantities on the left and right side of a ETM/Perovskite or a Perovskite/HTM interface have to be evaluated.

3.3.4 Diffusion

In many cases, the fastest way to bring a diode to thermal equilibrium is to externally short-circuit the anode and cathode. In this case, the time required for reaching thermal equilibrium is essentially determined by the diffusion process of electrons and holes. Until now, the charge carrier densities were considered to be uniformly distributed in space. In full diodes, however, this is rather an exception to the general rule that the carrier densities in a diode vary exponentially. This can even be the case in a pure intrinsic film if the charge carriers are not generated homogeneously by illumination. As soon as there is a gradient in the carrier concentration at finite temperature, diffusion occurs and carriers migrate from regions of high concentration to regions of lower concentration. Fick's law describes this process quantitatively in terms of a gradient driven diffusion current density for electrons

$$j_n = qD_n \frac{dn(x)}{dx} \quad (3.21) \quad \text{and} \quad j_p = -qD_p \frac{dp(x)}{dx} \quad (3.22)$$

for holes, where D_n and D_p are the electron and hole diffusion coefficients. The diffusion coefficient can be related to a diffusion length

$$L_D = \sqrt{D\tau_D} \quad (3.23) \quad \text{and mobility} \quad \mu_{n/p} = \frac{qD_{n/p}}{k_B T}. \quad (3.24)$$

L_D can be interpreted as the distance a particle can be found away from its origin after the time τ_D .

3.4 Current-Voltage characteristics

The current density-voltage characteristics (j - V) measures the total recombination rate (Fig. 3.1④) in a semiconductor device (e.g. a solar cell) as function of the voltage V applied at the electrodes. Thereby, a current will flow whenever generation and internal recombination is out of balance. This can be archived by shorting anode and cathode, while simultaneously shining light to the device, causing electrons collected at the ETM to flow to the HTM directly via a external wire which leads to a so called short circuit current. In this case, the recombination will happen not in the absorber but at the electrodes. Alternatively, it is possible to keep the solar cell in the dark and applying a voltage at the electrodes pushing electrons into the device where they will recombine, in this case the solar cell will act as a LED. It is of course also possible to do both, applying illumination and voltage simultaneously. Thereby, for every illumination a specific voltage can be found where generation and recombination are exactly balanced. As this voltage can be measured when the electrodes are not connected externally, it is called open circuit voltage (V_{OC}). It should be noted that for reasons of comparability the current is generally normalized by the device area. An example of such a current density-voltage ($j(V)$) relationship is shown in Figure 3.3a.

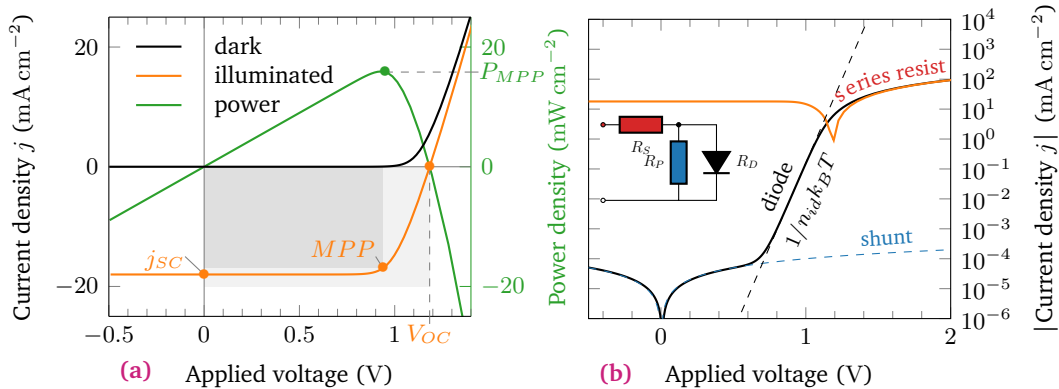


Figure 3.3.: Current voltage characteristics of a solar cell with (—) and without (—) being illuminated. a) Characteristic points in the current density (left axes) are indicated with •. The point where the power output $-j \cdot V$ has its maximum is indicated with •. The rectangle span by the MPP divided by $V_{OC} \cdot j_{sc}$ defines the fill factor. b) Semi-logarithmic $|j|$ - V characteristics. Where the parasitic contributions of series resistance R_S and leakage R_P become visible, leading to a deviation from the ideal diode relationship. The inset circuit diagram shows a common way to model these contributions.

The short circuit current density j_{SC} is defined as $j(0V)$, the V_{OC} by $j(V_{OC}) = 0 \text{ A cm}^{-2}$. In between these two points, the power output $P(V) = -j(V) \cdot V$ is positive with a maximum at the maximum power point (MPP). It also defines the fill factor FF as the ratio

$$FF = \frac{j_{MPP} \cdot V_{MPP}}{j_{SC} \cdot V_{OC}} = \frac{P_{MPP}}{j_{SC} \cdot V_{OC}}. \quad (3.25)$$

It can be interpreted geometrically as the degree of filling of the rectangle spanned by V_{OC} and j_{SC} by area spanned by the axis origin and MPP and is a measure of how rectangular the j - V curve is. The FF can be used to express the PCE

$$PCE = \frac{P_{MPP}}{P_L} = \frac{FF \cdot V_{OC} \cdot j_{SC}}{P_L}, \quad (3.26)$$

where P_L is the power density of the light the solar cell is exposed to, as the power output of the solar cell depends on the load applied to it. V_{MPP} changes with different illumination intensities and for energy harvesting it is therefore needed to adjust the load of the solar cell in a way that it always operates at MPP , even under the varying light conditions in real world scenarios like slightly cloudy days. An ideal solar cell would show a strictly exponential j - V relationship. A real one however suffers from different parasitic effects. The two most common ones are a resistance R_S in series and shunt resistance R_P in parallel to the diode as shown in the inset to Figure 3.3b. They do not always show a pure ohmic behavior and can have multiple physical origins, but assuming them to be ohmic is a good start for device modeling. Such losses can easily be introduced into the Shockley equation, leading to the generalized form^[118]

$$j = j_0 \left[\exp \left(\overbrace{\frac{q(V - jR_S)}{n_{id}k_B T}}^{\text{series loss}} \right) - 1 \right] + \underbrace{\frac{V - jR_S}{R_P}}_{\text{shunt current}} - qG_{ph}, \quad (3.27)$$

where the term G_{ph} is the flux density of absorbed photons creating a generation current. The term j_0 is herein referred to as dark saturation current density. Equation 3.27 can not be written as an explicit function $j(V)$ but can still be plotted by a simple parametrization with $V_{int} + jR_S = V$. Figure 3.3b shows $|j(V_{int})|$ vs. $V(V_{int})$ on a semi-logarithmic scale where the different contributions become visible: A shunt contribution at low voltages, series resistance limited current at high voltages and an exponential diode current in between with a slope of $1/n_{id}k_B T$ where n_{id} is the ideality factor of the diode. It ranges usually between 1 and 2 depending on the mechanism of recombina-

tion. Per definition, no external current is flowing at V_{OC} conditions and according to Equation 3.27 there are also no losses due to series resistance present. For this reason V_{OC} conditions are extremely valuable from an experimental point of view, as they allow statements about internals of the device, unadulterated by parasitic resistances.

3.4.1 Detailed balance limit

The assumption that all photons with energies greater than the band gap are completely absorbed, while those of lower energy pass through the semiconductor without any interaction, allows to derive a fundamental limitation of solar cells. The maximum efficiency of a solar cell in converting light to electricity is called the *detailed balance limit* or after its discoverers also *Shockley-Queisser limit*. It depends solely on the temperature of the solar cell T , its band gap and the light spectrum which the solar cell is exposed to.^[119] The spectrum of the sun before hitting the atmosphere is called Air Mass 0 (AM0) spectra. As radiation of thermal origin it can be approximated with the radiation of a black body of 5800 K temperature in a distance of 1 au according to Equation 3.28 as shown in Figure 3.4a. The sun light is partly absorbed by the atmosphere, hence the number of absorbable photons hitting the solar cell has to be obtained from the Air Mass 1.5 (AM1.5) spectra of the ASTM G-173 standard. The AM1.5 spectra is used to simulate the illumination of 1 sun equivalent at the western hemisphere and has a total irradiance of $P_{AM1.5} = 100 \text{ mW cm}^{-2}$. Its photon flux density is also shown in Figure 3.4a and shows clear signs of parasitic absorption, especially in the infrared region of the spectra. The number of photons $N(E_{ph} > E_g) = G_{ph}$ is then obtained by integration of the AM1.5 spectra from E_g onwards to infinity. As already depicted in Figure 3.1② excess energy will be thermalized and thus the maximum energy a solar cell can extract from a photon is limited to E_g . Thereby, the naive efficiency limit would be $\eta_0 = E_g \cdot N(E_{ph} > E_g) / P_{AM1.5}$ what leads to a maximum PCE of $\eta_0(E_g = 1 \text{ eV}) \approx 50\%$. In reality, η_0 can never be reached because of the finite temperature every physical object, including a solar cell, has. According to this, they are all thermal emitters similar to the sun, just with lower temperature. As a result, a solar cell can only generate power from an imbalance between absorbed and emitted photon flux, as otherwise no energy would have been transferred. A reasonable approach to model this property is to also treat the solar cell as black body which, due to reciprocity, only emits for energies higher than the band gap via a purely radiative recombination process (Fig. 3.2①). The spectral

distribution of the Black-body radiation follows from the Plank law

$$U_{ph}^{\circ}(E, T) = \frac{8\pi}{c^2 h^3} \frac{E^2}{e^{E/k_B T} - 1} \quad (3.28) \quad \text{or} \quad N_{ph}^{\circ}(E, T) = \frac{c}{4} U_{ph}^{\circ} \quad (3.29)$$

Equation 3.28 describes the energy density of photons stored in such a black body at a given temperature.^[111] If this energy is emitted from a sphere in all spatial directions, the photon flux density $L_{ph}^{\circ}(E, T) = \frac{c}{4\pi \text{sr}} U_{ph}^{\circ}(E, T)$ is obtained by the speed c of the photon as the energy carrier, and the solid angle $4\pi \text{sr}$ into which these photons are emitted (in units of $\text{s}^{-1} \text{sr}^{-1} \text{m}^{-2} \text{eV}^{-1}$). In case the emission takes place from a shaped object, Lambert's cosine law must be applied.^[120,121] In example of the photon flux emitted from a flat solar cell into a half-space, results in Equation 3.29.^[111,121] By using Equation 3.14 and Equation 3.16, an expression for the j - V characteristics in the so called radiative limit is provided as the difference between charge carrier generation rate and radiative recombination rate via

$$j_{rad}(V) = q(k_{rad} n_i^2 (e^{qV/k_B T_c} - 1) - G_{ph}), \quad (3.30)$$

where T_c is the temperature of the solar cell. Assuming that a solar cell acts as perfect black body above E_g , as non emitting white body below the band gap and only emitting to one side, the value of $j_0^{rad} = qk_{rad} n_i^2$ can be calculated from the black body spectra from Equation 3.29. In thermal equilibrium condition, where the number of thermally generated photons inside the solar cell must match the number of thermal photons emitted into the environment it follows:

$$j_0^{rad} = \frac{2\pi}{c^2 h^3} \int_{E_g}^{\infty} \frac{E^2}{\exp\left(\frac{E}{k_B T_c}\right) - 1} dE. \quad (3.31)$$

The PCE from the resulting j - V characteristics is shown in Figure 3.4b for different values of T_c . It shows that at 300 K the maximum PCE of 33.7% can be reached with a band gap of 1.37 eV. Perovskites are already close to this value but still have unexploited potential left. However, the detailed balance limit also reveals techniques for improving the efficiency of solar cells in general, regardless of material and band gap. From a practical point of view, two techniques are relevant nowadays. The first approach is called a *tandem* or *multi-junction* solar cell, in which materials with different band gaps are stacked on top of each other in order to use the second layer to harvest energy

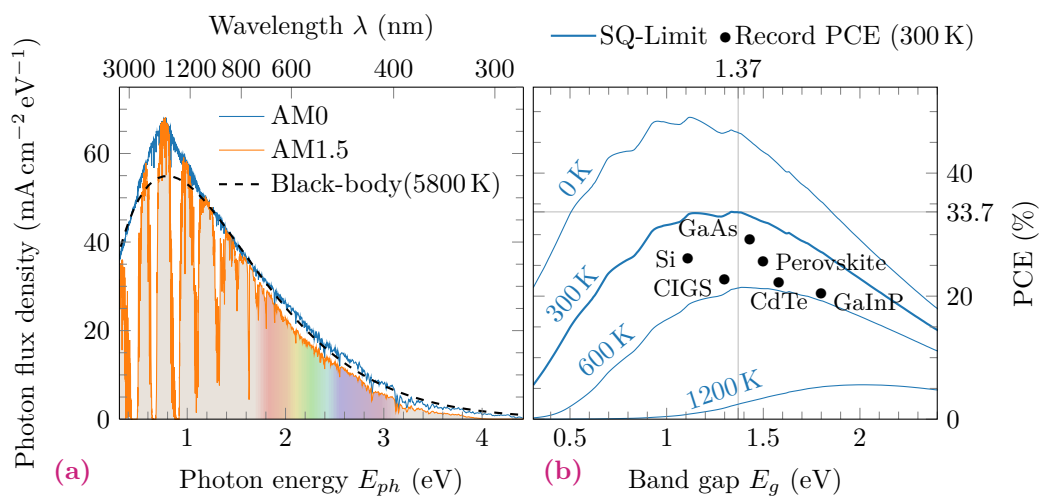


Figure 3.4.: a) Photon flux density spectrum of the sun before hitting the atmosphere (AM0) and after (AM1.5).^[122] The spectral density can be approximated with a blackbody radiation with a temperature of 5800 K. b) The maximum possible power conversion efficiency achievable with the AM1.5 spectra as a function of solar cells band gap and temperature. For reference, some of the record PV technologies at 300 K are indicated (●)

from light transmitted through the first. Because they are inherently more expensive to manufacture, they are often combined with the second approach to circumvent the detailed balance limit, i.e. to increase the incident photon flux by concentrating solar radiation from a large area onto a smaller solar cell.

3.4.2 Transient and Hysteresis properties

The j - V characteristic of solar cells based on perovskites differs fundamentally from that of other materials in one aspect. The currents measured at a voltage depend on whether the voltage is cycled from negative to positive values or vice versa. The magnitude of this effect also depends on how fast the voltage is swept. The dependence on the scan rate used in the measurement is exemplarily shown in Figure 3.5. It shows two different effects causing a scan rate dependent current. The first one can be observed in any device with a sufficiently high capacitance C independent of the actual solar cell technology. At any capacitor, a voltage changing in time causes a capacitive current I_C flowing, which sign and magnitude depends linearly on the time derivative of the voltage.^[123] In litera-

ture this phenomenon is sometimes referred as dark current hysteresis.^[124] The current density caused hereby is rather low and thus can only be seen at low voltages while the device is kept completely away from any light exposure. The resulting offset current is indicated with an arrow in Figure 3.5a and often makes extrapolation necessary in order to determine j_0 correctly from a j - V measurement. In practice, this capacitive effect is often masked by high shunt currents or stray light hitting the device, resulting in a similar-looking current offset, but with a magnitude and sign that is independent of the scan rate and direction. In addition to this capacitive property, a hysteresis in the diode

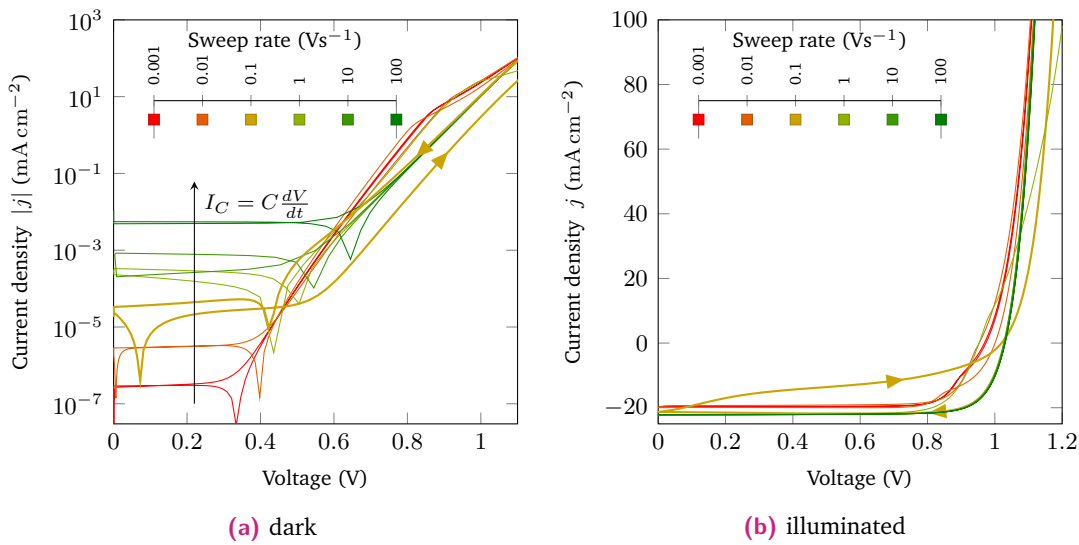


Figure 3.5.: a) Dark current density at different scan rates on log scales. At high scan rates a capacitive current becomes increasingly visible at the lower voltage range. Also at higher voltages the exponential diode current shows a scan dependence on scan direction and rate which is also visible in the illuminated case b) where the photo current is much higher than the contributions from the device capacitance. At medium scan rates (—) the forward and backward scans show the largest difference.

current can be observed in many perovskite solar cells in the illuminated characteristic curve as it is depicted in Figure 3.5b. This current voltage hysteresis also depends on the measurement speed. The non-capacitive current voltage hysteresis has a maximum contribution at a certain scan rate and disappears for much faster and slower measurement speed.^{Unger14, [123,125]} In literature many proposals can be found on how to quantify the magnitude of hysteresis correctly mostly by defining the relative differences in V_{OC} , j_{SC} , FF or PCE between the forward and backward scan.^[123,126–129] The exact characteristics of the hysteresis behavior depend not only on the scan speed but

also on many other external parameters such as temperature, maximum and minimum applied voltage or pre-applied conditions like a potential over longer times.^[123]

The first more phenomenological investigations on hysteresis behavior came to the assumption that charge carrier trapping/de-trapping^[49] or ferroelectricity^[49,130,131] might be responsible for this particular behavior. However, ionic migration was also considered to be the main driver of this phenomenon early on^[48,49] which was verified in a multitude of experimental and theoretical studies later on.^[62,66,69,125,132] The charge redistribution associated with ionic migration changes primarily the internal electrostatic field which consequently also affects the charge carrier distribution in the device. This coupling between ions, electrons and holes makes the resulting dynamics and its interpretation highly non-trivial. The impact of mobile ions to the internal energetic landscape is depicted in Figure 3.6, where Iodide anions and their positively charged vacancies are considered as the mobile species. In Figure 3.6a the ions are uniformly

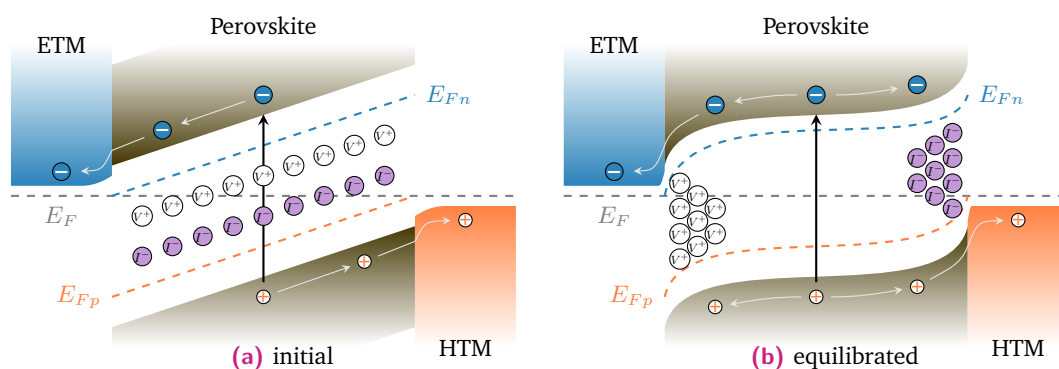


Figure 3.6.: The concept of ionic migration inside a perovskite layer can be phenomenological understood by a) initially homogeneously distributed ions underlying the same electrostatically induced drift as electrons and holes towards their electrode. b) Finally they are accumulated there leading to a screening of the electrostatic potential.

distributed and the device is under j_{SC} conditions. An electron-hole pair generated in the perovskite layer is separated by the gradient of the electrostatic potential prevailing there. However, this driving force applies to all charges, and if they are mobile, they also move in the direction of the transport layers. In this case, ionic charges will accumulate at the interfaces because the organic transport layers are not conductive for them. This situation is visualized in Figure 3.6b, where this interfacial charge accumulation leads to a screening effect in that sense, that a generated charge inside the perovskite layer is not driven by an electrostatic field any more. Consequently, in this equilibrated

state the extraction process is less efficient as before, resulting in an altered contribution from surface and bulk recombination to the total recombination current measured by the j - V . In addition, it can be taken for granted that such a mass transport can also cause several downstream effects. It is conceivable that such ionic vacancies and interstitials act as mobile recombination centers. In addition, it has been shown that these mobile ions can undergo chemical reactions at the electrodes also change the device performance and are not always reversible.^[133,134] It has been shown, however, that already the assumption of ionic migration without any downstream effect is sufficient to the model current voltage hysteresis especially if surface recombination is accounted for.^[125,135–137] This model also nicely renders the measurement speed dependency of the hysteresis effect. The electrostatic potential within the solar cell is depicted in Figure 3.7. If the measurement is performed fast enough, the ions do not have enough time to redistribute themselves and can be considered immobile within the measurement period. As a consequence, the electrostatic potential within the solar cell is independent of the measurement direction (Fig. 3.7a) and hysteresis is not observed. The situation is similar for very slow measurements. Here, too, the electrostatic potential is identical for backward and forward measurements, since the ions have enough time to follow the applied voltage. When the measurement and ion migration takes place on a similar time

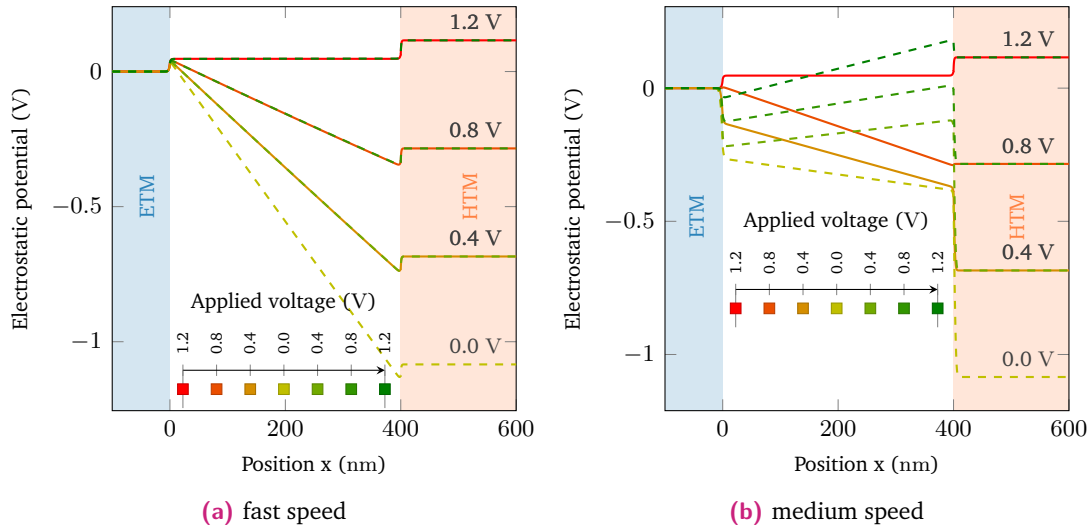


Figure 3.7.: Example of the electrostatic potential profile across a solar cell at different voltages during an j - V measurement. Starting from a forward bias state when the measurement is conducted a) faster than the ion migration can take place and b) in timescales similar to that of the ionic migration. For clarity, the backward scans are depicted as dashed lines.

scale, the electrostatic potential is different in the forward and reverse scan directions, as shown in Figure 3.7b. In this case, the inverted electrostatic potential that occurs after the change in scan direction is responsible for the hysteresis.

Methods

The following chapter is separated into four sections. In the first section the materials are introduced that were used as transport and blocking layers. The second section describes the device fabrication and manufacturing techniques. The third section introduces the different experimental techniques used for device characterization to study the electrical properties and ion dynamics of perovskite solar cells. In the last section of this chapter the numerical method used to simulate the device properties is outlined in detail.

4.1 Materials

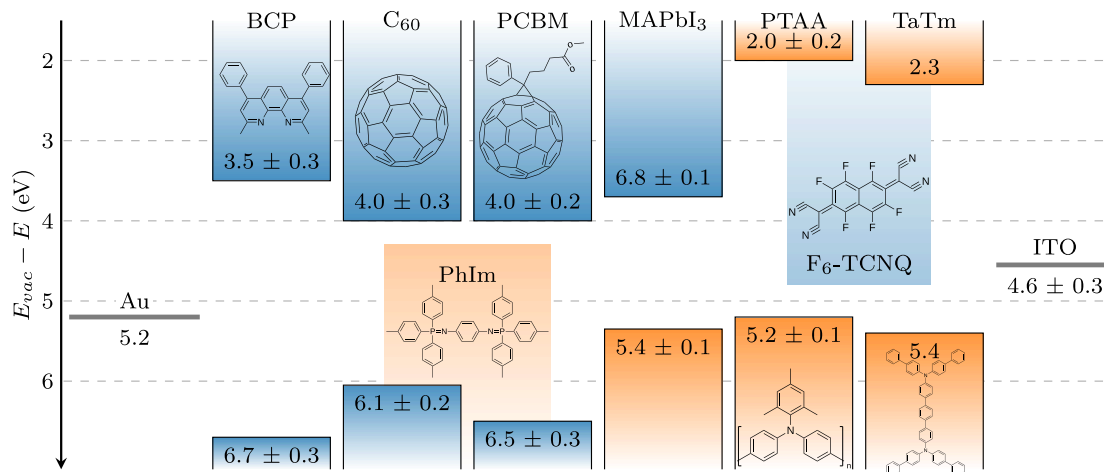


Figure 4.1.: Overview of the transport materials used in this work. The HOMO and LUMO levels of these materials are provided. The error roughly covers the spread over reported values in literature. The color indicates the material class, where ETMs are shaded blue, HTMs orange. The lighter blue and orange colors indicate the ionization potentials of the respective dopants. Two-colour MAPI symbolises the ability to contact both electrons and holes. It has to be noted, that all depicted molecules own a conjugated π -electron system.

ITO

ITO is a n-type semiconductor with a band gap of 3.6 eV^[138] and is therefore almost non absorbing for light in the visible spectral range.^[139] At the same time ITO is still an excellent electrical conductor with a sheet resistance of around $10^{-4} \Omega \text{ cm}$. This rare combination of transparency and electrical conductivity makes ITO a commonly used material in displays, touch panels or special applications like heated windows. In this work ITO is used as electrode material in solar cells, where it's work function is reported to be in the range of 4.3 to 4.9 eV.^[138,140–142]

PTAA

Poly[bis(4-phenyl)(2,4,6-trimethylphenyl)amine (PTAA) is a poly(triaryl)amine derivative used as HTM for perovskite solar cells since 2013.^[143] The LUMO level is located at 1.8 to 2.2 eV and the HOMO 5.1 to 5.2 eV below the vacuum level.^[141,144–147] This results in a high energy gap of 3 eV which makes PTAA virtually non absorbing for most of the solar radiation^[144] and therefore especially suited for p-i-n solar cell configurations where the light is hitting the HTM before it can be absorbed by the active perovskite layer. Due to the outstanding electro-optical characteristics and chemical variability, triaryl amines can also be found in organic light emitting diodes, transistors and other applications of organic electronics.^[148] For organic materials PTAA can show a high hole mobility which heavily depends on chain length and its dispersity, purity and doping.^[149] This explains the huge spread in reported values which are in the range of 1×10^{-6} to $4 \text{ cm}^2 \text{ V}^{-1} \text{ s}$.^[146,149,150] As a polymer its molecular weight is too high for thermal vacuum evaporation and it is essentially exclusively processed from solutions.

TaTm

The hole transport material N4,N4,N4'',N4'''-tetra([1,10-biphenyl]-4-yl)-[1,1':4',1''-terphenyl]-4,4''-diamine (TaTm) is a triarylamine derivative and has a LUMO of 5.4 eV and a HOMO of 2.3 eV below vacuum level.^[151] In contrast to PTAA, it is a monomer and can be deposited by thermal vacuum evaporation^[152], making this material family also relevant in other fields of organic electronics.^[153]

C₆₀

The buckminsterfullerene (C₆₀) is a spherical allotrope of carbon. It was found by laser evaporation of graphite in 1985 by Kroto who together with Curl and Smalley, was honored with a Nobel price in 1996 for this discovery.^[154] Its unique physical and chemical properties are potentially suitable for a multitude of applications like supercaps, nano-electronics, biomedical applications and many other fields of research.^[155] Because of its good electrophilic properties, C₆₀ is used in this work as the ETM. As large molecule (molar weight of 721 g mol⁻¹) it is subject to many different inter and intramolecular interactions, making its exact electronic properties hard to predict. The spread of values for its energetic levels is quite large in literature as they heavily depend on the environment of the C₆₀ molecule. The LUMO level is located at 3.7 to 4.3 eV and the HOMO 5.9 to 6.2 eV below the vacuum level^[156-159], with an energy gap of 1.7 to 2.5 eV.^[155,157,160] Since its chemical structure is free of polar groups, it is almost insoluble in most solvents and is therefore usually applied by thermal evaporation under high vacuum.

PC₆₁BM

[6,6]-Phenyl-C₆₁-butyric acid methyl ester (PC₆₁BM) is a C₆₀ derivative modified in order to have a higher solubility in organic solvents like chlorobenzene or toluene. Depending on the solvent it has a 10 to 100 times increased solubility compared to C₆₀.^[161] This was achieved by adding a functional phenyl and methyl butyrate group to the C₆₀ ball as polar and hydrogen-bonding component.^[162] The development of soluble fullerene was one major key to enable printable OPV, as it allows high molar concentrations in the ink needed for this process. PC₆₁BM shows opto-electronic properties similar to C₆₀ with a HOMO at 6.8 to 6.2 eV and a LUMO 3.8 to 4.2 eV below the vacuum level depending on literature.^[141,163-166]

Dopants

The doping process in organic semiconductors is only partially comparable to that in classical ones, such as silicon or GaAs. Organic semiconductors often have an amorphous structure and even if they are in an ordered lattice, it is difficult to find a dopant that can be incorporated into it.^[167] For n-doping, the dopant must be able to donate electrons

to the LUMO and, for p-doping, to the HOMO of the material. In this work, this is achieved by means of molecular doping. The N1,N4-bis(tri-p-tolylphosphoranylidene) benzene-1,4-diamine (PhIm) is used as donor molecule for the acceptors C₆₀ and 2,2'-(perfluoronaphthalene-2,6-diylidene) dimalononitrile (F6-TCNQ). It has a high electron affinity within and its neutral form has a LUMO of 5.6 eV.^[168] The ionization energy of the negatively charged anion (4.8 eV^[169]) is still close to HOMO energy of many hole transport materials so that it often accepts two electrons per molecule.

[167]

BCP

2,9-Dimethyl-4,7-diphenyl-1,10-phenanthroline or Bathocuproin (BCP) is typically used as a buffer layer between the fullerene-ETM and the metal electrode with a thickness in the range of 2 to 10 nm. It causes the formation of an ohmic contact which would otherwise result in a Schottky barrier at the fullerene-metal interface. While the LUMO of the PCP layer is energetically too high for an efficient electron transport (2.7 to 3.5 eV below the vacuum level^[158,159,170]), these layers are thin enough to allow for efficient electron tunneling.^[170] Other authors make a high density of defect states within the BCP layer responsible for charge transport across this energetic barrier.^[156] The reports for the HOMO energy range from 6.4 to 7.0 eV below the vacuum level.^[157-159,170,171] Vacuum deposited BCP layers have a compact morphology which additionally prevents the ETM from contamination with metal atoms during the electrode deposition.^[172]

4.2 Device Preparation

In general, perovskite solar cells can be realized in many ways and the past years of research have resulted in a wide variety of available material combinations. This work is limited to solar cells of the planar type, as shown in Figure 2.4b. These planar cells offer the advantage over the mesoporous ones that they can be modelled reliably due to their well-defined layer sequence. The production of a solar cell starts with a glass substrate coated on one side with ITO of 100 nm thickness (VisionTek Systems Ltd., United Kingdom). These thin layers have an electrical sheet resistance of 10Ω corresponding to the electrical resistivity of $1 \mu \Omega \text{ m}$ and allow for transmission of about 92 % of the visible light.^[139] By means of a photolithography process, strip-like electrodes with a width of 3 mm are etched out of the closed ITO layer by nitric acid hydrochloride. The substrates are cut to the desired size of $(127 \times 127) \text{ mm}^2$ using a glass cutter. This is followed by thorough cleaning with water, acetone and isopropanol in an ultrasonic bath for 10 min each. In a final step, the substrates are being exposed to a low pressure oxygen plasma for 30 s to remove organic residues and enhance the wettability needed in the further steps.

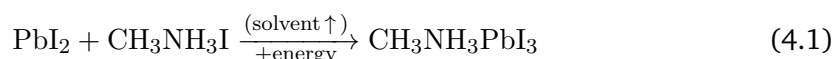
Hole transport layer deposition

The PTAA layer is fabricated by transferring the cleaned ITO coated substrates into a nitrogen filled glove box. PTAA (Sigma-Aldrich) is dissolved in toluene with 1 mg mL^{-1} weight concentration and processed by room temperature spin coating with 6000 rpm for 30 s on to the substrates resulting in a layer thickness of $>5 \text{ nm}$. These films are subsequently dried at $100 \text{ }^\circ\text{C}$ for 5 min on a hot plate.

To fabricate the layers based on TaTm (Novaled, Germany), the substrate is placed into a vacuum chamber and evacuated to a pressure of 10^{-6} mbar . At a temperature of $250 \text{ }^\circ\text{C}$ the TaTm is then sublimed with a constant evaporation rate of 0.8 \AA s^{-1} , monitored by quartz crystal microbalance (QCM) sensors, up until the desired layer thickness of 40 nm is reached. The dopant F6-TCNQ is co-sublimed during this process at temperatures ranging from 135 to $160 \text{ }^\circ\text{C}$ and controlled by a separate QCM sensor. The doped TaTm layer is capped with 10 nm of the pure C_{60} deposited at 0.5 \AA s^{-1} . After this deposition, the chamber is vented with dry N_2 .

Perovskite layer deposition

Numerous possibilities and variations are known in the literature to deposit perovskites as thin films on substrate. They have in common that the perovskite is formed from the precursors during the process and is virtually never applied directly. For MAPbI₃ films the precursors are lead(II) iodide (PbI₂) and methylammonium iodide (MAI) undergoing the stoichiometric reaction



in which a possible solvent has to be removed and some energy, mostly in form of heat, is needed to deliver the activation energy needed for the perovskite formation. In the meantime, the processes have been consolidated to such an extent that essentially two processes are leading the race for the solar cells with the highest efficiency and deliver the best results in terms of cell performance. The successful strategy of sequential deposition was first published by Burschka et al.^[173] and 2014 improved by Xiao et al.^[174] to what they called *interdiffusion* approach which is illustrated in Figure 4.2a.

The key idea is to first deposit a thin film of PbI₂ from a solution, let it dry for a short period of time and then expose it to MAI. This way a reproducible and homogeneous film growth is archived when the PbI₂–MAI stack is heated up to 100 °C. This is accompanied by a rapid change in color from light yellowish to dark brown due to the high absorption coefficient of the formed MAPbI₃. As the final stoichiometry of the perovskite film is badly defined in this process, Xiao et al. improved this method by using an orthogonal poor solvating solvent directly after the deposition of a premixed precursor solution^[175] as it is shown in Figure 4.2b. This procedure helps to remove other solvents resulting in a fast crystallization of the perovskite. This way perovskite films can be produced with virtually no roughness in vertical direction and a superior homogeneity on areas of 1 cm² or more. Herein, two types of perovskites are studied which differ in the choice of organic cation. MA and formamidinium (cation) (FA or FA⁺) are fabricated using the fast crystallization approach, leading to MAPbI₃ and formamidinium lead iodide (FAPbI₃) perovskite respectively. For MAPbI₃ films a precursor solution with a concentration of approximately 1.3 mol L⁻¹ is prepared by dissolving 1.3 mmol (600 mg) PbI₂, 1.3 mmol (224 mg) MAI and 1.3 mmol (102 mg) dimethyl sulfoxide (DMSO) in 1 mL dimethylformamide (DMF) at 100 °C. The precursor for FAPbI₃ films is prepared in the same concentration by dissolving 1.3 mmol (600 mg) PbI₂, 1.3 mmol (224 mg) formamidinium iodide

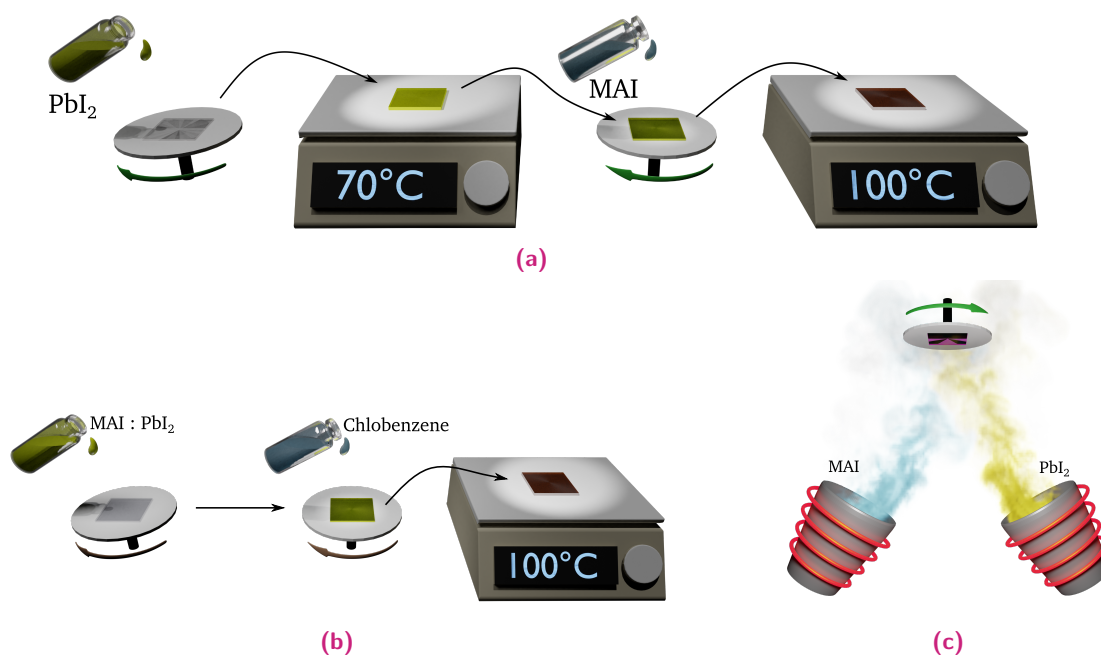


Figure 4.2.: Schematic illustration of (a) the two step fabrication process of perovskite thin films in example of MAPbI₃. In the first step the PbI₂ solution is deposited on a glass substrate. After a short time on the hotplate the second precursor MAI is then applied and the perovskite is formed in a final annealing step. (b) The fast crystallization approach where the premixed precursor solution is quenched by an anti-solvent and annealed afterwards on a hotplate. (c) Co-evaporation method in which MAI and PbI₂ is evaporated simultaneously under high vacuum. The kinetic energy of the precursor gases is sufficient to cause formation of a uniform and homogeneous perovskite film.

(FAI) and 1.3 mmol (102 mg) DMSO in 1 mL DMF at 100 °C. Thereby, the perovskite films are made by spin coating the precursor solution at 4000 rpm for 30 s. During this step 200 μ L chlorobenzene (CB) is dripped on top of the wet film 10 s after the spin coating process has started. Then the MAPbI₃ substrate is annealed for 15 min at 100 °C. The FAPbI₃ film needs higher temperatures in order to crystallize in the correct phase and is annealed at 140 °C. As the process is extremely sensitive to all kind of environmental conditions the manufacturing is conducted inside a nitrogen filled glove box where the oxygen and humidity levels are kept below 0.1 ppm. A further method for perovskite deposition is thermal evaporation. The substrate is mounted in a vacuum chamber on rotary dish in 20 cm distance above two crucibles filled with the precursors, one with PbI₂ and the other with MAI. At a pressure of 1×10^{-6} mbar the PbI₂ is evaporated at 250 °C and the MAI 70 °C leads to a deposition rate of 0.5 \AA s^{-1} and 1 \AA s^{-1} respectively,

monitored by QCM sensors. The process is depicted in Figure 4.2c and results in perfect homogeneous films over 10 cm areas with an accurately controllable film thickness by the evaporation time. The evaporation was accomplished by the group of Dr. Henk Bolink from the University of Valencia (Spain). The details of the deposition process are provided in reference [176]. Due to the achievable high controllability and film homogeneity with this method it can be considered as a candidate for large scale production of perovskite solar cells.

Electron transport layer deposition

The perovskite layer deposition is followed by electron layer deposition. For the solution deposited solar cells, a 20 nm thick PC₆₁BM layer is spin coated from a dichlorobenzene (DCB) solution with a weight concentration of 20 mg mL⁻¹. This is followed by another 60 min annealing at 100 °C. In the last step, the substrates are transferred into an evaporation chamber in order to apply a 20 nm C₆₀ and 8 nm BCP at a rate of < 0.5 Ås⁻¹. Finally, a 60 nm Gold (Au) layer at a rate in the range of 1 to 3 Ås⁻¹ is applied as back contact. For the vapor deposited solar cells, C₆₀ and PhIm are co-evaporated to a final thickness of 40 nm. This n-doped ETM is capped by the deposition of 10 nm of pure C₆₀.

4.3 Electrical device characterization techniques

4.3.1 Complex Impedance Spectroscopy

The impedance designates the alternating current resistance of an electrical component and has the formula symbol Z . Since this is a complex quantity, it is important to distinguish between Z and its magnitude, the apparent resistance $|Z|$. In the literature, impedance and apparent resistance are not always stringently separated. Impedance spectroscopy can be understood in the context of this work as the measurement of the impedance $Z(\omega)$ as a function of the frequency ω .

Impedance spectroscopy (IS) technique in which the device is held at a specific direct current (DC) bias level. In addition to this DC, an AC modulation is applied, which usually is small in amplitude. By phase-sensing the current I with respect to the applied voltage V , the complex impedance is given as their ratio by Equation 4.2

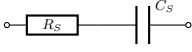
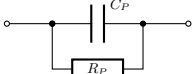
$$Z(\omega) = \frac{V(t)}{I(t)} = \frac{\hat{V}(\omega)e^{i(\omega t + \varphi_V)}}{\hat{I}(\omega)e^{i(\omega t + \varphi_I)}} = \frac{\hat{V}(\omega)}{\hat{I}(\omega)}e^{i(\varphi_V - \varphi_I)} = |Z(\omega)|e^{i\varphi}. \quad (4.2)$$

The resulting impedance of an electrical component can be viewed as a composition of resistive or reactive elements, such as capacitors and inductors, arranged in a circuit. The simplest cases are shown in Table 4.1 and the insets of Figure 4.3. For real solar cells, such equivalent circuit models can become quite complex and easily contain 7 or more free parameters. The problem in such a case is that one can sometimes derive the same $Z(\omega)$ from differently arranged equivalent circuits. For this reason it is important to reflect on the properties under which reliable statements can be drawn.

Capacitance Measurements

IS is often used to determine the small perturbation capacitance of a semiconductor device. As the measured Z consists of a real and an imaginary part it is possible to solve a two parameter circuit model with one single measurement at one frequency. A resistive element can be combined with a reactive one in two ways, in series or parallel, the resulting relations between the Z , C and resistance are provided in Table 4.1. For equivalent circuit models with more than 2 free parameters it is necessary

Table 4.1.: Transformations of the complex impedance value to the values of the respective equivalent circuit elements. $\Re(Z)$ and $\Im(Z)$ refer to the real and imaginary part of Z

	Circuit	Impedance	Capacitance	Resistance
Series		$Z_S = R_S + \frac{1}{i\omega C_S}$	$C_S = \frac{-1}{\Im(Z)\omega}$	$R_S = \Re(Z)$
Parallel		$Z_P = \left(\frac{1}{R_P} + i\omega C_P \right)^{-1}$	$C_P = \frac{-\Im(Z)}{ Z ^2\omega}$	$\frac{1}{R_P} = \frac{\Re(Z)}{ Z ^2}$

to measure $Z(\omega)$ at several different frequencies. As such an approach leads to an overdetermined system of equations, a fitting routine has to be applied in order to derive the model parameters. Alternatively, it is sometimes possible to pick a suited frequency where certain contributions dominate over others. Figure 4.3a shows how the impedance at low and high frequencies can be used to determine the resistive elements directly, even if the actual circuitry consists of 3 circuit elements. This can be done by reading out $|Z|$ resp. $\Re(Z)$ whenever the phase φ is close to zero. In dielectrics like the absorber of a solar cell under low injection conditions the resistive losses are often negligible within a certain frequency window. In such a case, even the simplest equivalent models (as in Table 4.1) can lead to a correct determination of the actual capacitance as shown in Figure 4.3b. For this, it is important that the phase shift between U and I meets the condition $\varphi \approx \pi/2$. However, if significant resistive losses are present, the underlying loss mechanism has to be known in order to obtain correct results. When it is assumed that the losses occur inside the actual dielectric medium, the parallel mode is a good choice. In this case, the complex of the dielectric function $\varepsilon_r = \varepsilon'_r + i\varepsilon''_r$ is directly related to the capacitor in a planar geometry by

$$C_P = \varepsilon_0 \varepsilon'_r \cdot \frac{A}{d} \quad (4.3) \quad \text{and} \quad \frac{1}{R_P \omega} = \varepsilon_0 \varepsilon''_r \cdot \frac{A}{d}, \quad (4.4)$$

where A is the area, d the thickness of the capacitor and ε_0 the vacuum permittivity. However, PSC often suffer from a relatively high series resistance due to the TCO layer, especially when their active area is large. In such a case the series mode can also be a good choice.

The schematic setup for IS measurements is depicted in Figure 4.4. It consists out of

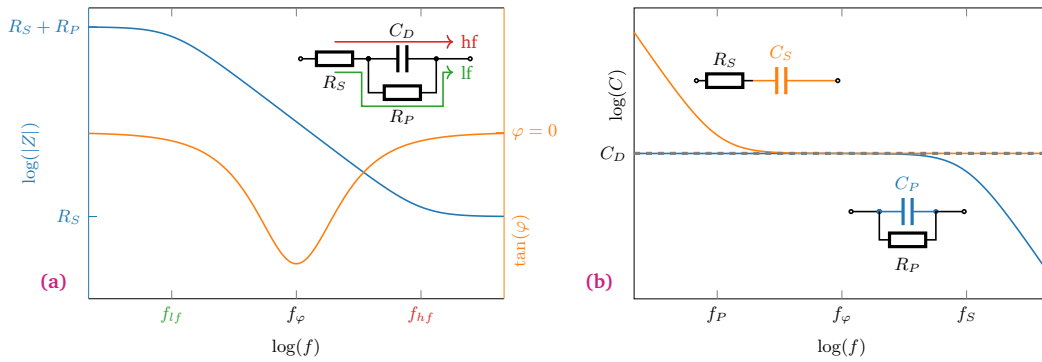


Figure 4.3.: (a) The impedance of the circuit shown in inset as function of frequency. $|Z|$ (—) is limited by the sum of all ohmic components at low frequencies and the series resistance at high frequencies. At the maximum of $\Im(Z)/\Re(Z)$ (—), f_φ can be found where the impedance is almost purely imaginary ($\varphi \approx \pi/2$). (b) At f_φ , the capacitance can be directly determined irrespective of where the resistive losses are assumed to happen. C_D (---) is the actual capacitance present suffering with R_S and R_P simultaneously. The C_s mode (—) overestimates the capacitance when $f < f_P$ while the C_p mode (—) underestimates when $f > f_S$.

a signal generator to generate the alternating current (AC) voltage, a high bandwidth current/voltage amplifier and an digital storage oscilloscope (DSO) as analog/digital converter to measure the time varying current and voltage. The amplitude and phase information is then obtained via a software implemented lock-in amplifier. This makes it possible to record transient capacities with high time resolution and bandwidth (20 μ Hz -200 MHz) overcoming the usual bandwidth limitations which most lock-in amplifiers have. However, if no transient measurement is required and only the frequency range between 20 Hz and 2 Mhz is needed, these components can be replaced by the Agilent E4980A as single device. Instead of voltage, it is also possible to bias the solar cell with light from a LED light source. As the sample is mounted inside a closed cycle helium cryostat the temperature can be adjusted precisely (by a Lakeshore 332 cryogenic temperature controller) while the sample is kept save from oxygen, humidity or unwanted stray light from the environment. In addition, a helium bladder is installed on the cryostat to guarantee isobaric conditions at different temperatures.

4.3.2 Open Circuit Voltage Decay

The open circuit voltage decay (OCVD) is a transient property of electrical devices. It describes the disappearance of a measurable voltage over time when no external load is

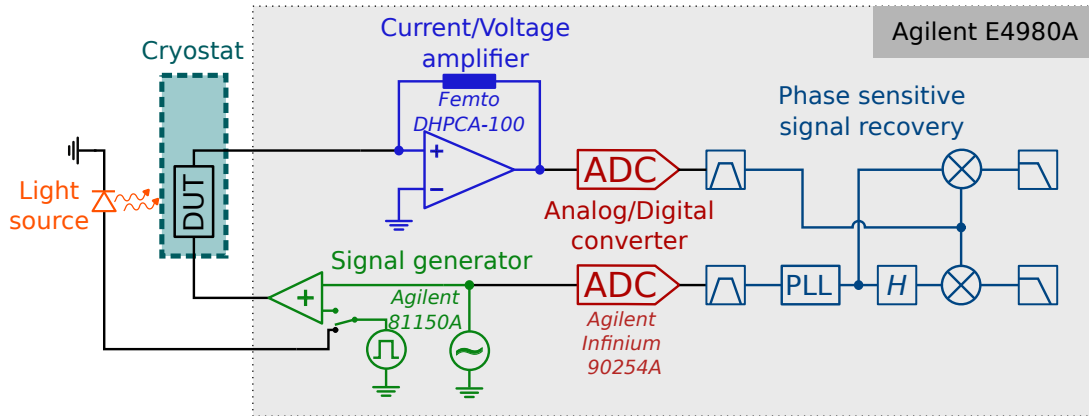


Figure 4.4.: Schematic illustration of a setup for impedance measurements. The different assemblies have been colored for clarity.

applied. In terms of solar cells, the OCVD is caused by charge carrier recombination in the device leading to a transient reduction in voltage according to Equation 3.12. The measurement principle is depicted in Figure 4.5. First, the solar cell is placed inside a completely dark environment and then illuminated with a white light LED under open circuit conditions for a time t_{on} . The time it takes for the solar cell to built up a certain V_{OC} depends fundamentally on two factors, the device capacitance C_p and the illumination intensity as it defines the generation rate.

Before the device is exposed to light, there are no excess charges in the device. Immediately after the LED is switched on the carrier dynamics is solely ruled by the generation rate, as there are still no excess charges and thus no recombination ($G_{ph} \gg R_{rec}$). This can be seen as the charging process of a capacitor

$$\frac{dV}{dt} = \frac{dQ}{dt} \frac{dV}{dQ} \approx qAG_{ph} \frac{1}{C_p}, \quad (4.5)$$

where A is the device area. From Equation 4.5 it is clear that for low illumination the voltage built up will take longer than higher ones. Therefore, it is important to apply a sufficient illumination time to reach a steady state V_{OC} . At the time t_0 the LED is switched off and the voltage decay can be observed. In Figure 4.6, the solar cell is represented via a circuit diagram where the capacitance and shunt resistance are drawn separately. In this model the OCVD can be explained as a capacitor discharging over a diode. By neglecting parasitic resistive losses and treating the capacitor as constant over all voltages and times, it is possible to derive an analytic expression for the OCVD. The

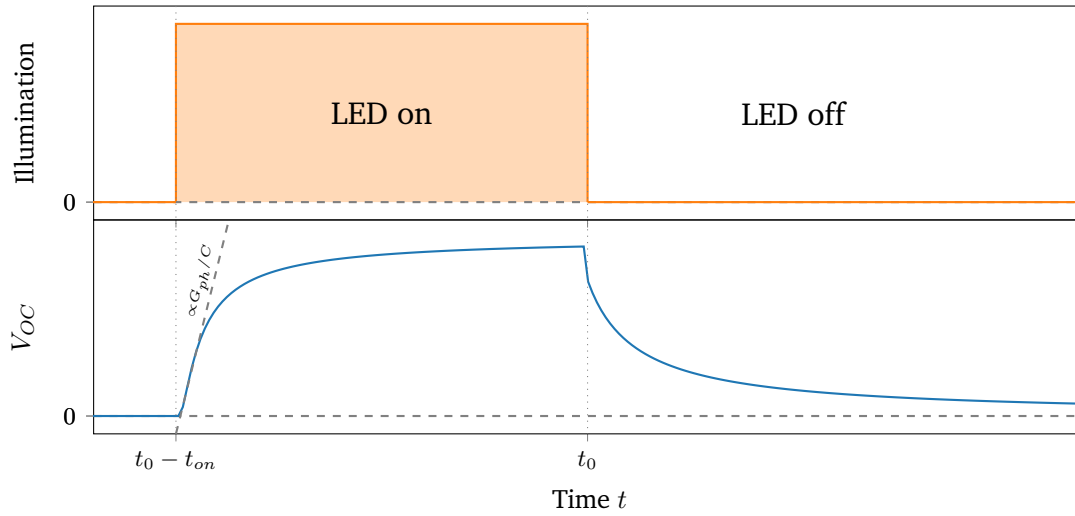


Figure 4.5.: Schematic illumination and voltage transients used to measure a OCVD. The solar cell is illuminated with a constant intensity up until steady state is reached. Then the LED is switched off and the actual OCVD is measured.

diode current (Eq. 3.27) must then be equal to the displacement current of the capacitor leading to

$$j(V_{OC}) = j_0 \left[\exp \left(\frac{qV}{n_{id}k_B T} \right) - 1 \right] = -\frac{C_p}{A} \frac{dV_{OC}}{dt}. \quad (4.6)$$

This differential equation has an analytical solution.^[177] For most of the time it can be approximated due to $V_{OC} \gg q/n_{id}k_bT$ by

$$V_{OC}(t) \approx -n_{id}V_T \ln \left[\exp \left(\frac{-qV_{OC}(t=t_0)}{n_{id}k_B T} \right) + \frac{qj_0A}{n_{id}k_B T C_p} \cdot t \right]. \quad (4.7)$$

From this, it is expected that for longer times the OCVD is proportional to the logarithm of time.

In order to measure the OCVD properly one has to consider that a diode has an extremely high resistance at low voltages. Therefore, the device must be measured with a high-impedance voltmeter/amplifier, otherwise the measuring unit will act as an external load and the open-circuit conditions will no longer be met. For the high resolution measurements of fast transients this is achieved by attaching a $1 \text{ T}\Omega$ voltage amplifier (Femto Messtechnik GmbH) to the DSO. For lower resolution/long time scale measurements, a semiconductor parameter analyzer (Agilent Technologies 4156C, $\geq 1 \text{ T}\Omega$ input impedance) is used. Due to their high input impedance both instruments can be safely

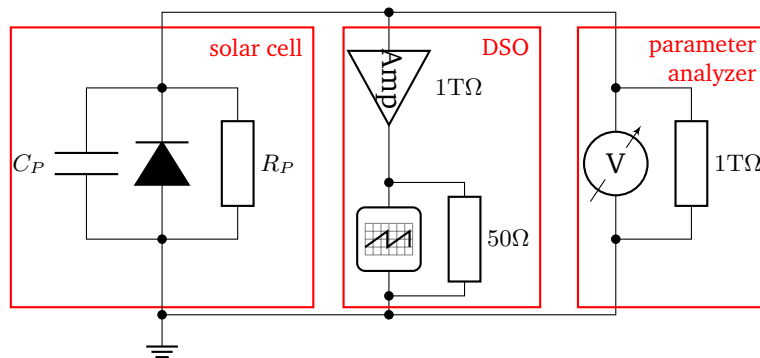


Figure 4.6.: Schematic layout of the setup used to measure the OCVD. Due to the logarithmic time dependence of the decay two instruments are combined to cover the fast and slow parts. The digital storage oscilloscope is used to sample the first 1 s with high sample rate (1×10^8 Sa/s). For the later and slower decay a parameter analyzer is used with lower temporal resolution (10 Sa/s). Due to their $T\Omega$ input impedance they can be connected simultaneously without interfering with each other.

used simultaneously to monitor the device voltage without causing interference. This way the full transient can be recorded at once using the different sample rates from both, the DSO and the parameter analyzer and merging the data afterwards.

4.4 Drift-Diffusion simulations

The special appeal of solar cell simulations is that it is extremely difficult to fully observe the internal dynamics in the device experimentally. By means of suitable simulations, however, one gains access to the quantities about whose relevance one can otherwise only speculate. Of course, a simulation can only be an approximation of the actual conditions, since it is based on model assumptions, which themselves are often only approximations. The art, however, is to get an accurate picture of the actual conditions with as few assumptions as possible. How well this succeeds must be measured by the experiment. The model proposed in this section and its implementation is largely based on the work of Courtier et al.^[136,178,179] who was not only able to simulate the ionic properties of a solar cell but also did this very efficiently in a transient manner. Especially the transient property is crucial in perovskite research as the ionic effects in experiments often take place in the seconds time scale. Hence, it is not enough to only consider a steady state when interpreting the experimental results. A transient simulation can be quite valuable in this case.

4.4.1 Mathematical model

The basic idea behind drift-diffusion simulations of perovskite solar cells and semiconductor devices in general is not to assume the charge carrier density to be constant, but to allow for inhomogeneity in it and to account for the resulting dynamics. The assumption that only the charge transport perpendicular to the electrodes plays a role in the solar cells investigated here can be regarded as indisputable for the planar devices. This is due to the large ratio of the side length of the active area and its thickness ($A/d \approx 10^{-6}$). This way the device is treated as object with only one spatial dimension, drastically reducing computational effort. It should be noted, however, that this picture may not apply adequately to solar cells with relatively thick mesoporous layers. Strictly speaking, at least a two-dimensional model is required to represent the charge transport through such superstructures. The charge transport itself is described as a net effect of charge carrier diffusion from Equation 3.21/3.22 and electrostatic induced drift. The

drift current of a carrier density \hat{N} with a drift velocity ν_d is obtained from Ohm's law. By taking advantage of the Einstein relation (Equation 2.5) it takes the form

$$j = q\hat{N}\nu_d = q\hat{N}\mu E = \frac{q^2\hat{N}D}{k_B T} E = \frac{-q^2\hat{N}D}{k_B T} \frac{\partial\Phi}{\partial x}. \quad (4.8)$$

In the last step of this equation the electrical field strength is written as gradient of the electrostatic potential Φ which will become handy later. As electrons, holes and ions have different densities, diffusion coefficients and charges, their current densities have to be treated separately by Equation 4.10, 4.12 and 4.14.

In each subvolume within the solar cell, the temporal change of the number of charge carriers in that volume results from the difference between the inflowing and outflowing charge carriers, as well as the recombination and generation rate prevailing there. In the limit for small subvolumes one obtains the equations 4.9 and 4.11. For the ionic charge carriers in Equation 4.13, it is assumed that they are conserved and can therefore neither be created nor destroyed. The resulting system of equations is a set of partial differential equations

$$\frac{\partial p}{\partial t} = \frac{-1}{q} \frac{\partial j_p}{\partial x} - R(n, p) + G(x, t), \quad (4.9) \quad j_p = -qD_p \left(\frac{\partial p}{\partial x} + \frac{qp}{k_B T} \frac{\partial\Phi}{\partial x} \right), \quad (4.10)$$

$$\frac{\partial n}{\partial t} = \frac{1}{q} \frac{\partial j_n}{\partial x} - R(n, p) + G(x, t), \quad (4.11) \quad j_n = qD_n \left(\frac{\partial n}{\partial x} - \frac{qn}{k_B T} \frac{\partial\Phi}{\partial x} \right), \quad (4.12)$$

$$\frac{\partial P}{\partial t} = \frac{-1}{q} \frac{\partial j_P}{\partial x}, \quad (4.13) \quad j_P = -qD_{ion} \left(\frac{\partial P}{\partial x} + \frac{qP}{k_B T} \frac{\partial\Phi}{\partial x} \right). \quad (4.14)$$

They are coupled by the electrostatic potential resulting from all charges present in the system. One obtains the following equation by solving another partial differential equation, known as Poisson's equation

$$0 = \frac{\partial^2\Phi}{\partial x^2} - \frac{q(N_{ion}(x) - P(x) + n(x) - p(x) + \hat{p} - \hat{n})}{\varepsilon}. \quad (4.15)$$

The symbols \hat{n} , \hat{p} and ε represent a homogeneous charge distribution of ionized n - or p -dopants and the dielectric constant, respectively. The recombination rate R in Equa-

tion 4.11 and 4.9 is modeled as the sum of Shockley-Read-Hall (Equation 3.18) and radiative recombination (Equation 3.16). Thus, the mathematical model used for the simulations can be treated as essentially equivalent to that used by Courtier et al.^[136,178].

4.4.2 Courtiers numerical scheme

The set of Equations 4.9 to 4.15 are solved by a finite element approach developed by Courtier et al.^[136,178], which they specifically tailored for modeling perovskite solar cells. In this scheme the solar cell is described as a three layered system, that satisfies a set of continuity conditions for Φ , E and $j_{n,p,P}$ at the interfaces, as described in Figure 4.7. For simplicity, the sequence of layers from left to right is defined as ETM-Perovskite-HTM, which keeps the notation consistent with section 3.3.3 where quantities evaluated on the left / right side of the interface are indicated with \leftarrow/\rightarrow . The spatial domains of the respective layers are also shown in Figure 4.7, where the ETM layer with thickness d_E is located at $x \in [-d_E, 0]$, the perovskite with thickness d at $x \in [0, d]$ and the HTM with thickness d_H at $x \in [d, d + d_H]$. Thereby, the model is simplified taking the following central approximations into account:

- The perovskite layer is fully intrinsic
 $(\hat{n}|_{x \notin [-d_E, 0]} = \hat{p}|_{x \notin [d, d+d_H]} = 0)$.
- There are no mobile ions present in the transport layers
 $(P|_{x \notin [0, d]} = N_{ion}|_{x \notin [0, d]} = 0)$.
- The ETM/HTM is conductive for electrons/holes only
 $(j_n|_{x \in [d, d+d_H]} = n|_{x \in [d, d+d_H]} = j_p|_{x \in [-d_E, 0]} = p|_{x \in [-d_E, 0]} = 0)$.
- In the transport layers no light is absorbed and no recombination takes place.
 $(R|_{x \notin [0, d+d]} = G|_{x \notin [0, d]} = 0)$.
- The charge carrier exchange across the interfaces of the respective layers is based on thermal emission and the principle of detailed balance. As a result, the charge carrier densities on the opposite sides have fixed ratios

$$\frac{\vec{n}}{\overleftarrow{n}} = k_E = \frac{\overleftarrow{N}_C}{\overleftarrow{N}_C} e^{\frac{\overleftarrow{E}_C - \overleftarrow{E}_C}{k_B T}}, \quad (4.16)$$

$$\frac{\overleftarrow{p}}{\overleftarrow{p}} = k_H = \frac{\overleftarrow{N}_V}{\overleftarrow{N}_V} e^{\frac{\overleftarrow{E}_V - \overleftarrow{E}_V}{k_B T}} \quad (4.17)$$

to each other.

- The photon flux enters the device via the front or back side of the device and is absorbed according the Beer-Lambert law

$$G(x, t) = F_{ph}(t)\alpha e^{-\alpha x}, \quad (4.18)$$

where the absorption coefficient α is assumed to be wavelength independent. The irradiated photon flux F_{ph} may additionally vary in time. The Beer-Lambert approximation implies that internal reflections are neglected.

- The electrodes of the solar cell are perfect ohmic contacts, so that no space charge is formed there.

Figure 4.7 also shows that the outer electrodes obey boundary conditions that pin the carrier concentration there to a value equal to the respective doping concentration. The electrostatic potential is subject to two boundary conditions as well. The first one at the ETM electrode pins the $\Phi|_{x=-d_E}$ to ground and through the second condition it is possible to simulate the application of an external voltage source

$$\Phi|_{x=d+d_H} = \overset{*}{\Phi}(t) = \frac{V(t)}{R_S(t)/R_P + 1} + \frac{j_n|_{x=-d_E}}{1/R_P + 1/R_S(t)} - \Phi_{BI}, \quad (4.19)$$

where Φ_{BI} is the built in potential defined by

$$\Phi_{BI} = E_C^E - E_V^H + k_B T \ln \left(\frac{\hat{n}^E \hat{p}^H}{N_C^E N_V^H} \right). \quad (4.20)$$

The superscripts E and H indicate that the values refer to the ETM or HTM respectively. Equation 4.19 extends Courtiers model by the possibility to include series and a parallel shunt resistance in the simulations. Additionally, there exists the option to make the series resistance a function of time, thus allowing also for the simulation of experiments where the operation mode is switched from open to short circuit conditions and vice versa, like in charge extraction or voltage biased OCVD. This approach, however involves

the additional approximation of negligible displacement currents at the outer electrodes which is consistent with the assumption of an ohmic contact there.

To finally solve this set of equations a non-dimensionalization is performed in a way that the variables are rescaled to values in the magnitude of 1 and a discretization is conducted over a non uniform grid leading to a system of coupled ordinary differential equations (ODEs) where the Poisson equation acts as an algebraic boundary condition.

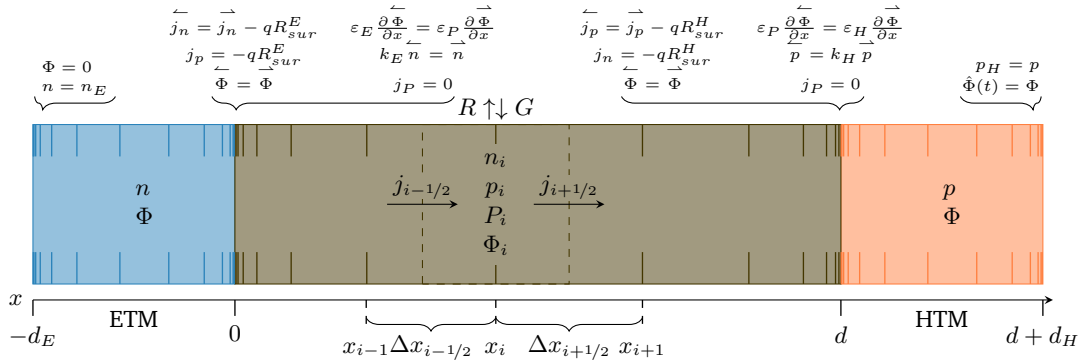


Figure 4.7.: Schematic representation of the perovskite solar cell model including its transport layers. The equations refer to the boundary and continuity conditions at the electrodes and interfaces. The discretization scheme uses a nonuniform grid with far denser sampling near the interface than in the bulk, in order to resolve the space charges there with sufficient accuracy and to avoid unnecessary computations for the bulk region. The \leftarrow/\rightarrow indicate that the quantities on left and right side of a ETM/Perovskite or a Perovskite/HTM interface has to be evaluated. Due to the discretization, the same quantities are only calculated in between two points of the grid, this is indicated by the subscripts $_{i\pm 1/1}$.

Non-dimensionalization

When solving systems of equations numerically, finite precision in the representation of floating point numbers in computers is a significant problem. This is especially true when some parts of the system have much larger values than others. In such a case, the small terms are essentially neglected when solving the system if their numerical value is many orders of magnitude below the largest values. If this happens the system is called ill-conditioned. If one would try to solve the equations numerically by specifying all constants and variables in SI base units, one would encounter exactly this problem. For instance, the carrier densities are easily above 10^{24} m^{-3} while the electrostatic potential

Φ takes values somewhere around 10^{-19} J. The aim of the non-dimensionalization is to transform the system of equations in a way that all values are in the order of 1 irrespective of the units in the input parameters. Courtier proposed for this purpose the transformations

$$\begin{aligned} x &= dx^*, & P &= N_{ion}P^*, & n &= \hat{n}n^*, \\ p &= \hat{p}p^*, & t &= \frac{b}{D_{ion}} \sqrt{\frac{k_B T \varepsilon_P}{q N_{ion}}} t^*, & \Phi &= \frac{k_B T}{q} \Phi^*, \\ j_p &= F_{ph}^0 (1 - e^{-\alpha d}) j_p^*, & j_n &= F_{ph}^0 (1 - e^{-\alpha d}) j_n^*, & j_P &= \frac{D_{ion} N_{ion}}{d} j_P^*, \end{aligned} \quad (4.21)$$

where F_{ph}^0 is the photon flux from AM1.5 irradiation. ε_P is the relative permittivity in the perovskite layer which might be different from the value in the HTM ε_H or ETM ε_E . By inserting these scalings into the Equations 4.9 to 4.15, a well-conditioned system is obtained with respect to the new starred variables (t^*, x^*, n^*, p^*, P^* and Φ^*). The non- and re-dimensionalization procedure is conducted automatically by the software implementation of the drift-diffusion simulator and does not require any interaction by the user. The star notation will be dropped for the rest of this section where all variables are treated as non-dimensionalized simplifying the further expressions.

Discretization

The perovskite layer is represented by a unevenly spaced grid with N points distributed in a tanh shape

$$x_i = \frac{\tanh(s(2i/N - 1))}{2 \tanh((s) + \frac{1}{2})}, \quad \text{for } i = [0 \dots N]. \quad (4.22)$$

The scaling parameter s defines how dense the interfaces are sampled. Analogous approach is taken for the grid of the HTM and ETM layer where the spacing is made approximately equal on both sides of the interface. The resulting grid is visualized in Figure 4.7. The final discretization is done by a finite element approach. This method is based on representing the variables n, p, P and Φ as linear combinations of piecewise linear basis functions with the property $\varphi_i(x) = 0$ if $x \notin [x_{i-1}, x_{i+1}]$. By multiplying the equations 4.9 to 4.15 with these basis functions and a subsequent integration over the entire spatial domain, a discretization is obtained which can then be solved numerically. The integrals over the highly nonlinear source terms R and G are approximated

by a procedure from the work of Skeel and Berzins^[180]. The complete derivation of the discretization is somewhat lengthy and described in great detail in [178]. However, since the result determines what type of solver can be applied to the problem and how the process of integrating the differential equation can be accelerated, the result of the discretization process must be discussed to some minimum extent. In the following this will be done exemplary on the non dimensionalized form of Equation 4.11 and 4.12 governing the dynamics of electrons by taking the results directly from [136].

4.4.3 Implementation

The non dimensionalized current densities are computed in the center of x_i and x_{i+1} , approximated by finite differencing. In case of Equation 4.12 this leads to the expression

$$\dot{j}_{n_{i+1/2}} = \frac{D_n \hat{n}}{F_{ph}^0 (1 - e^{-\alpha d}) d} \left(\frac{n_{i+1} - n_i}{\Delta x_{i+1/2}} + \frac{n_{i+1} + n_i}{2} \frac{\Phi_{i+1} - \Phi_i}{\Delta x_{i+1/2}} \right). \quad (4.23)$$

The currents contribute to the discretized conservation laws. In this case Equation 4.11 takes the form

$$\begin{aligned} \sigma \left(\frac{\Delta x_{i+1/2}}{6} \frac{dn_{i+1}}{dt} + \frac{\Delta x_{i+1/2} + \Delta x_{i-1/2}}{3} \frac{dn_i}{dt} + \frac{\Delta x_{i-1/2}}{6} \frac{dn_{i-1}}{dt} \right) = \\ \dot{j}_{n_{i+1/2}} - \dot{j}_{n_{i-1/2}} + \frac{\Delta x_{i+1/2}}{2} \left[G(x_{i+1/2}, t) - R\left(\frac{n_i + n_{i+1}}{2}, \frac{p_i + p_{i+1}}{2}\right) \right] \\ + \frac{\Delta x_{i-1/2}}{2} \left[G(x_{i-1/2}, t) - R\left(\frac{n_i + n_{i-1}}{2}, \frac{p_i + p_{i-1}}{2}\right) \right], \end{aligned} \quad (4.24)$$

with

$$x_{i\pm 1/2} = \frac{x_i + x_{i\pm 1}}{2}, \quad \Delta x_{i\pm 1/2} = \mp x_i \pm x_{i\pm 1}, \quad \sigma = \frac{\hat{n} D_{ion}}{F_{ph}^0 (1 - e^{-\alpha d})} \sqrt{\frac{q^2 N_{ion}}{k_B T \epsilon_P}}. \quad (4.25)$$

Similar expressions are derived for Equations 4.9 to 4.15. The left hand side of Equation 4.24 can be written as the matrix vector product $\left(\frac{\Delta x_{i+1/2}}{6}, \frac{\Delta x_{i+1/2} + \Delta x_{i-1/2}}{3}, \frac{\Delta x_{i-1/2}}{6} \right)_i \cdot \left(\frac{dn_{i+1}}{dt}, \frac{dn_i}{dt}, \frac{dn_{i-1}}{dt} \right)_i^T = f_i(\mathbf{n})$. By following [136,178] and writing all variables into one column vector

$$\mathbf{u} = (\mathbf{P}, \Phi, \mathbf{n}, \mathbf{p}, \Phi^E, \mathbf{n}^E, \Phi^H, \mathbf{p}^H)^T, \quad (4.26)$$

the discretized form of Equations 4.9 to 4.15 is expressed by a *mass matrix* \mathbf{M} and a vector function $\mathbf{f}(\mathbf{u})$ representing the right hand side of the equations as

$$\mathbf{M} \frac{d\mathbf{u}}{dt} = \mathbf{f}(\mathbf{u}, t). \quad (4.27)$$

By formulating the problem in this generic way it can be easily inserted in the most numerical solvers. However, Equation 4.15 does not contain any time derivative, causing \mathbf{M} to be singular, thus it can not be integrated via explicit methods. To perform the simulations, suitable starting conditions \mathbf{u}_0 are still required. In general, the steady state of the system is a good choice because it can be derived via the solution of $\mathbf{f}(\mathbf{u}_0, t_0) = \mathbf{0}$ by a nonlinear solver like `NLsolve.jl`^[181] or by integration of Equation 4.27 over a sufficient long time span using a consistent initial guess for \mathbf{u}_0 .

Implicit solvers

Figure 4.8a shows the structure of \mathbf{M} where all non zero elements are indicated by a square and the singular property becomes obvious. Such an algebraic differential equation must be either transformed to an ODE or integrated via implicit methods. Generally implicit methods are suited better for stiff problem but cause some additional overhead as they lead to a root finding problem. If the differential equation is solved by the implicit Euler method it takes the form

$$\begin{aligned} \mathbf{M}\mathbf{u}_{n+1} &= \mathbf{M}\mathbf{u}_n + \Delta t \mathbf{f}(\mathbf{u}_{n+1}, t + \Delta t) \iff \\ \mathbf{M}\mathbf{u}_{n+1} - \mathbf{M}\mathbf{u}_n - \Delta t \mathbf{f}(\mathbf{u}_{n+1}, t + \Delta t) &= \mathbf{0} = \mathbf{g}(\mathbf{u}_{n+1}). \end{aligned} \quad (4.28)$$

This shows already another beneficial property of implicit schemes. The algebraic part (those where the rows \mathbf{M} are empty) does not need an initial condition. In this scheme these are the variables for the electrostatic potential. To find \mathbf{u}_{n+1} for a given \mathbf{u}_n , Equation 4.28 can be solved iteratively by Newton's method

$$\tilde{\mathbf{u}}_{i+1} = \mathbf{M}\tilde{\mathbf{u}}_i - \mathbf{J}_g^{-1} \mathbf{g}(\tilde{\mathbf{u}}_i), \quad (4.29)$$

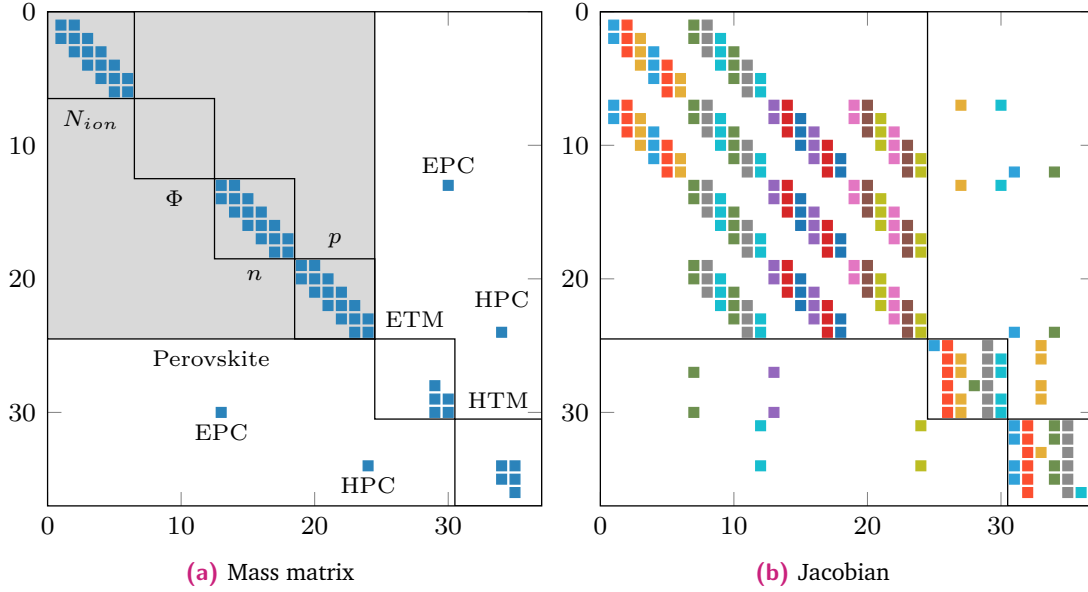


Figure 4.8.: Sparsity patterns from an example system with a perovskite layer grid size of 5. The non zero entries are represented by squares. For the mass matrix (a) the sub matrices for the individual layers and charge carriers are marked by labeled rectangles. The far off diagonal elements correspond to the ETM-Perovskite (EPC) and HTM-Perovskite (HPC) coupling terms. The sparsity pattern of the Jacobian is more dense. However, the different columns group the entries which can be computed simultaneously without leading to *perturbation confusion*. Exploiting this, the whole Jacobian can be computed by 12 function evaluations irrespective of the grid size.

where \mathbf{J}_g is the Jacobian matrix of g which is connected to the Jacobian matrix of f by

$$\mathbf{J}_g = \mathbf{M} - \Delta t \mathbf{J}_f. \quad (4.30)$$

From this equation it becomes clear that even if \mathbf{M} is singular \mathbf{J}_g likely is not and the Newton iterations in Equation 4.29 still lead to success so that $\tilde{\mathbf{u}}_{i \rightarrow \infty} = \mathbf{u}_{n+1}$. Since the root-finding problem is inherent to implicit methods (as long as f is not linear), it can be drastically accelerated by an efficient computation of \mathbf{J}_f . The efficiency aspect is especially important because \mathbf{J}_f actually has to be reevaluated after each step in the Newton iterations. For densely populated Jacobi matrices the computational complexity scales linearly with their size. However, the Jacobi matrix resulting from the discretization of Equations 4.9 to 4.15 is rather sparse (Fig. 4.8b) and a structural analysis reveals that it can be calculated by evaluating f along 12 specific orthogonal directions only, independent of the grid size. This approach is called Jacobian coloring and is elaborated in

detail in [182]. A possible choice for the different directions is indicated by different colors in Figure 4.8b, where columns of the same color represent one direction.

Automatic differentiation

The Jacobian is the matrix of directional derivatives of a vector function $(J_{ij} = \frac{df_i}{du_j})$. The simplest method calculating \mathbf{J} numerically is through finite differences. This method however suffers from a lack in accuracy while having a substantial computational overhead compared to other methods. For this reason the herein implemented drift-diffusion simulator takes derivatives by a concept called *automatic differentiation*. It involves a special type of numbers called *dual numbers*. They are defined similar to complex numbers by taking a real number and adding a dual part to it with the unit ϵ and the property $\epsilon^2 = 0$. By taking the Taylor series of a function along the direction of the dual part

$$f(x + \epsilon) = f(x) + \frac{df}{dx}\epsilon + \mathcal{O}(\epsilon^2), \quad (4.31)$$

one can see that dual part of the function value contains only the derivative of that function. Therefore, if such an expansion is available for all elementary functions it is possible to get an exact (within machine precision) derivative of any function composed of these elementary functions. For this purpose, the Julia package ForwadDiff.jl^[183] is used in this work, which implements this already. Another beneficial property of these numbers is, that it is possible to take derivatives along n different directions at once by a single application of the vector function \mathbf{f} to a multi-dimensional dual number

$$\mathbf{f}(\mathbf{u} + \mathbf{e}_1\epsilon_1 + \mathbf{e}_2\epsilon_2 + \dots + \mathbf{e}_n\epsilon_n) = \mathbf{f}(\mathbf{u}) + \frac{df_1}{du_1}\epsilon_1 + \frac{df_2}{du_2}\epsilon_2 + \dots + \frac{df_n}{du_n}\epsilon_n, \quad (4.32)$$

where $\mathbf{e}_1, \mathbf{e}_2, \dots, \mathbf{e}_n$ are the unit vectors along n directions. This way it is possible to calculate the whole Jacobian at once by taking the colored directions shown in Figure 4.8b.

Benchmarks

The herein implemented simulation tool is wrapped in a Julia package called AnnA.jl and is publicly available^[184]. It internally uses differential equation solvers provided by DifferentialEquations.jl^[185]. Since it is not clear which solver methods are best suited to

integrate this specific discretization of the partial differential equations, various benchmark tests are performed. There are two main parameters of interest, the time needed to solve and the relative error made. To determine the error, the time-averaged relative deviation of the solution at a given solver tolerance to a reference solution is determined. However, since no analytical reference solution is known, a numerical solution calculated with very restrictive tolerances (10^{-12}) is used for this purpose. It should be noted that relative (reltol) and absolute tolerance (abstol) can be specified separately. The relative tolerance is a measure of the relative uncertainty and defines the significant digits of the solution. The absolute error defines a cutoff level where a solution component can be neglected if it is below that value. In the benchmarks both tolerances were set to be equal ($\text{reltol} = \text{abstol}$). Figure 4.9a compares 6 different implicit solver methods

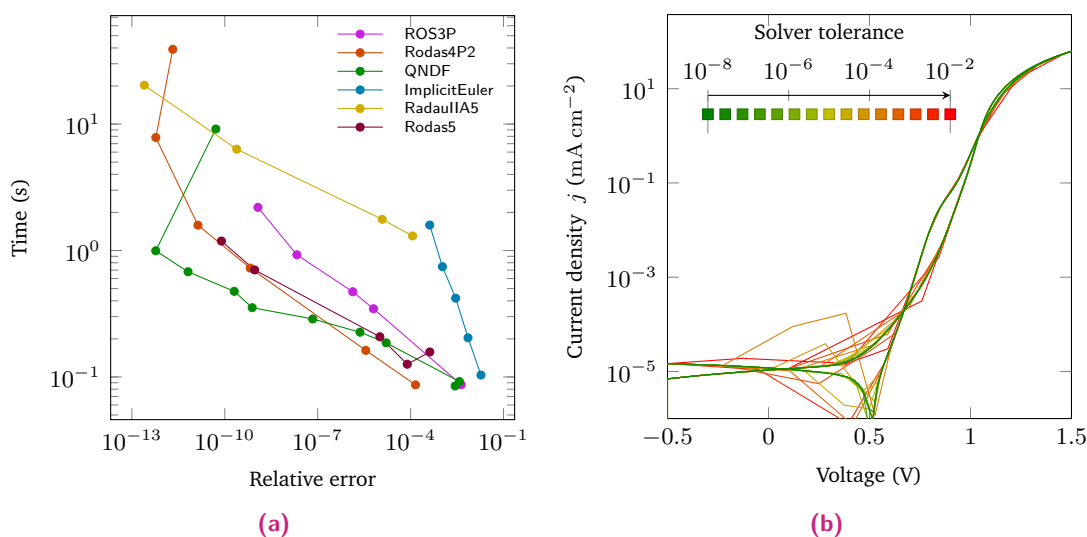


Figure 4.9.: Benchmark for j - V simulations with a grid size of $N = 200$. a) Running time versus relative error of different solution methods. Depending on the targeted error, the QNDF and Rodas4P2 methods represent the ideal choice. b) Rodas4P2 with different solver tolerances. For values of $\text{reltol}=\text{abstol}=10^{-5}$, even on a logarithmic scale, hardly any artifacts can be detected in the simulated j - V curve.

used by AnnA.jl, the ROS3P^[186], Rodas4P2^[187], Rodas5^[188], QNDF^[189], Implicit Euler and RadauIIA5^[190]. The QNDF and Rodas4P2 method show the best performance depending on the target error. From experience, it can also be said that the QNDF method requires well-defined and consistent initial conditions, whereas the Rodas4P2 algorithm tends to be less restrictive in this respect. Figure 4.9b shows simulations of a j - V characteristics on logarithmic scale using the Rodas4P2 method. At tolerances below 10^{-5} no significant numerical artifacts are visible. For illuminated characteristics, where the

current densities are in the mA cm^{-2} range, tolerances below 10^{-3} may already be sufficient. The actual performance depends slightly on the type of problem to solve, as it can

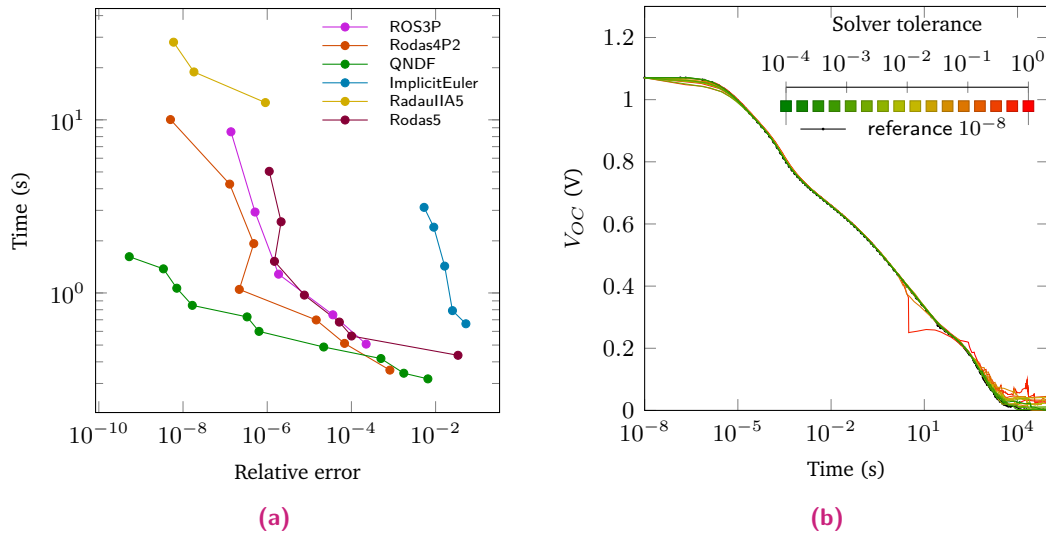


Figure 4.10.: Benchmark for OCVD simulations with a grid size of $N = 200$. a) Running time versus relative error of different solution methods. Depending on the targeted error, the QNDF and Rodas4P2 methods represent the ideal choice. b) OCVD simulated with Rodas4P2 using different solver tolerances. For tolerances below $\text{reltol}=\text{abstol}=10^{-3}$ the $V_{OC}(t)$ transient is essentially artifact free. High tolerances cause a noisy behavior near the steady state around 1×10^4 s.

be seen when comparing j - V simulations (Fig. 4.9a) to simulations of OCVD transients (Fig. 4.10a) the solvers perform differently but the QNDF and Rodas4P2 methods are still a good choice.

Besides the solver tolerances also the resolution of the spatial grid influences both accuracy and run time. The accuracy gain of a higher sampled space has to be paid by additional computational affords as the matrices get larger thus all operations involving matrix operations need more time. In Figure 4.11a the run time vs. grid size of the timings archived by this simulation tool using the Rodas4P2(—●—) and QNDF(—●—) integrators is plotted together with the timings presented by Courtier (—●—). Anna.jl shows an overall faster computation as well as a better (almost linear) scaling behavior over a wide range of grid sizes. It is important to note, that Courtiers timings are not directly comparable. This is because the solver tolerances of different integration methods do not necessarily lead to the same numerical errors. From the technical aspects the QNDF method provided by DifferentialEquations.jl should be functionally equivalent to MAT-

LABs ode15s solver.^[189] Additionally, the timings measured by itself were on different machines. Courtier however does not directly specify the hardware used to measure the timings, but that it was done “on a standard modern personal computer”^[136]. The results for AnnA.jl was archived on a AMD Ryzen 9 4900HS CPU (3.0 GHz) using a single thread and 16 GB DDR4 dual channel RAM at 3200 MHz. The considerable performance gain

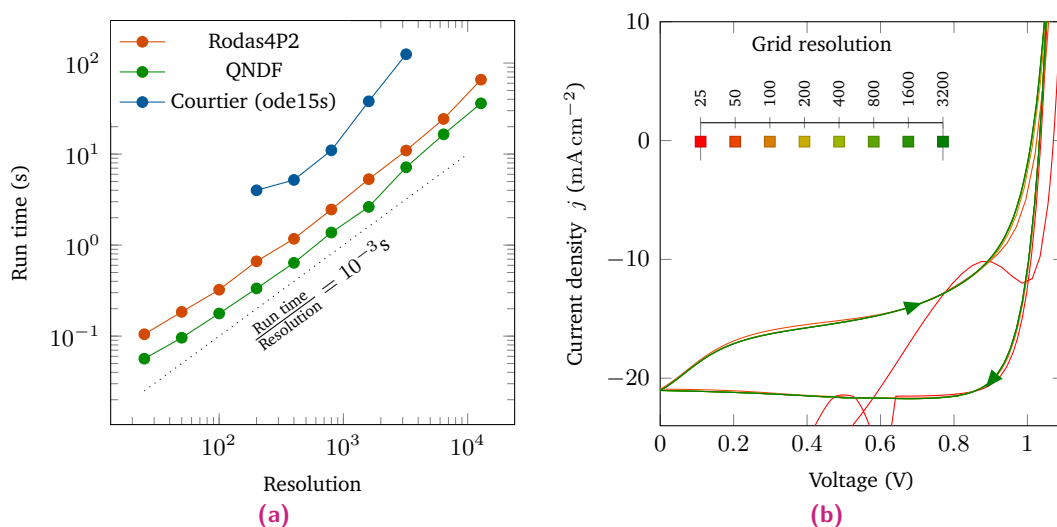


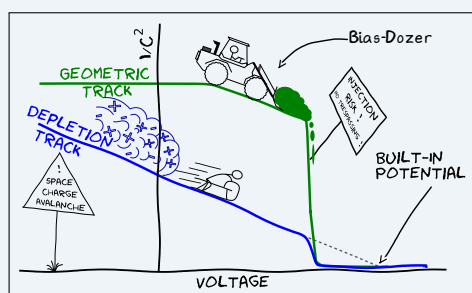
Figure 4.11.: a) Simulation protocol, parameters and tolerances ($reltol=10^{-6}$ and $abstol=10^{-8}$) were chosen equal to those used by Courtier^[125,136] in her benchmarks. The resolution refers to the number of grid points in the perovskite layer. b) The j - V characteristics obtained by AnnA.jl do match the ones obtained from Courtiers implementation^[125]. Numerical artifacts appear only for a grid resolution below 50 points (with Rodas4P2). Timings presented by Courtier —●—

compared to Courtier’s implementation in MATLAB is also due to the fact that AnnA.jl is written in Julia, which, unlike MATLAB, executes fully compiled code. The necessary compile time is not taken into account in the benchmarks, since this is no longer a factor in the repeated execution of simulations. This is of particular relevance when many consecutive simulations are carried out, as in the case of fitting measurement data or explorative studies in which the influence of various parameters is investigated based on the model. In such cases it is also good practice to work with large tolerances and small grid resolutions and to verify the results with small tolerances on a high-resolution grid at the end, to detect possible numerical artifacts and errors. AnnA.jl is additionally written in a thread save manner so that it is possible to do many simulations in parallel on a multiple core CPU or a computing cluster.

Ionic contributions to Space Charge Behavior

ABSTRACT:

The difficulty in studying electronic properties of solar cells results from the screening effects as well as slow dynamics of mobile ions, particularly if they are located at the interfaces. Herein, the distribution of charged species in planar-type MAPbI₃ is addressed, as well as FAPbI₃ solar cells by using a modified capacitance-voltage (*CV*) method without illumination in combination with a Mott-Schottky (*MS*) analysis of experimental data. The characteristic *MS* behavior with a linear dependence of $C^{-2}(V)$, distinctive for a pn-junction, is not visible in pristine devices. Surprisingly, biasing the device in the forward direction results in *MS* behavior, which is due to the field-driven redistribution of mobile ions from the interface toward the absorber bulk. From the *MS* analysis, space charge concentrations of $2.5 \times 10^{16} \text{ cm}^{-3}$ and $2.8 \times 10^{16} \text{ cm}^{-3}$ for the FAPbI₃ and the MAPbI₃ devices are deduced, respectively. However, the junction formation effect is not sustainable, since mobile ions relax to their initial location at ambient conditions. However, if the prebiasing is done at temperatures slightly below room temperature, the pn-junction can be stabilized for the FAPbI₃ device. In contrast, the MAPbI₃ device shows a rapid redistribution of mobile ions back to the transport layers during the measurement even at lower temperatures. This can be observed in the quite different doping profiles for the two perovskite devices.



This chapter is partially based on:

Doping Profile in Planar Hybrid Perovskite Solar Cells Identifying Mobile Ions

M. Fischer, K. Tvingstedt, A. Baumann and V. Dyakonov. ACS Appl. Energy Mater. 2018, 1, 10, 5129-5134, DIO:[10.1021/acsaem.8b01119](https://doi.org/10.1021/acsaem.8b01119)

5.1 Introduction

In order to design new solar cell architectures, detailed knowledge about the material properties is required. Despite the well-known fact that doping of solar cells is a fundamentally important property, little attention has been spent on the doping concentration and distribution in perovskite solar cells. It has, however, been noted that the preparation methods may have an impact on the final doping distribution of the perovskite absorber.^[191] Thus, very different interface physics is expected depending on whether the formation of the perovskite absorber takes place on top of a charge selective layer or vice versa, or whether the perovskite is formed via thermal evaporation or via solution processing. The formation of detrimental defects at the interface of the perovskite may not only reduce the solar cell parameters due to interfacial nonradiative recombination but also lead to the formation of charged defects such as iodine vacancies (V_I) and iodine interstitials or methylammonium vacancies (V_{MA}).^[63,192] Especially, the iodine vacancies and interstitials have been proposed to be mobile within the perovskite absorber due to a low activation energy and high diffusion rate.^[193] While it is still under debate whether the hybrid perovskites should be considered as p- or n-type or even as an intrinsic semiconductor, the presence of mobile ions in the perovskite absorber is considered to affect the device performance strongly. In this matter, the almost omnipresent current-voltage hysteresis is assigned, at least partly, to the presence of mobile ions in the perovskite.^[194] In general, mobile ions are among the most discussed issues in the field, and they are frequently made responsible not only for current-voltage hysteresis but also for device degradation or inverted photocurrent transients which are assigned to be direct evidence for field screening in the device.^[33,48,49,62,132,195–199] The origin of ionic transport is still under debate, and transport of iodine, methylammonium, or even protons is proposed.^[62–64] Such mobile ions will follow a diffusion potential gradient within the perovskite device. Hence, the ion distribution in hybrid perovskites can also be considered as a space charge distribution. When accumulating at the interface in the vicinity of the transport layer, this space charge will lead to a screening of the built-in potential which generally makes the interpretation of the capacitance-voltage behavior of solar cell devices extremely difficult.^[191]

5.2 Mott-Schottky analysis

A well-established experimental technique to study the space charge distributions in semiconductors, e.g., formed by a junction capacitance, is the Mott-Schottky analysis based on capacitance-voltage characteristics (C - V) measurements. The $C(V)$ behavior can be understood by integrating the Poisson equation and treating the device as a plate capacitor. From the MS analysis, it is possible to determine directly the minority space charge concentration (N_{SC}) as well as parameters such as the built-in potential (V_{BI}) according to

$$C_D(V) = \left[\frac{-2\varepsilon(V - \Phi_{BI})}{qN_{SC}} \right]^{-1/2} \quad (5.1)$$

with the elementary charge q , the dielectric constant $\varepsilon = \varepsilon_0\varepsilon_r$, and the vacuum permittivity ε_0 . A prerequisite, however, is a clear identification of the linear $C^{-2}(V)$ MS region, i.e., the buildup of a depletion layer in the bulk or at the interface, which fulfills the MS equation.^[118] In classical semiconductor devices with a pn- or Schottky-junction, the capacitance-voltage dependence is typically governed by the formation of a depletion (or space charge) layer between the p- and n-doped regions of the semiconductor and/or metal. The region, where no free charge carriers are present, behaves as an insulator and is defined by the density of ionized dopants. This causes a certain capacitance C_D which is in addition governed by the depletion layer width W_D and the dielectric properties of the material according to Equation 5.1. From the MS plot of the reciprocal square of capacitance $C(V)^{-2}$ versus voltage, the built-in potential can be determined by the linear extrapolation toward voltage axis from the intercept. This method, however, is restricted such that it can only be applied as long as no free electrons and/or holes are injected into the solar cell. Only in this case can the contribution of diffusion capacitance $\propto J$ be neglected.^[64] In perovskite solar cell devices, the applicability of MS analysis is challenging. With a typical active layer thickness of around 300 to 500 nm and the fact that most of the perovskite semiconductors are believed to be rather intrinsic or at least not very heavily doped, the solar cell absorber layer is most likely fully depleted. The built-in potential in this case is then ruled by the work function difference of the contact materials. Another prerequisite for having a linear $C(V)^{-2}$ dependency in MS analysis is that the dopants (space charges) are homogeneously distributed in the bulk of the material.^[106,118] However, in the case of the hybrid perovskite semiconductors, it has to be considered that mobile ions are very likely to be present and possibly redis-

tributed when an external voltage is applied on a time scale of several seconds, which will also lead to a change in the space charge distribution. Since it is unclear to what extent the redistribution of mobile ions can influence the overall charge carrier density in the active material, it is appropriate to differentiate between doping density, free charge carrier density, and space charge density in this case as all space charges, including ions, must be considered in context of the Poisson equation which then delivers the built-in potential. In this work, the slow dynamics of charge redistribution in hybrid perovskites is used to the benefit of affecting and probing the space charge profile formed at a particular voltage applied externally. Planar hybrid perovskite solar cells with two different perovskite absorbers, namely, MAPbI₃ and FAPbI₃, are fabricated. PTAA as a hole transport layer and PCBM/C₆₀ as ETM with BCP and gold as top contacts is used. Further details about the preparation of solar cells can be found section 4.2. The j - V characteristics of the fabricated devices are shown in Figure 5.1. Both devices are subject to a moderate current voltage hysteresis. To do accurate C - V characteristics measured first

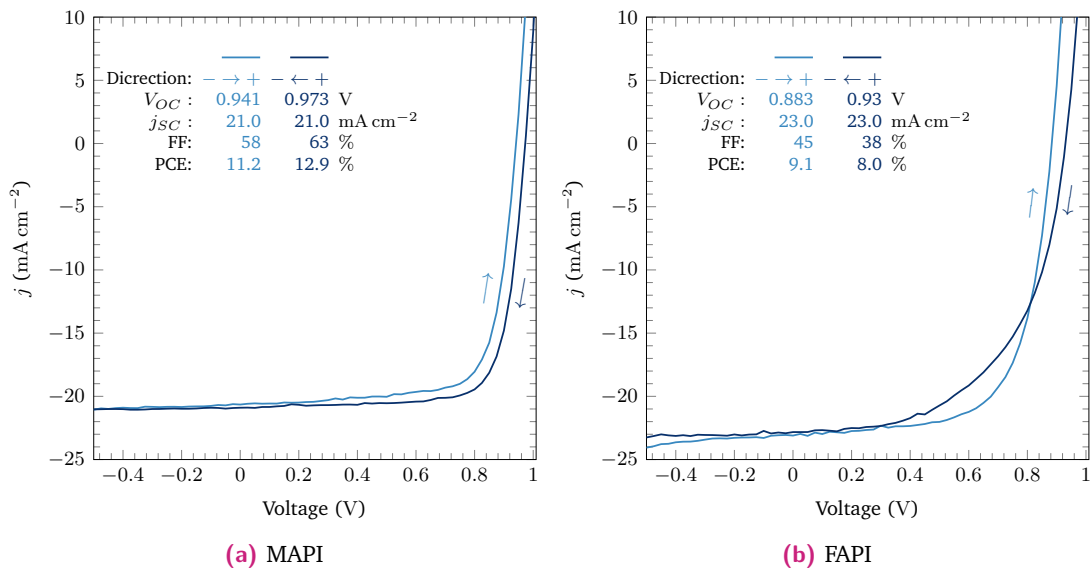


Figure 5.1.: j - V characteristics illuminated by 1 Sun irradiance. The solar cells are based on a) methylammonium lead iodide and b) formamidinium lead iodide. The FAPbI₃ device shows an increased j_{SC} , but decreased V_{OC} due to the lower band gap energy compared to MAPbI₃. The forward sweep (—) and backward sweep (—) were recorded using a scan rate of 200 mV s⁻¹.

the frequency dependency of the dielectric function of the two devices is investigated as shown in Figure 5.2. Like it is outlined in section 4.3.1 a frequency where the dielectric losses are minimal is chosen for accurate and fast capacitance measurements, this

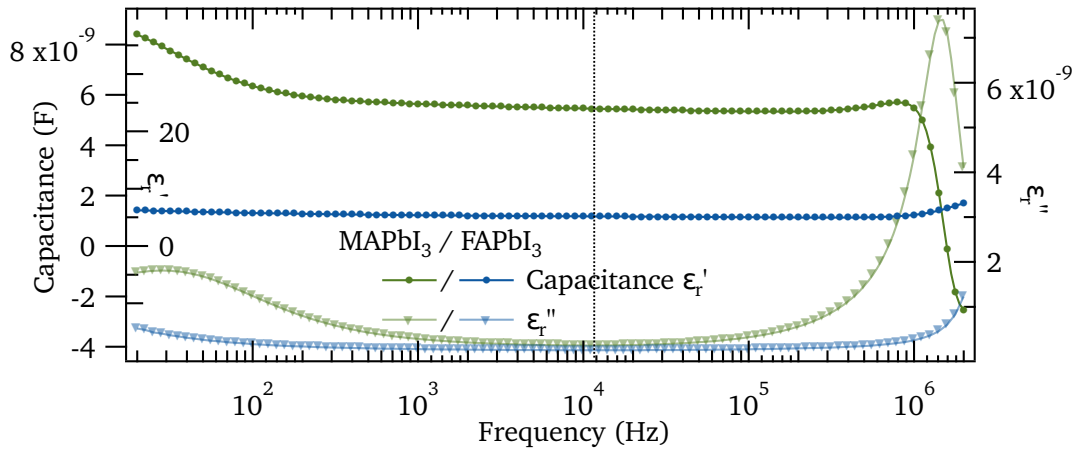


Figure 5.2.: Frequency dependent capacitance and relative permittivity (left axes) of the investigated devices at 0 V bias. For both materials the dielectric losses (right axes) are minimal at around ≈ 10 kHz at 300 K.

is the case at ≈ 10 kHz. By this the relative permittivity of MAPbI₃ and FAPbI₃ is determined to be 24 ± 1 and 5 ± 1 respectively. The errors include uncertainties regarding the thickness of the layers and the influence of the thin but existing transport layers. The standard C - V measurements were conducted by sweeping the voltage in forward direction from -0.4 to 1 V while keeping the frequency constant at 10 kHz and the AC-voltage amplitude to 20 mV. All capacitance measurements were done in C_S mode according to Table 4.1. Further details on the C - V measurements are provided in section 4.3.1. In both types of devices, a nearly voltage-independent capacitance in the range between -0.4 to 0.6 is observed, as can be seen in Figure 5.3a. This is consistent with the assumption of an intrinsic perovskite layer with the capacitance being essentially ruled by the thickness of the device which is then fully depleted. However, space charges at the contacts or transport layers as are often reported for hybrid perovskite solar cell devices^[195] and assigned to charged defects such as iodine and methylammonium vacancies or interstitials would also lead to a capacitance which only slightly changes with voltage. In this case, the ions screen the external electric field hindering the latter from penetrating into the bulk of the perovskite. The range above 0.6 V is dominated by charge carrier injection, which means that Equation 5.1 is no longer valid. As the $C(V)^{-2}$ relation is not observed in the C - V measurements shown in Figure 5.3a, a direct employment of Equation 5.1 would lead to nonrealistic values of both N_D or V_{BI} . To put in perspective the validity of the Mott-Schottky analysis to doped semiconductors and to compare it to

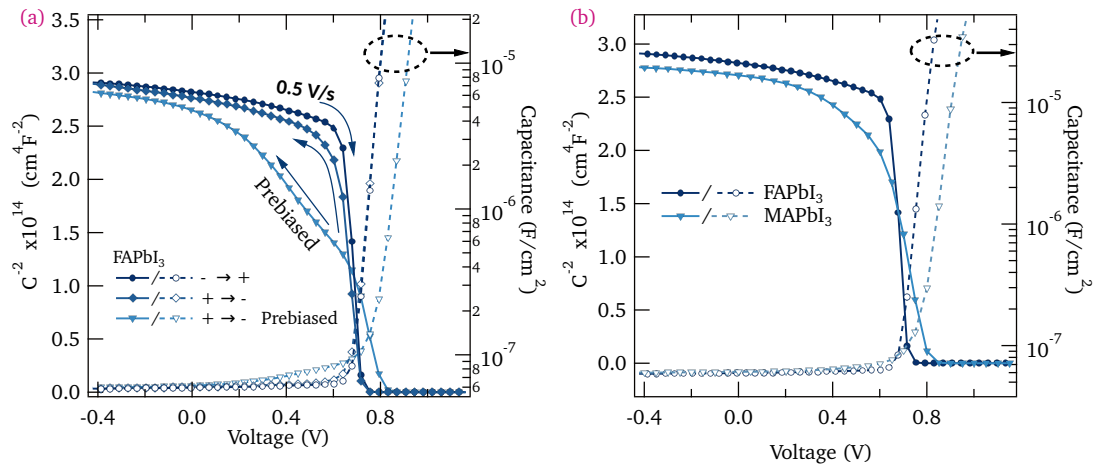


Figure 5.3.: a) $C(V)^{-2}$ (left axes) and $C(V)$ (right axes) of a FAPbI₃ and MAPbI₃ devices. b) Forward, reverse, and reverse with prebias cycle of the FAPbI₃ device. The voltage used for prebias was 1.5 V applied for 20 s.

the hybrid perovskites studied here, C - V scans on a standard Hamamatsu silicon photodetector are performed. The results are shown in Figure 5.6. Further, the capacitance remains voltage-independent for both forward and backward sweeps with only a slight hysteresis being visible in Figure 5.3b.

However, the situation changes drastically when applying a forward voltage (further on called prebias) of more than 1 V for 20 s prior to the C - V scan, followed by a 0.5 V s^{-1} fast C - V scan in the reverse direction (from the prebias voltage to -0.4 V). As can be seen in Figure 5.3b, an MS region begins to become visible and more and more pronounced when the prebias voltage is further increased. This phenomenon is assigned to the formation of two corresponding space charge layers within the perovskite absorber layer when applying the external electric field to the sample. Interestingly, in an immediate forward scan after prebiasing, no MS behavior is visible and the C - V diagram looks identical to a C - V curve without prebias. This indicates that the formation of the space charge layers in the perovskite by the prebiasing procedure is a slow process taking some time in the second range. Also, vice versa, the established space charge distribution is not very persistent relaxing to its initial value, as shown in the C - V plot in the subsequent scan in the forward direction. Taking the thermal dependence of ion motion into account, we lowered the sample temperature to 280 K and performed again the same set of experiments with the intention to prolong the persistency of the

formed spaced charge region. The same behavior as for 300 K is observed, however, now indeed with a much more stable formation of the MS region during the time of C - V measurement. Therefore the observed dynamic phenomenon is assigned to the presence of mobile ions. A schematic illustration is shown in Figure 5.4 which visualizes the hypothesis. A possible built-in potential created by the electron and hole transport material (ETM/HTM) will drive diffusion of mobile charges along the potential gradient, which also includes mobile ions. Under short circuit conditions, ions present in the perovskite absorber will move toward the respective transport layers. As the ETM (HTM) can be considered nonconductive for ions, an accumulation of the latter will occur at the interface to the respective transport materials, i.e., anions at the ETM and cations at the HTM (see Figure 5.4b). The accumulated ions will thus lead to the often-reported screening of the built-in potential.^[191,200] When a bias is applied in the forward direc-

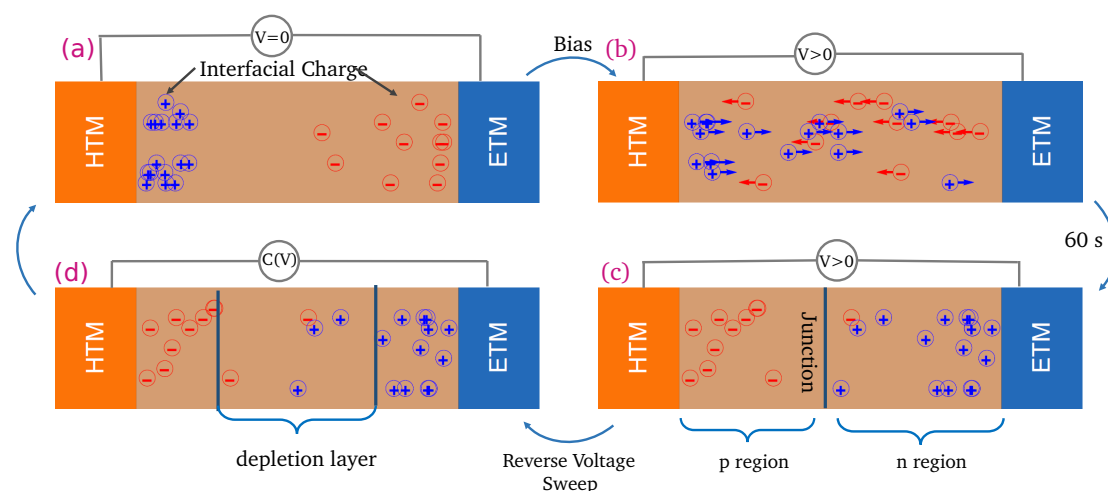


Figure 5.4.: a) Schematic representation of the redistribution of mobile ions in the perovskite absorber. a) Ions at the interfaces does not allow the observation of a depletion layer capacitance. b) Forward bias redistributes mobile ions. c) When the applied bias is sufficiently long, a junction is created in the perovskite absorber, d) Depletion layer capacitance is measured with reverse voltage sweep. Low forward voltage only reduces the number of ions accumulated at the interface. If the forward voltage is high enough, a space charge zone is built up over the bulk,^[201] showing a linear $C(V)^{-2}$ behavior.

tion, the ions are distributed within the perovskite; most importantly, they are removed from the perovskite/transport layer interface. With respect to recent publications reporting defect migrations, iodine vacancies obey a relatively low activation energy of about 0.1 to 0.6 V and are therefore considered to be very mobile. Moreover, the methylam-

monium vacancies VMA with a reported activation energy of 0.5 to 0.84 V are another type of defect which is believed to be mobile, although on the time scale of milliseconds to seconds only.^[202,203] Depending on the magnitude of the applied prebias as well as its duration, the charged defects may be pushed from the respective interface into the bulk of the perovskite to form a junction capacitance inside the perovskite absorber, as in a typical pn-junction defined by a space charge concentration and a V_{BI} . The letter does imply a difference in the chemical potential between the n and p side of the junction originating from a local change in equilibrium charge carrier concentration. Thus, the findings can be understood as a bias induced self-doping effect of the perovskite absorber by ion redistribution. Consequently, by measuring the capacitance-voltage behavior under reverse bias, a voltage-dependent depletion capacitance can be observed. It has to be noted that in such a generated pn-junction it is expected that positive and negative space charges are present in equal densities which requires a correction by a factor of $1/2$ when determining the space charge density. After the prebias is removed from the device, the ions start to redistribute within the perovskite layer, until a state of equilibrium is reached, which corresponds to the initially accumulated charges at the edge of perovskite absorber. An important note here is that additional stationary dopants in the perovskite layer in the same or even greater amounts than the mobile ions are unlikely, because the space charge layer would form at the interface and show MS behavior without applying prebias. Assuming a thermally activated motion of the ions in the perovskite, it is obvious that with decreasing the temperature the ion motion is lowered which will also lead to a slower redistribution of the ions after removal of the prebias voltage. In this case, already reducing the temperature by 20 K made it possible to measure the capacity of the depletion layer before the ions began to redistribute.

In the following, the junction capacitance in the FAPbI₃ as well as in a MAPbI₃ solar cell device are studied by performing C - V measurements at 280 K by applying a 2 V forward bias for different durations and then performing a 0.5 V s^{-1} fast C - V sweep in the reverse direction. In the FAPbI₃ device, the MS region at 280 K is much more pronounced compared to the room temperature measurement, as shown Figure 5.5. Carrying out fast C - V scans every 10 s during prebiasing, it is possible to monitor the change in the space charge region in time. It is seen that, after 30 s of prebiasing, a saturation is reached and the device in this state shows an almost ideal $C(V)^{-2}$ dependence. According to Equation 5.1 an average space charge concentration of $(2.5 \pm 0.1) \times 10^{16} \text{ cm}^{-3}$ and a built-in potential of $V_{BI} = (1.3 \pm 0.1) \text{ V}$ can be deduced for the FAPbI₃ device. This V_{BI}

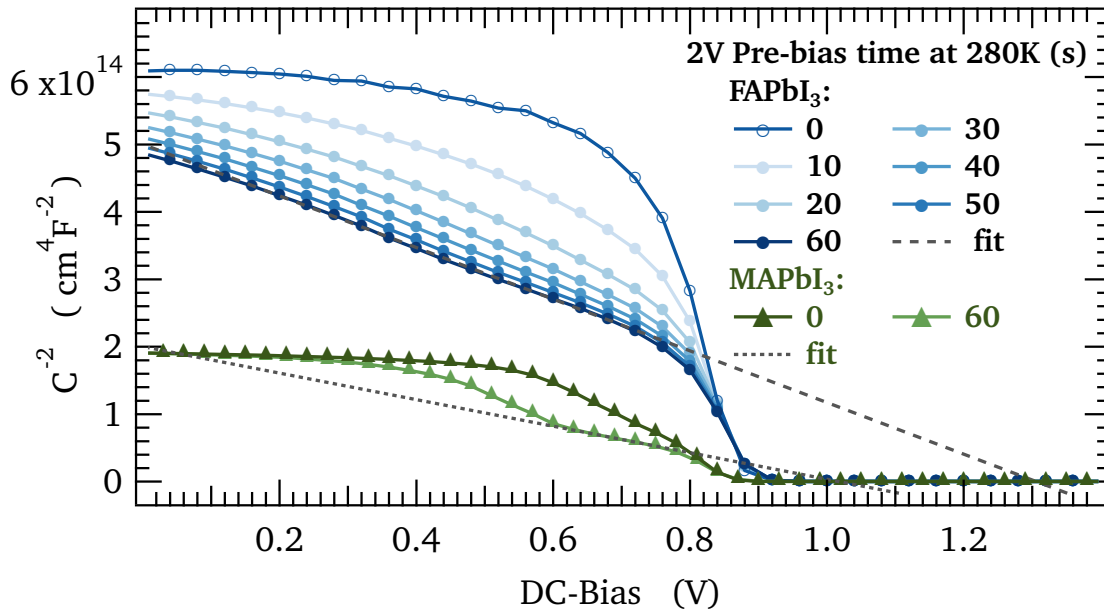


Figure 5.5.: (a) Mott-Schottky plots for the FAPbI₃ (●) device when different prebias durations are applied. The depletion layer capacitance becomes visible when a forward bias is applied for more than 30 s; in the case of MAPbI₃ (▲) the change is less pronounced.

and space charge concentration are thus far more realistic than what is obtained for the device without the application of a prebias voltage, which may easily result in concentration in the order of 10^{18} to 10^{19} cm^{-3} when blindly fitting the slope of the almost constant capacitance. The concentration in the range of 10^{16} cm^{-3} , however, fits well with values obtained for doped semiconductors as found also for the Si photodiode (see Figure 5.6). However, we note here that in silicon of course the dopants are most likely stationary and not mobile like in the mixed ionic-electronic perovskite semiconductors.

In the case of the MAPbI₃ sample, the situation is however not so clear. After a prebias applied to the MAPbI₃ device for 60 s, an MS region becomes visible in the C - V sweep from positive to negative voltage. Interestingly, the $C(V)^{-2}$ dependence shows two linear regions with different slopes Figure 5.5. The almost constant capacitance in the voltage range from 0 to 0.4 V is solely ruled by interfacial charges leading to values close to the purely geometric capacitance. By fitting the two slopes, i.e., in the voltage range from 0.4 to 0.6 V and from 0.6 to 0.8 V, it is obvious that only the slope in the latter voltage range results in meaningful parameters of $V_{BI} = (1.0 \pm 0.1) \text{ V}$ and $N_{SC} = (2.8 \pm 0.1) \times 10^{16} \text{ cm}^{-3}$.

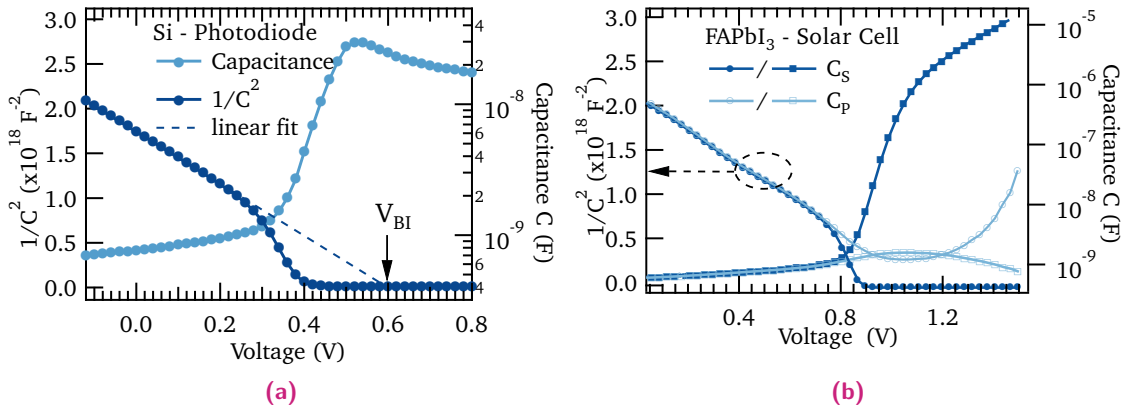


Figure 5.6.: $C(V)^{-2}$ (left axes) and $C(V)$ (right axes) of a) a Hamamatsu Si photo detector and b) the FAPbI₃ device after prebias treatment. C_S and C_P mode give the same result as long the device is in operates in the low injection regime.

The change of the $C(V)^{-2}$ dependence is assigned in the intermediate voltage range (0.4 to 0.6 V) to the ion redistribution back to the contacts/transport layers which lead to the field screening effect. It has to be noted here that it is not possible to exclude that the fast redistribution of the ions already influences the slope in the MS region between 0.6 V and 0.8 V and hence the extracted V_{BI} and N_{SC} . Thus, the values represent a lower estimate. Interestingly, this redistribution of ions in the MAPbI₃ happens on a faster time scale compared to those in the FAPbI₃ device. Assuming that the moving ions are iodine vacancies on one hand and FA and MA ion vacancies on the other hand, we hypothesize that the positively charged FA vacancies move more slowly compared to the MA vacancies which is in agreement with the reported higher activation energy for migrating FA vacancies.^[204] However, from the given set of data a final conclusion cannot be made here and left open for future studies.

5.3 Capacitance profiling

Finally, the capacitance profile, i.e., the density of space charge as a function of the depletion width $N_{SC}(W_D)$, can be determined from the C - V measurements. The space charge concentration $N_{SC}(W_D)$ can be calculated from the reciprocal voltage derivative of $C(V)^{-2}$ according to Equation 5.1. Thereby, the change in capacitance is attributed to a change in the extent of the space charge region, using the relationship of a paral-

parallel plate capacitor, where A is device active area and $W_D(V)$ is the voltage-dependent depletion layer width. The value for ϵ_r was determined by measuring the capacitance of the fully depleted solar cell at 0.5 V reverse bias. The measured capacitance C as a function of the frequency f is shown in Figure S3. The constant plateau at this frequency for both devices present at 10 kHz can be assigned to the geometric capacitance due to dielectric relaxation of the bulk, [124,191,205,206] resulting in a relative dielectric constant of 24 for MAPbI₃ and 15 for FAPbI₃. In Figure 5.7, the capacitance profile is shown for both types of devices. For comparison, the depletion width W_D is normalized to the perovskite layer thickness which was measured to be 300 nm/320 nm in the case of the FAPbI₃/MAPbI₃ device by using a profilometer. The whitened part of the capacitance

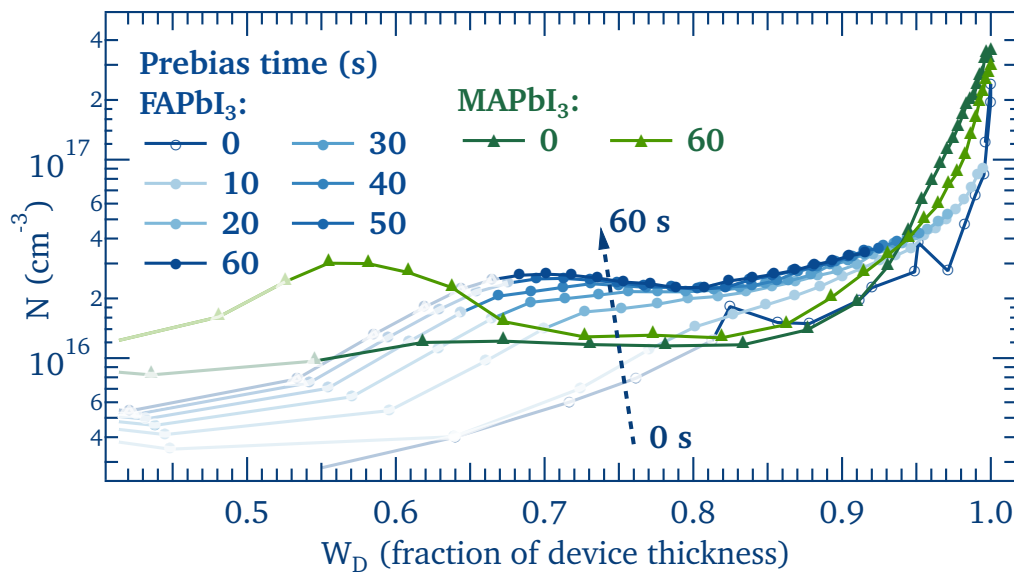


Figure 5.7.: Capacitance profile of both devices. The minimum seen in the MAPbI₃ is assumed to be caused by ionic redistribution during the measurement.

profiles in Figure 5.7 again correspond to charge carrier injection (see, e.g., Figure 5.5 for $V > 0.8V$) which shrinks and finally diminishes the pn-junction in the bulk and thus represent a limitation in the resolution of the profile. For both devices, it is found that charge carriers are initially located at the interface to the transport layers in which case the electric field is screened and thus N_D is large at $W_D = 1$ (W_D equals sample thickness) dropping quickly for $W_D < 1$ as can be seen in Figure 5.7. When a prebias is applied to the device, mobile charges are pushed into the bulk of the perovskite which is visible in a decrease of N_{SC} at $W_D = 1$ and a simultaneous increase of N_{SC} for $W_D < 1$.

With increasing duration of the prebias condition, the space charge concentration N_{SC} increases in the bulk and can be shrunk further by the C - V scan until it reaches a saturation. For the FAPbI₃ device, N_{SC} saturates at $2.5 \times 10^{16} \text{ cm}^{-3}$ at a depletion layer width of 68% of perovskite layer thickness whereas in the case of the MAPbI₃ a concentration of $2.8 \times 10^{16} \text{ cm}^{-3}$ at W_D of around 55% of perovskite layer thickness is reached. Comparing the shape of the two doping profiles, a clear difference can be observed. On one hand, the capacitance profile in the FAPbI₃ device shows an almost constant ion concentration of $2.5 \times 10^{16} \text{ cm}^{-3}$ for a wide range of varying depletion widths from 70% to 90% of the perovskite layer thickness indicating the rather uniform formation of the junction capacitance in the FAPbI₃ device. For the MAPbI₃ device, however, a minimum in the profile can be observed from 60% to 90% of the perovskite layer thickness. This minimum corresponds to the slope in the MS plot in Figure 5.5 at lower voltages. As discussed above, only the slope at high voltages leads to meaningful parameters. Again, the slope at lower voltages ($V < 0.4\text{V}$) is assigned to a transition from the MS region toward the almost voltage-independent $C(V)^{-2}$ region which appears in the MAPbI₃ device already during the C - V measurement. This is associated with a rapid redistribution of mobile ions back to their original position at the transport layer interface.

5.4 Conclusion

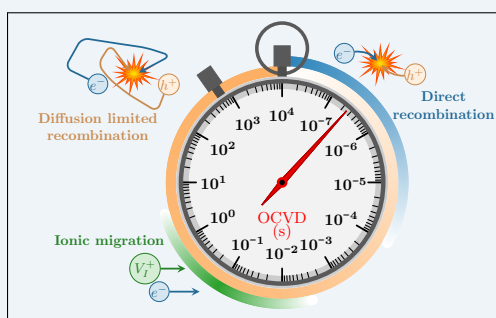
This work demonstrates that capacitance-voltage measurements can be used to identify mobile ion concentration in perovskite solar cell devices. In both MAPbI₃ and FAPbI₃ devices, it was possible to determine ion concentration by means of MS analysis when a prebias was applied to the device prior to the C - V scan, which pushes ions from the interface toward the bulk forming a pn-junction in the perovskite absorber. Concerning hybrid perovskites as mixed electronic-ionic conductors, the analysis of the ion concentration and its impact on the performance of optoelectronic devices in general becomes more and more relevant for a complete understanding and controlled improvement of those devices. In conclusion, two different hybrid perovskite planar p-i-n solar cells based on MAPbI₃ and FAPbI₃ as active layers were studied. C - V measurements were performed in order to determine the space charge carrier density by using the Mott-Schottky analysis. When applying a prebias to the solar cells up to 60 s and 2 V in the forward direction, we observed a hysteresis in the C - V sweep indicating MS behavior

(a linear $C(V)^{-2}$ dependence) in the first sweep from backward to forward directions which disappeared during the immediate forward sweep. However, when cooling down to 280 K, we find a more stable MS behavior in FAPbI₃ devices than in MAPbI₃ within the time of the $C-V$ measurement. The appearance of the MS region is attributed to the mobile ions being initially located at the transport layer interface which are pushed into the bulk of the perovskite when a forward prebias is applied. Consequently, a pn-junction is formed in the perovskite absorber. For the unbiased devices the value for the interfacial charge concentration on the order of 10^{17} cm^{-3} as well as their expansion are nominally in good agreement with findings from Belisle et al.^[195] made using photocurrent transients. The average concentration of the moving ion species is estimated to be in the range of $2.5 \times 10^{16} \text{ cm}^{-3}$ for FAPbI₃ and $2.8 \times 10^{16} \text{ cm}^{-3}$ for the MAPbI₃ device, which is in good agreement with values published by Cheng et al.^[199] The almost equal densities hint toward a common origin of the moving ions, most probably iodide which is present in the same stoichiometric concentration for both materials. The resulting capacity profiles showed that the space charge distribution reacts dynamically to the externally applied electric field. The work presented here gives a valuable insight into the properties of hybrid perovskite semiconductors for photovoltaic applications. With an established Mott-Schottky analysis, the space charge distribution in the semiconductor can provide important feedback for the device engineering when optimizing the individual layers and interfaces in the solar cell.

Ionic Traces in Transient Open Circuit Voltage Decay

ABSTRACT:

Traditional Drift-diffusion simulations have generally been employed to describe static steady-state conditions, whereas recently the transient counterpart has been able to reveal more detailed information regarding carrier kinetics. In addition to customary electron and hole dynamics, perovskite materials are known to also be strongly affected by the displacement of lattice vacancies, charged atoms or even entire molecules. Such ionic motion transpires on vastly different time scales compared to free charges and are generally not straightforward to simultaneously account for in one transient simulation tool. Here, based on coding in Julia, such a tool is developed and used accounting for both the fast dynamics of free charges subjected to radiative, Shockley-Read-Hall and surface recombination, simultaneously as the very slow displacement of ions is properly accounted for. It is shown that interconnected steady-state parameters such as V_{OC} and j_{SC} as well as transient experimental voltage decay measurements can be accurately reproduced by the simulations. The vast time window, ranging from sub-microseconds to hours, provided by high resolution open circuit voltage decay (OCVD) measurements combined with the steady-state parameters, is identified as a reliable gauge of artifact-free ionic dynamics in perovskite solar cells. With the knowledge gained from the simulations it is thus possible to provide a straightforward experimental method providing direct access to values of ion concentration, diffusivity as well as its thermal activation energy, parameters that are crucial for the future development and commercialization of perovskite-based photovoltaics.



This chapter is partially based on: Assigning ionic properties in perovskite solar cells; a unifying transient simulation/experimental study

M. Fischer, D. Kiermasch, L. Gil-Escrig, H. J. Bolink, V. Dyakonov and K. Tvingstedt. Sustainable Energy Fuels, 2021, 5, 3578, DIO:[10.1039/d1se00369k](https://doi.org/10.1039/d1se00369k)

6.1 Introduction

First experimental transient observations, employing both time and frequency domain techniques, have already confirmed a pronounced impact of slowly redistributing charge components.^[207–209] The most straight-forward electrical transient charge probing method is probably OCVD^[210,211] which simply measures the decay of the open circuit voltage after the charge-carrier generating light source has been switched off. Although the voltage decay measured with this technique certainly originates from the disappearance, or recombination, of the photo-generated excess charge carriers, the voltage decay rate cannot directly be linked to the charge carrier recombination rate, as also pronounced displacement and redistribution of electrons, holes as well as ionic species can occur on similar timescales.^[212–215] Only with detailed spatial and temporal knowledge of how excess charge carriers redistribute and recombine, is it possible to apprehend and determine correct carrier lifetimes and similar relevant material properties, such as e.g. diffusion constants of electrons, holes and ions. The essential spatial information of charge distribution in real solar cells is however usually never directly available from any experiment, but does become accessible via properly employed carrier drift-diffusion simulation tools.^[216–218] Usually, these methods are implemented in the steady-state and allow to access the spatial profile of both background and excess charge carriers at selected and specific quasi-static conditions such as e.g.; “in the dark”, “under illumination at open- and short circuit conditions or at *MPP*”. Recently, steady-state drift-diffusion simulations have also been carried out on perovskite solar cells, where the additional treatment of mobile ions needs to be accounted for.^[219–221]

Time-resolved drift-diffusion simulation capabilities are in principle always available within the traditionally employed static methods,^[222] as time is the main free parameter in the employed differential Poisson and continuity equations. However, correctly describing the time dependence of displacement currents occurring on both nano- and mega-second timescales requires extreme caution. Even though in principle the same continuity equations apply to all mobile charge carriers, there are two major identifiable differences between electronic and ionic charges. First, a diffusion constant differing by several orders of magnitudes and second, the boundary condition that ionized atoms cannot escape the device, which instead causes their charges to accumulate at the electrode interface. These effects render very large gradients in charge densities and therefore often amount to severe problems in precise numerical calculations. The resulting

numerical inaccuracies thus often prevent stable solutions, especially when integration over long time scales is needed, rendering the transient calculations less straightforward. Due to the omnipresence of mobile ions, the perovskite film must however be treated as a mixed ionic-electronic conductor in any device simulation, where these problems must be dealt with. A few very recent works^[125,135,136,178,179,223–225] nonetheless successfully implemented transient drift-diffusion simulations on perovskite devices and accounted for both free carrier and ion displacements. In this work, a homemade transient drift-diffusion simulator is employed,^[184] written in Julia,^[226] to show how transient OCVD measurements can effectively be used to simultaneously probe both carrier and ion dynamics in working perovskite solar cells. Here it is demonstrated that by including mobile ions and surface recombination, it is possible to quantitatively describe the experimentally measured OCVD transients using drift-diffusion simulations. Further it is calculated how both charges and ions redistribute in time after light is switched off, at various starting intensities and temperatures. With additional knowledge about the steady-state recombination current at each voltage value, a straightforward route to determine the time evolution of device capacitance is provided. By these means it is shown how the concentration of ions, their diffusion coefficient and associated activation energies can be easily determined from the experimental OCVD when the dark current density-voltage $j_d(V)$ or the j_{SC} vs. V_{OC} relation $j_{SC}(V_{OC})$ is known.

6.2 Simulation Conditions

The numerical scheme used is strongly inspired by Nicola Courtier's work, which nicely avoids the above-mentioned numerical problems by an appropriate non-dimensionalization, together with a dispersed finite element based approach.^[136,179] As detailed further in section 4.4.2, the main difference in the implementation in this work is found in the automatic differentiation and the numerical solver applied. The physical model is kept almost identical to what was used by Courtier. However her treatment is marginally expanded by employing the effective mass concept to account for the weak temperature dependence of the density of states. A planar MAPbI₃ device, manufactured by co-evaporation^[152] (See section 4.2), having the photoactive perovskite layer sandwiched between two organic charge selective layers, is chosen for this combined transient experimental/simulation study. Prior to presenting the results of such a device, the chosen con-

ditions of the employed simulations will be clarified. The device is modelled by assuming the perovskite layer to be intrinsic and embedded between doped ETM/HTM layers that are only conductive for electrons/holes. The charge transfer from ETM (HTM) to the intrinsic layer is modelled by thermionic emission over an ΔE_E (ΔE_H) with both sides of an interface in detailed balance, thus defining the ratio of the charge carrier densities on the two sides of an interface. Light absorption and carrier generation is then assumed to follow a Lambert-Beer approximation, thus not accounting for possible interference effects. This may limit the general applicability of the model for thin devices with very high recombination rates, but are amply suited for studies of thick perovskite devices. The various types of allowed recombination routes and their relations to each other must also be fairly justified. It has to be recognized that in current perovskite literature, a large range of assumed recombination routes is proposed to dominate the kinetics. Thus it is first acknowledged that it is not straightforward, with sufficient conviction, to pick the most trustworthy proposed routes and parameters in the simulations. For example, even the mere value of the best-understood rate constant, the radiative rate constant k_{rad} , is still varying quite a lot in literature.^[227] Likewise, both short SRH lifetimes and large surface recombination velocities are currently both proposed to entail the most prominent loss mechanism in perovskite solar cells. For sake of completeness, it has to be chosen to allow for all these types of probable recombination pathways in the model, and their respective rates have to be adjusted to reconstruct both transient and steady-state experiments, performed over a large range of light intensities as well as temperatures. Meaningful modelling of electrical transients benefits enormously from accurate information of physically relevant initial-, as well as steady-state conditions. Some of these can be attained from standard experimental measurements combined with steady-state calculations. Well known boundary conditions embody, for example, the steady-state V_{OC} , which also represents the starting condition for any transient OCVD measurement/simulation. A further useful parameter, embodying a clear premise that also must be satisfied in both transient and steady-state simulations, is the device radiative efficiency.^[228] This ratio, between the radiative rate and the sum of all present rates, accordingly limits the parameter space somewhat. Having measured the external radiative efficiency of the studied device, which amounted to $\sim 2\%$ at current injection conditions similar to $j_{SC}(1\text{ Sun})$, it is ascertained that the ratio of radiative recombination amounts to an identical value at carrier concentrations under 1 Sun steady-state illumination conditions also in the simulated solar cell. Employing the external radiative rate constant k_{rad}^{ext} as determined by Staub et al.,^[85] and reliable mobility values as provided by Zhai^[229] as

further material input parameter, a good starting condition for the total simulation of free charge carrier kinetics is provided. As for the mobile ions additionally present in perovskite materials, it is also needed to justify the chosen simulation inputs. A now fairly accepted mechanism of ionic migration in metal halide perovskite seems to be vacancy mediated iodine migration as outlined in section 2.1.2. Therefore, in the model it is selected to simulate the migration of the virtual positively charged vacancies only, and assumed an evenly distributed and stationary negative countercharge to maintain global ionic charge neutrality corresponding to an intrinsic perovskite layer. Due to their positive charge, the mobile vacancies are subject to the same field induced drift as the holes, whereby the electrostatic field is mostly caused by the positive/negative space charge in the ETM/HTM. It is then assumed that these vacancies, unlike the electrons/holes, are not transported through the ETM/HTM. Consequently, due the direction of the built-in field, the positively charged vacancies are accumulated at the perovskite/HTM interface when the device is in darkness under equilibrium conditions. The full set of chosen simulation parameters, shown in Table 6.1, is accordingly the one best able to reconstruct not only a 300 K illuminated j - V curves on linear scales (Fig. 6.1a), but more importantly also the quasi steady-state j_d curves as well as the $j_{SC}(V_{OC})$ relations on logarithmic scales for several temperatures, as shown in Figure 6.1b. Since doping concentrations and surface recombination velocities are determined by the way the cell is manufactured, these device specific parameters cannot be obtained from literature and were instead determined by global fitting of the simulated to the experimental transient and steady-state data, at all investigated temperatures, and marked with “*” in Table 6.1. It is emphasized that it is herein aimed for the quite ambitious target to obtain one closed description of all experimental data from different experiments (steady-state and transient) at several temperatures and light-intensities, which cannot be found in the literature up until now.

6.3 Open Circuit Voltage Dynamics

The main outcome of this work is however to be found in the measured and simulated transients. In Figure 6.2a, the measured OCVD data is compared with the results from the transient simulations using the input parameters from Table 6.1, once with (yellow) and once without (blue) mobile ions present. Several aspects of the complete decay

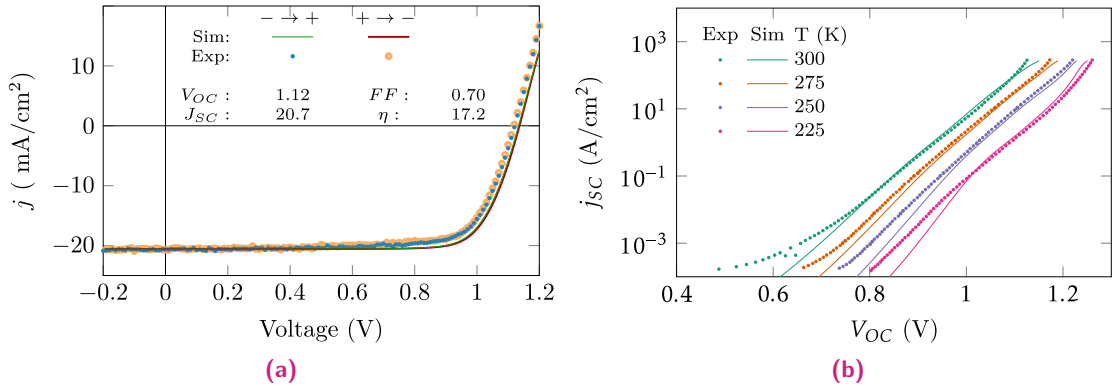


Figure 6.1.: (a) Measured and simulated j - V at 1 Sun light exposure, showing a complete absence of hysteresis at a 200 mV s^{-1} scan rate in forward (green) and backward (red) direction. A series resistance of $200 \Omega \text{ mm}^2$ was assumed in the simulations. (b) Comparison of the measured and simulated steady-state $j_{SC}(V_{OC})$ relations.

deserve detailed attention. First, the early OCVD drop observed at around 10 ms (blue arrow) is attributed mostly to free carrier kinetics and to the fact that the built-in potential V_{BI} of the simulated device is noticeably lower than the V_{OC} measured at 1 Sun illumination intensity (the device V_{BI} of 987 mV is a direct outcome of the chosen input HTM/ETM parameters). Under such strong (1 Sun) illumination, the excess free electron (hole) density near the HTM (ETM) is quite prominent. This is highlighted in Figure 6.3a and b where the excess charge densities (deviation from the steady-state equilibrium density in the dark) of electrons and holes are shown. At the initial times (blue line), a clear increase of excess hole (electron) densities is found near the electron (hole) transport layer interfaces. The reason here fore is found in that the V_{OC} has overcome the V_{BI} , resulting in an inverted internal field causing holes (electrons) to accumulate at the ETM (HTM) and appears irrespective of the presence of mobile ions.

The distribution of excess carriers also rationalizes why surface recombination is more dominant at these earlier times as it implies that a more pronounced amount of minority excess carriers is found in a region of the device where the counterpart majority charge is usually residing (e.g. rendering more holes closer to the ETM). This can be compared to the more progressed decay, where the excess free carriers now have to diffuse through the bulk of the device to recombine with a counter charge located closer to the opposing interface. Surface recombination, being responsible for the fast initial drop, present also in the simulated ion free device, thus certainly limits the achievable

Table 6.1.: Parameters used for the drift-diffusion simulations in this chapter if not specified differently. Values marked with “*” were obtained by global fit.

Symbol	Discription	Value	Ref.
T	Temperature	300 K	-
F_{ph}^0	Absorbed photon flux (AM1.5)e	$1.4 \times 10^{21} \text{ m}^{-2} \text{ s}^{-1}$	-
α	Perovskite absorption coefficient	$1.3 \times 10^7 \text{ m}^{-1}$	[230]
ε_p	Perovskite relative permittivity	22	[51,231]
$\varepsilon_E/\varepsilon_H$	ETM/HTM relative permittivity	3	-
d	Perovskite layer thickness	500 nm	-
d_E/d_H	ETM/HTM thickness	50 nm	-
n_E	ETM doping concentration	$1 \times 10^{17} \text{ cm}^{-3}$	*
p_H	HTM doping concentration	$1 \times 10^{16} \text{ cm}^{-3}$	*
m_E/m_H	ETM/HTM electron/hole effective mass	$3/12 m_e$	*
m_n/m_p	Perovskite electron/hole effective mass	$0.2 m_e$	[85]
N_{ion}	Mean mobile ion concentration	$1.4 \times 10^{16} \text{ cm}^{-3}$	*
E_g	Perovskite band gap energy	1.6 eV	[42,83,84]
ΔE_H	HTM-perovskite valence band offset	0.14 eV	*
ΔE_E	Perovskite band gap energy	-0.2 eV	[152]
D_{ion}	Iodine vacancy diffusion coefficient	$3.3 \times 10^{-13} \text{ m}^2 \text{ s}^{-1}$	*
D_n	Perovskite electron diffusion coefficient	$5.5 \times 10^{-6} \text{ m}^2 \text{ s}^{-1}$	[229]
D_p	Perovskite hole diffusion coefficient	$6.3 \times 10^{-5} \text{ m}^2 \text{ s}^{-1}$	[229]
D_E/D_H	ETM/HTM electron/hole diffusion coefficient	$10 \times 10^{-8} \text{ m}^2 \text{ s}^{-1}$	-
τ_n/τ_p	Bulk SRH electron/hole lifetime	800 ns	[232]
k_{rad}^{ext}	Bulk radiative recombination const. (external)	$4.78 \times 10^{-11} \text{ cm}^3 \text{ s}^{-1}$	[85]
ν_{nE}	ETM interface electron recombination velocity	$8 \times 10^{-6} \text{ m s}^{-1}$	*
ν_{pE}	ETM interface hole recombination velocity	0.6 m s^{-1}	*
ν_{nH}	HTM interface electron recombination velocity	$2.5 \times 10^{-3} \text{ m s}^{-1}$	*
ν_{pH}	HTM interface hole recombination velocity	0.75 m s^{-1}	*

steady-state (and starting) V_{OC} of the measured and simulated device, in line with observations by Stolterfoht et al.^[109,233] The V_{BI} of 987 mV accordingly can be declared as a high voltage restraint although the actual value of the V_{BI} can, and certainly is, overcome by the open circuit voltage in the investigated device. This underscores that although a high V_{BI} does not increase separation and extraction of carriers,^[234] it definitely helps to reduce the influence of surface recombination in operational solar cells under high illumination. It is however worth noting here, that when surface recombination is accounted for in the model, the outcome of the simulation on timescales shorter than 1 ms are highly sensitive to many of the initially selected device input parameters. Since the model used depends on the carrier concentration in the respective transport

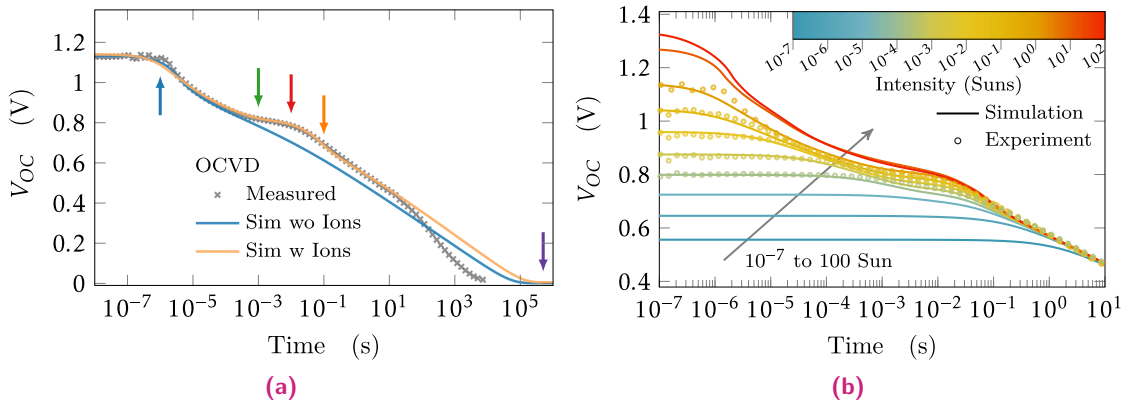


Figure 6.2.: (a) Comparison of measured (crosses) and simulated (solid lines) OCVD for a perovskite n-i-p solar cell with and without the presence of mobile ions. The characteristic shoulder related to the presence of mobile ions is located in the time window between 1 to 100 ms. Except for the shunt regime (very long times), every part of the decay (with ions) is reproduced quantitatively. The colored arrows indicate the points in time used to visualize the instantaneous charge distributions presented in Figure 6.3. (b) Comparison of the simulated and measured OCVD with varying starting illumination intensities ranging from 10^{-7} to 100 Sun. The ionic shoulder becomes increasingly visible with higher light intensities, for both the simulated as well as the measured data.

layer and the adjacent perovskite on both sides of the device, the assumed values for the surface recombination velocity need to be altered with either the energetic offsets or the effective doping in the transport layers. In addition, the chosen value of mobility also starts to play a more prominent role here. This originates from the fact that a higher mobility allows to feed the local surface recombination more effectively with new free carriers.^[85] These circumstances unfortunately restrict this study to make only qualitative statements about the early voltage decay, identifying it as surface recombination, but prevents a quantitative assignment of e.g. the actual surface recombination velocities.

Second, at later times of the decay something distinctly different is however happening in the ionic device. Recently it has been shown that the later parts of OCVD is generally determined by the recombination of capacitive stored charges^[212] in both silicon pn-junctions as well as in thin organic devices, consistent with that the two charge carriers types being located separately in their respective transport layers near the electrodes, as show in Figure 6.3a and b. A full OCVD can thus easily take several hours in normal, (un-shunted) ion-free solar cells, as these separate distributions needs to diffuse towards each other prior to recombining.^[235] On such long timescales, the possible ef-

fect of ionic redistribution (if also present), should however have a direct impact on the shape of the observed voltage transients. Importantly for this work, the so-called voltage persistency previously observed in perovskites^[198,207,214] is again clearly identified also in this device at around 10 ms in Figure 6.2a and can in fact be fully explained by the ionic redistribution. Here it is emphasized that the OCVD shoulder of the ion containing device is clearly distinguishable from the rest of the voltage decay. Figure 6.3c shows the time evolution of the simulated ion concentration at the selected points in time, as highlighted in the OCVD of Figure 6.2a. The correlation between the most pronounced ionic displacements and the persistency feature (shoulder) seen in the OCVD is evident. Under steady-state 1 Sun illumination conditions, (starting conditions for the OCVD) a significant amount of the positively charged iodide vacancies have accumulated closer to the ETL. This has occurred, as under strong illumination V_{OC} exceeds the built in voltage and the electrostatic potential gradient points towards the ETM and drives the positive vacancies there. As the light is switched off, they start to redistribute back to their dark equilibrium positions. Initially (green arrow and line), during the first millisecond of the OCVD, there are just slight alterations of the ionic density distribution. After this point a noticeable shoulder in the voltage transient develops, which exactly matches the time when the ionic species start to accumulate more on the opposing interface (red arrow/line in Fig.6.2a/6.3c). After 100 ms this process is essentially complete (orange arrow and line) which accordingly corresponds to the time of almost all ions are back in their thermal equilibrium positions.

The externally measurable voltage corresponds to the difference in the quasi Fermi level (QFL) at the respective electrodes. The QFL expresses the electro-chemical potential representing the sum of the chemical and the electrostatic potential at each position in the device. While the chemical potential at every point in the device is determined by the charge carrier density prevailing there, the electrostatic potential is defined by the Poisson equation and thus by the net charge distribution present over the whole device. The net excess charge distribution is defined as the sum of the individual electron, hole and ionic excess charge distributions and is shown in Figure 6.4. Figure 6.3a and b show already that the charge concentration at the outer electrodes (and thus the chemical potential) is virtually constant during the entire OCVD, which tells us, that during the time where the shoulder in V_{OC} is observed the electrostatic potential however has to be constant at the electrodes as well. This can be explained by an almost unchanged net charge distribution in the time window of the shoulder. Although recombination

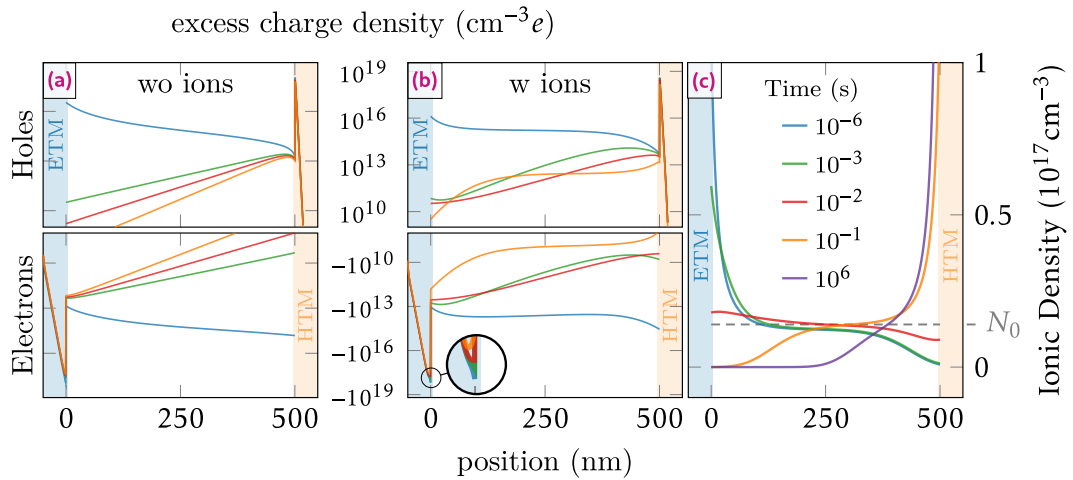


Figure 6.3.: (a) Excess charge density of free electrons and holes during the OCVD inside the (a) ion-free device and (b) the device with mobile positive iodide vacancies, whose distribution is shown in (c). It is chosen to represent excess hole and electron densities as positive and negative numbers respectively, on logarithmic scales away from a virtual “zero” level, corresponding to the dark conditions without any excess carriers. The motif for this somewhat unconventional representation is merely to increase clarity in the graph. The positive iodine vacancy distribution is shown on a linear scale, where the dashed grey line corresponds to a homogeneous effective average density of $1.4 \times 10^{16} \text{ cm}^{-3}$ and furthermore equating the stationary negative counter-ion distribution. The inset in (b) shows the zoomed decaying excess electron distribution inside the ETM (where it has to be noted that the substantially larger magnitude of excess charge herein originates from the much lower dark carrier concentration due to depletion upon Fermi level equilibration when forming the device).

still takes place here, the resulting change in the distribution of the free electrons and holes is largely compensated by the displacement of the ions. A closer look on the ETM side of the ETM/perovskite interface in Figure 6.3b reveals that the electron density is indeed decreasing during the entire time window. However, this local reduction of negative free electron charge is accompanied by a decrease of the positively charged ionic vacancies accumulated on the perovskite side of the ETM/perovskite interface, as shown in Figure 6.3c. This effectively keeps the net charge density distribution around the ETM/perovskite interface almost unchanged in the time window between 1 and 10 ms, resulting in an almost constant electrostatic potential and thus an almost constant V_{OC} at the electrodes, when mobile ions are present. At the final point of the decay, when the simulated voltage reaches 0 V at 106 seconds (or 278 hours) the device is fully back to dark equilibrium conditions, where all excess charges are gone and the mobile ions

are again located close to the HTM. It has to be noted that after ~ 10 s the experimental voltage decays faster than the simulations. This is merely caused by shunt and leakage currents,^[235] not included in the simulations. A simple ohmic shunt could be added to the modeling, as sometimes done by other researchers implementing drift-diffusion simulations. It would however not add anything in terms of understanding the free carrier and ionic kinetics. The esthetics of the fits would possibly increase, but that is it. As it has also been observed that shunts are not always best described as truly ohmic, it is preferred to abstain modeling this part and focus instead on the main topic of ion migration. This not truly ohmic behavior would also enormously complicate the fitting process since the simulations would never be able to reconstruct this part of the OCVD correctly when only ohmic shunt is assumed. As a result the fitting algorithm would likely propagate the errors originating from this inaccuracy to the other parameters. Thus in favor of correctness to leave this part is left out for now. An essential aspect of the observed persistent

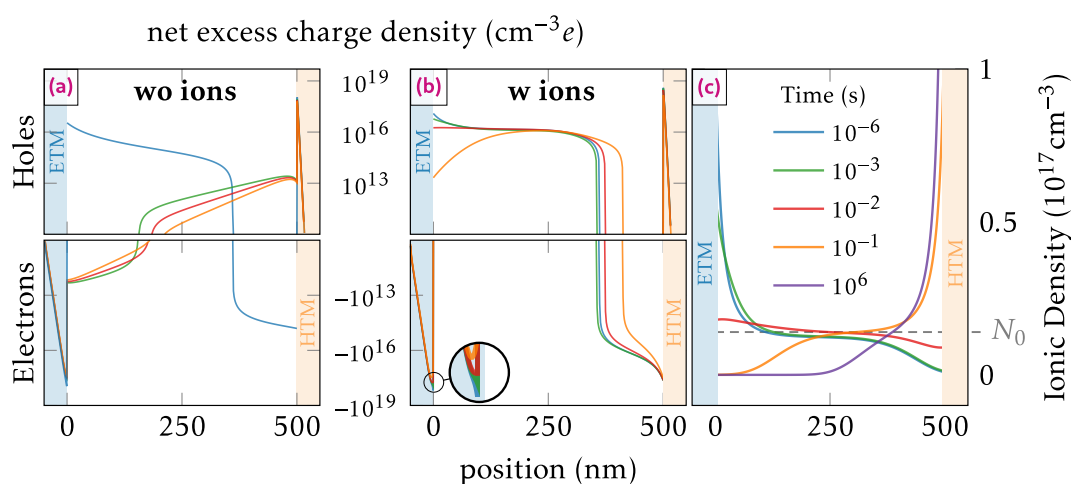


Figure 6.4.: Evolution of the net excess charge density (sum of electron, hole and ion densities) during the simulated OCVD decay. (a) Without mobile ions the charge density close to the ETM rises monotonically. (b) Including mobile ions, where the increase of the net charge density left of the ETM/Perovskite interface is compensated by a decrease of the net charge density on the right of the ETM/Perovskite Interface, leading to an almost constant V_{OC} . (c) The ionic density distribution.

photo voltage is that it is strongly dependent on the initially set illumination intensity. As can be seen in Figure 6.2b, the experimental data can be reproduced directly and accurately in the simulations without changing any of the other model input parameters. First it is confirmed that at low illumination intensities, the initial fast decay (previously

shown in Fig. 6.2a at ~ 10 ms) is no longer present. Under such conditions, the spatial distribution of photo-generated charge carriers never allows for any pronounced surface recombination, as an insignificant amount of electrons is positioned near the HTL and likewise for holes at the ETL. Secondly, we see that the ionic contribution to the OCVD gets less pronounced when the light intensity is reduced, and completely vanishes when the illumination intensity is below 10^{-4} Sun. This shows that any proposed light soaking or light induced degradation^[236,237] do not seem to play any significant role here, but instead that the ionic polarization alone is fully sufficient to explain the transient behavior (at least for this studied and simulated device). The fact that the ionic contribution to the OCVD becomes more pronounced with increasing initial starting illumination, and hence V_{OC} , is only due to that more ions are initially accumulated next to the ETM. Finally, it has to be noted that there also appears to be a saturation of the ionic feature for the strongest measured/simulated illumination. This can probably be rationalized by the fact that the amount of available mobile ions is indeed finite and thus above a certain value of V_{OC} all the ions are completely accumulated next to the ETM, such that a further increase of illumination intensity (and thus voltage) will have almost no additional effect on the ionic distribution. Again, we stress that only one set of ionic input parameters can reconstruct the measured persistent ionic OCVD shoulder at every simulated initial light intensity.

6.3.1 Ionic concentration measurement

Now, the device capacitance $C(V) = dQ/dV$ as an external measurable device property will be given special attention, as it directly relates a change in the externally measured V_{OC} to changes in the total number of charge Q stored inside the device. Capacitance is commonly determined by frequency-dependent impedance measurements, but in principle, other methods that are more direct are also available. Here a simple (but novel) method is we proposed for determining the differential capacitance, which can be calculated directly from the inverse time derivative of the OCVD transient, combined with the commonly measured device recombination current- voltage characteristics $j_d(V)$:

$$C(V(t)) = \frac{dQ}{dV} = \frac{dQ}{dt} \frac{dt}{dV} \approx j_{sc}(V_{OC}(t)) \left(\frac{dV_{OC}(t)}{dt} \right)^{-1}. \quad (6.1)$$

To avoid the influence of series resistance, omnipresent in traditional dark $j_d(V)$ curves at high voltages, instead of the dark $j_d(V)$, the $j_{SC}(V_{OC})$ steady-state relation^[228] is employed here, as the best representative for the time derivative of charge. This replacement can be done, as at each steady-state open circuit voltage value, the sought-after recombination current must be equal to the generation current, which in most solar cells is very well approximated with the j_{SC} . An assumption of this approach is thus that the steady-state recombination current, corresponding to a particular steady-state V_{OC} value, is indeed the same as the recombination current at the same instantaneous V_{OC} value during the decay. Prior to the implementation of Equation 6.1, a fair amount of logarithmic data interpolation needs to be executed, as the experimental amount of OCVD data from oscilloscope sampling is a lot larger than the 80 data points of the $j_{SC}(V_{OC})$ relation (Fig. 6.1b). Unlike impedance spectroscopy or cyclic voltammetry, this method does not employ frequency modulation, but determines instead directly the voltage and time-domain capacitance $C(V_{OC}(t))$ continuously and always at true open-circuit conditions. This is not the case with traditional frequency impedance measurements, where the required small AC modulation is always bringing the potential slightly above and below the true, and sought-after, V_{OC} condition. This accordingly has the enormous analytical advantage that the data can easily be interpreted directly following Equation 6.1 without having to assume any specific equivalent circuit model. As with impedance measurements, interpretational concerns will however arise if the device shows pronounced j - V hysteresis. Especially in the case of only moderately or poorly performing perovskite solar cells, a hysteresis is often observed in such a way that they differ depending on the direction in which the voltage is swept through. In the presented method for the determination of ionic characteristics, j - V hysteresis is a challenge, since the total recombination rate in such a case is obviously also influenced by the internal ionic distribution. As a result, the recombination current obtained by j - V measurement is not exactly the same as during OCVD. However, Equation 6.1 shows that an error in the recombination current only contributes linearly to the determination of the capacitance, and thus has only a linear effect on the determination of the ion density. Therefore, if there is a low percentage of uncertainty in the recombination current due to hysteresis, this does not play a significant role for most practical concerns. However, if the solar cell is excessively affected by hysteresis, it is advisable to use a variable scan rate instead of a fixed one. Ideally, the voltage during measurement would be run through at the same rate as it falls in the OCVD, so that an $j(V_{OC}(t))$ curve is obtained

where the $V_{OC}(t)$ corresponds to the OCVD decay. As it is visible in Figure 6.1a the here studied device did not suffer from hysteresis limitations and thus can be examined safely.

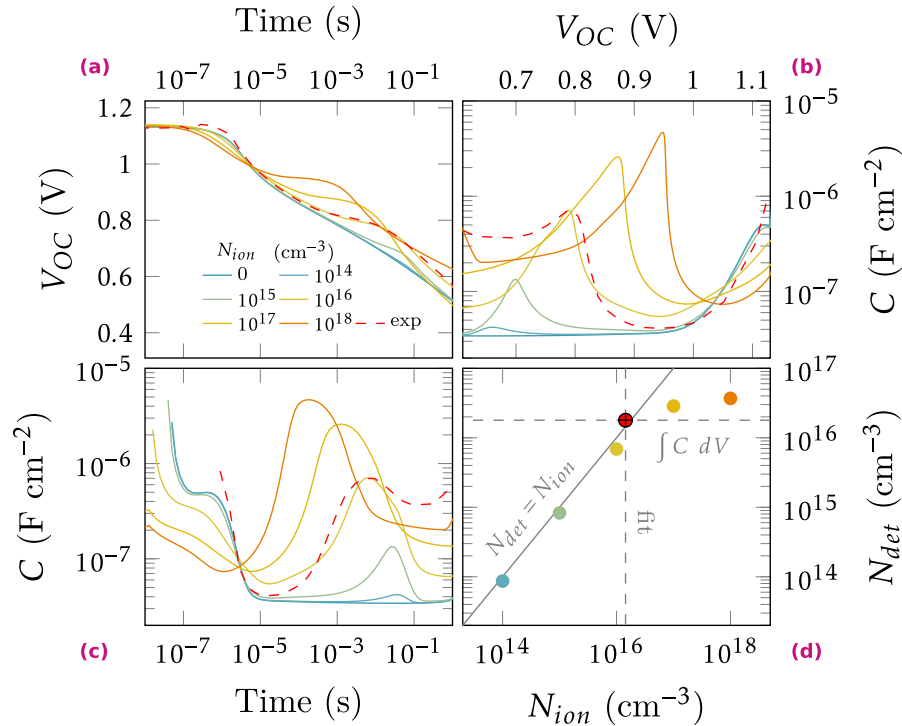


Figure 6.5.: (a) Simulated OCVD for six different ionic concentrations together with the experimentally obtained (red dashed) transient, (b) corresponding deduced transient capacitance, (c) capacitance-voltage plots according to eqn (1), where the peak area corresponds to the ionic charge density, (d) calculated (determined) ionic densities N_{det} resulting from $C(V)$ integration compared to input values N_{ion} in the simulations. Almost no deviations are observed for input values of $N_{ion} < 10^{17} \text{ cm}^{-3}$. The red dot shows the experimentally determined ionic density together with the value obtained from fitting the model to the experimental data.

The results of the analysis according to this method are summarized in Figure 6.5. First, a set of simulated OCVD signals for six different input ion concentrations is displayed in Figure 6.5a. Applying Equation 6.1 to this simulated decay shows that at the time of the shoulder in the OCVD, a very distinct peak in the capacitance occurs, as displayed in Figure 6.5b. This describes the aspect that despite recombination taking place, the voltage here changes only marginally, which is due to the ionic motion that compensates the charge carrier decrease in the transport layers, in a way that the net charge density remains almost constant, as described earlier. Finally, Figure 6.5c displays the corresponding capacitance values in Figure 6.5b vs. the voltage from Figure 6.5a, at

the respective times. Based on the knowledge obtained from the simulations it is now possible to provide an approximate experimental method allowing the determination of the mobile ion concentration and diffusivity from the measured OCVD signal, without actually having to employ and rely on specific drift-diffusion simulations. Therefore it is best to start by assuming that all ions were indeed accumulated at one of the interfaces at the beginning of the OCVD measurement and they all moved to the other interface at the end, the amount of charge displaced per area can be associated by evaluating the classical charge integral $Q[\text{F cm}^{-2}] = \int C(V) dV$. This general integral only provides a value. It does not provide information on what type of charge is moved, nor where the charge carriers are located inside the device. Only thanks to the simulations it is in fact known that the main peak in Figure 6.5b and c is indeed originating almost exclusively from ionic displacement, and it is also known how their distribution altered in time from Figure 6.3c. However, even if one can be certain that the main capacitive peak is indeed of ionic origin, a small capacitive contribution arises also from the amount of free charges still residing on the electrodes. Since the free charge carriers stored in the transport layers are also included in the total charge integral, it is in principle suited to also subtract them (especially if the device has a very low amount of mobile ions). This small geometric capacitance charge can be read off easily as the constant plateau for the lower simulated concentrations in Figure 6.5c. Bearing the logarithmic scale in mind, here it can be however sanction the experimentalist, not having access to the small value of the simulated plateau, to simply neglect it, and associate the integrated peak entirely with the value of mobile ion concentration. A clarification on the concept and utilization of the term “concentration” is however in place here, as it is important to understand, that both ions and free charges are almost always distributed inhomogeneously inside the film. Just dividing the ionic charge per area, as obtained from the integral, with the thickness of the film thus only allows determining a mean charge concentration $N_{ion} = Q/d$. The obtained value is accordingly only truly correct for the red line in Figure 6.3c, at the time where the ions are indeed distributed sufficiently homogeneous. It does however not diminish the importance of the average ion concentration as a key parameter when comparing differently manufactured devices or films.

In Figure 6.3d we plot the derived values of ionic concentration vs. the input simulated ones, together with the value obtained from the real measured cell. The average ion concentration for the studied device amounts to $N_{ion} = 1.4 \times 10^{16} \text{ cm}^{-3}$ and is in perfect agreement with the findings in chapter 5. This value can be compared to the higher val-

ues ($4 \times 10^{17} \text{ cm}^{-3}$) found by Bertoluzzi et al.^[219] and the lower values ($1 \times 10^{15} \text{ cm}^{-3}$) observed^[238–240]. The apparent large deviation in the reported values are partly caused by the different sample preparation techniques, certainly leading to different Im properties. However, some of the prior employed methods to determine the ionic density depend on assumptions that may not be sufficiently fulfilled. In case of the transient ion drift method^[239] a background doping concentration which is both uniform and much higher than the ionic concentration is required,^[241] which essentially restricts its application only to highly doped pn-junctions. The method proposed in^[219] further depends on accurate estimates of the built-in potential which is difficult to measure accurately in n-i-p/p-i-n structures, and certainly cumbersome to obtain in devices with mobile ions, as it has been show in chapter 5. The method, based on integrating $C(V_{OC})$ directly without charge profile simulations, however also has to be treated with some caution as it provides the amount of accumulated ionic charge that is not necessarily equal to the total ionic charge present in the device. At high ionic concentrations, a part of the ionic charge is already capable to completely shield the electric field from the bulk and the remaining ions can freely diffuse within the perovskite layer where they do no longer contribute to the $C(V_{OC})$ integral. In those cases, the more accurate treatment based fully on the exact knowledge of ion distribution has to be used, as previously also demonstrated by Bertoluzzi et al.^[219] With the chosen parameters, noticeable deviations between the input ion concentration and the concentration determined by the direct integral method indeed occurs at $N_{ion} > 10^{17} \text{ cm}^{-3}$, as seen in Figure 6.5d

6.3.2 Diffusivity measurement

With the mean ion concentration reliably determined with this approach, it is now further possible to also determine the ionic diffusivity (or diffusion coefficient D_{ion}). This parameter embodies the defining characteristic of ionic conductors and is essential to identify in perovskite optoelectronic materials as it partly governs the magnitude of j - V hysteresis in devices.

Ionic diffusivity is a thermally activated parameter with an activation energy E_{ion}^D according to Equation 2.4. Following ref. [136,179,242,243], the characteristic time constant

τ_{ion} of the ionic relaxation is related to the ionic diffusion coefficient and the mean ionic concentration according to

$$D_{ion} = \frac{d}{\tau_{ion}} \sqrt{\frac{\varepsilon_p \varepsilon_0 k_B T}{N_{ion} q^2}} \quad (6.2)$$

This expression relates the diffusing distance d to the effective diffusive time constant and accordingly assumes that the ions in the device are only subjected to diffusive motion. A heuristic derivation of Equation 6.2 can be done by considering τ_{ion} as the time an ion with velocity ν_{ion} needs to overcome the distance $d = \nu_{ion} \tau_{ion}$. By equating the diffusion current with Ohm's law ν_{ion} can be expressed in form of a ordinary differential equation

$$j_{ion} = -q D_{ion} \frac{dN_{ion}(x)}{dx} = q N_{ion} \nu_{ion}. \quad (6.3)$$

By the reasonable approximation the ions form a electrostatic double layer at a transport material-perovskite interface (in literature often referred as *Debye layer*) with a exponential shape in the form of

$$N_{ion}(x) \approx N_{ion}(x=0) \cdot e^{-x/\lambda_D} \quad (6.4) \quad \text{with} \quad \lambda_D = \sqrt{\frac{\varepsilon_p \varepsilon_0 k_B T}{N_{ion} q^2}}, \quad (6.5)$$

Equation 6.3 can be solved for $\nu_{ion} = D_{ion}/\lambda_D$, where the term λ_D is the Debye length. Finally, the expression

$$d = \nu_{ion} \tau_{ion} = \frac{D_{ion}}{\lambda_D} \tau_{ion} \quad (6.6)$$

can be rearranged to Equation 6.2.

It is important to note that this expression differs from that recently used^[239] in transient ion drift analysis on pn-junctions, where a central analytical criterion requires the ion concentration to be significantly lower than the doping concentration in the active layer.^[241] This renders the proposed method superior for p-i-n or n-i-p-hetero-structures, as it applies for intrinsic materials and does furthermore not depend on accurate determination of the built-in potential.

Figure 6.6 shows the effect of different input diffusion coefficients on the simulated OCVD and the corresponding capacitance derived via Equation 6.1, again compared to the experimentally determined (red dashed) curves. A direct proportional shift of the

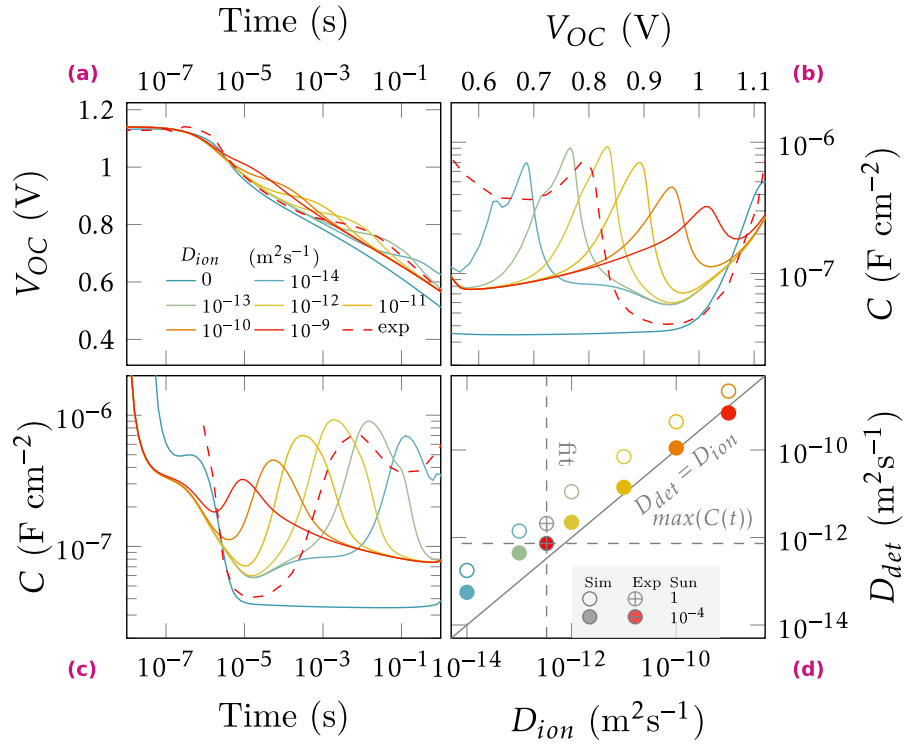


Figure 6.6.: (a) OCVD simulated with different input ionic diffusion coefficients together with the experimentally obtained curve at 1 Sun initial perturbation, (b) time resolved capacitance showing the corresponding proportional peak shift, (c) obtained $C(V_{OC})$ where the integrated peak area stays constant, and equates to the (defined) density of mobile ions, (d) diffusion coefficients D_{det} determined with high (1 Sun) and low (10^{-4} Sun) initial perturbation vs. diffusion coefficient D_{ion} used as simulation input.

temporal $C(t)$ peak position, representing the characteristic ionic time constant τ_{ion} , is observed in Figure 6.6b, as lower input diffusivity shifts the OCVD ionic shoulder to longer times. The observed shift from the simulations thus clearly highlights the range and ability of the OCVD method to target device ionic kinetics. The area under the $C(V)$ curves in Figure 6.6c corresponds to the total amount of (simulated input) ionic charge and does therefore not change. By employing the film thickness as effective diffusion distance and the peak positions in Figure 6.6b, as the characteristic time constant we can via Equation 6.2 estimate the diffusivity (diffusion coefficient D_{det}). However, the ions are not exclusively subjected to diffusion, but partly also to a possible drift as mentioned earlier, implying that strong perturbation from the dark equilibrium should be avoided when applying Equation 6.2, which assumes only ionic diffusive motion within a Debye layer. For a more precise determination of the ion diffusivity, it is therefore

generally advisable to measure the OCVD also at lower initial illumination intensities, where the lower induced voltage provides smaller contribution to ionic drift, like shown in Figure 6.6d. The proportionality of D_{det} to the simulation input coefficient D_{ion} is nevertheless maintained even under large perturbation conditions as visible in Figure 6.6d. This figure thus validates the employment of Equation 6.2 and provides a straightforward route for the determination of ion diffusivity in complete devices from OCVD measurements. Importantly for the accuracy of the method, Equation 6.2 has a sublinear dependence on the determined mean ionic concentration, making D_{det} quite tolerant against errors in the determined N_{ion} . In perovskite literature up until now, the determined ionic activation energy has been assigned mostly for ionic conductivity, merely defined by the product of the number of mobile ions and their diffusivity. Accordingly, no differentiated clear information regarding whether the conductivity is thermally activated due to an increased (thermally released) number of ions or to a thermally activated mobility/diffusivity has been offered. This is mainly due to the fact that the decoupling of the ionic conductivity in diffusivity and density is hardly feasible with established methods, but is of course imperative for a general understanding of ion kinetics in perovskite semiconductors.

6.4 Experimental factorization of the ionic conductivity

Thus, to change the only attainable experimental variable that can influence the ion motion in the same device device, OCVD is carried out at a series of reduced temperatures. as shown in Figure 6.7. Panel (a) shows the measured and simulated OCVD curves, clearly allowing the identification of a delayed ionic shoulder upon cooling. From panel (b) it is thus also evident that the derived $C(t)$ maxima are markedly shifted to later times as the temperature is reduced from 300 K down to 225 K while in the $C(V)$ representation, shown in panel (c), only minor changes are visible. Figure 6.7 thus contrast the simulations in Figure 6.6, where temperature was kept constant and only the material ion diffusivity was altered. In the temperature dependent measurements, not only ion diffusivity decreases with T , but also the intrinsic carrier concentration n_i , as well as the thermionic emission rates at the electrodes. This accordingly reduces the dark saturation current value j_0 , which delays the overall OCVD in a similar temperature dependent manner as the ion motion, such that the $C(V)$ peak position now remains at

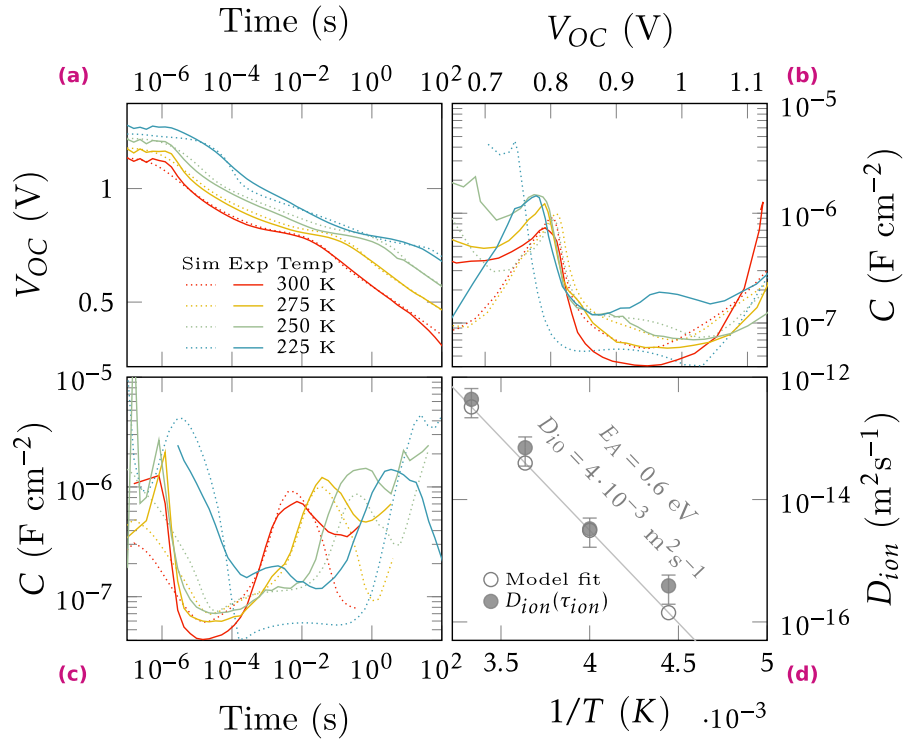


Figure 6.7.: (a) Experimental OCVD measured (solid) at four different temperatures compared to the simulated decay (dotted), (b) Derived time resolved capacitance showing a proportional peak shift. The $C(V_{OC})$ peak position in (c) stays nearly constant, because also recombination is throttled at lower temperature, (d) Arrhenius-plot allowing the determination of the activation energy of the measured (closed circles) and simulated (open circles) ionic diffusivity.

around the same voltage value. Importantly, the peak area does not alter much and the amount of mobile ions does therefore not change strongly with T , at least in this studied temperature range (and device), meaning that there is no specific need to invoke a temperature activated release (exponential with $1/T$) of the number of mobile ions. Instead, the diffusivity of the ions is fully governing the $C(t)$ data of Figure 6.7b and is obviously strongly temperature activated. This allows us to conclude that (in this studied device and temperature range) the thermally activated ion conductance has its principal origin in the thermally activated diffusivity. The value of the activation energy for the diffusivity can therefore be derived from an Arrhenius plot of τ_{ion} ($1/T$) as shown in Figure 6.7c. With the now rational postulate of an ion concentration remaining essentially constant with temperature, we can determine the diffusivity activation energy $E_{ion}^D = 0.6 eV$ of mobile iodine vacancies (in good agreement with^[62]) and their diffusion constant of

$D_{ion}^0 = 4 \times 10^{-3} \text{ m}^2 \text{ s}^{-1}$, which corresponds to an ion diffusivity at room temperature of $D_{ion} = 3.3 \times 10^{-13} \text{ m}^2 \text{ s}^{-1}$, in excellent agreement with recent literature as well.^[132] In total, it can be clearly stated that it is justified to assign the changed time constant directly to a change in the ionic diffusivity, without having to account for a temperature-induced change in ion concentration. As OCVD measurements are easy to implement experimentally, herein an appealing route to probe ionic motion in complete devices is provided, comprising electronic and ionic conducting materials, such as metal-halide perovskites.

6.5 Conclusions

Herein a transient drift-diffusion solver is developed and implemented on experimentally measured open circuit voltage decay measurements obtained from planar n-i-p perovskite solar cells, and focused the efforts on ionic kinetics. The omnipresent shoulder seen in OCVD from perovskite devices can straightforwardly be assigned uniquely to ionic redistribution. By introducing a simple expression allowing calculating the differential capacitance from the OCVD and a simultaneously measured current-voltage relationship, and by performing intensity and temperature dependent measurements and simulations, a experimental technique is provided enabling the determination of both concentration as well as diffusion coefficients for the slowly moving ionic species in fully operational perovskite solar cells. The T -dependent measurements provide a 0.6 eV activation energy for the diffusivity of the ions and their diffusion constant of $D_{ion}^0 = 4 \times 10^{-3} \text{ m}^2 \text{ s}^{-1}$, with a nearly constant mean concentration of $N_{ion} = 1 \times 10^{-16} \text{ cm}^{-3}$ within the investigated temperature range. A strong benefit of the proposed method is that it does not depend on any prior knowledge of neither V_{BI} nor background carrier-doping concentrations, parameters that are rather difficult to determine for the non-pn-junction device configurations currently dominating the perovskite field.

Summary

7

The fact that photovoltaics is a key technology for climate-neutral energy production can be taken as a given. The question to what extent perovskite will be used for photovoltaic technologies has not yet been fully answered. From a photophysical point of view, however, it has the potential to make a useful contribution to the energy sector. However, it remains to be seen whether perovskite-based modules will be able to compete with established technologies in terms of durability and cost efficiency. The additional aspect of ionic migration poses an additional challenge. In the present work, primarily the interaction between ionic redistribution, capacitive properties and recombination dynamics was investigated. This was done using impedance spectroscopy, OCVD and IV characteristics as well as extensive numerical drift-diffusion simulations. The combination of experimental and numerical methods proved to be very fruitful.

A suitable model for the description of solar cells with respect to mobile ions was introduced in chapter 4.4. The formal mathematical description of the model was transferred by a non-dimensionalization and suitable numerically solvable form. The implementation took place in the Julia language. By intelligent use of structural properties of the sparse systems of equations, automatic differentiation and the use of efficient integration methods, the simulation tool is not only remarkably fast in finding the solution, but also scales quasi-linearly with the grid resolution. The software package was released under an open source license.

In conventional semiconductor diodes, capacitance measurements are often used to determine the space charge density. In the first experimental chapter 5, it is shown that although this is also possible for the ionic migration present in perovskites, it cannot be directly understood as doping related, since the space charge distribution strongly depends on the preconditions and can be manipulated by an externally applied voltage. The exact form of this behavior depends on the perovskite composition. This shows, among other things, that experimental results can only be interpreted within the framework of conventional semiconductors to a very limited extent. Nevertheless, the built-in

potential of the solar cell can be determined if the experiments are carried out properly. A statement concerning the type and charge of the mobile ions is not possible without further effort, while their number can be determined.

The simulations were applied to experimental data in chapter 6. Thus, it could be shown that mobile ions make a significant contribution to the OCVD of perovskite solar cells. j - V characteristics and OCVD transients measured as a function of temperature and illumination intensities could be quantitatively modeled simultaneously using a single global set of parameters. By the simulations it was further possible to derive a simple experimental procedure to determine the concentration and the diffusivity of the mobile ions. The possibility of describing different experiments in a uniform temperature-dependent manner strongly supports the model of mobile ions in perovskites.

In summary, this work has made an important contribution to the elucidation of ionic contributions to the (photo)electrical properties of perovskite solar cells. Established experimental techniques for conventional semiconductors have been reinterpreted with respect to ionic mass transport and new methods have been proposed to draw conclusions on the properties for ionic transport. As a result, the published simulation tools can be used for a number of further studies.

7.1 Zusammenfassung

Dass die Photovoltaik eine Schlüsseltechnologie für die klimaneutrale Energieerzeugung ist, kann als gegeben angesehen werden. Die Frage, inwieweit Perowskit für Photovoltaik-Technologien eingesetzt werden wird, ist noch nicht abschließend geklärt. Aus photophysikalischer Sicht hat es jedoch das Potenzial, einen sinnvollen Beitrag im Energiesektor zu leisten. Es bleibt jedoch abzuwarten, ob Module auf Perowskitbasis in Bezug auf Haltbarkeit und Kosteneffizienz mit den etablierten Technologien konkurrieren können. Der zusätzliche Aspekt der Ionenmigration stellt eine weitere Herausforderung im Bezug zu Degeneration und MPP-tracking dar. In der vorliegenden Arbeit wurde vor allem die Wechselwirkung zwischen Ionenumverteilung, kapazitiven Eigenschaften und Rekombinationsdynamik untersucht. Dazu wurden Impedanzspektroskopie, OCVD- und IV-Kennlinien sowie umfangreiche numerische Drift-Diffusions-

Simulationen eingesetzt. Die Kombination von experimentellen und numerischen Methoden erwies sich als sehr fruchtbar.

Ein geeignetes Modell zur Beschreibung von Solarzellen im Hinblick auf mobile Ionen wurde in Kapitel 4.4 vorgestellt. Die formale mathematische Beschreibung des Modells wurde durch eine Nichtdimensionalisierung und geeignete numerisch lösbare Form umgesetzt. Die Implementierung erfolgte in der Sprache Julia. Durch intelligente Ausnutzung struktureller Eigenschaften der dünn besetzten Gleichungssysteme, automatische Differenzierung und den Einsatz effizienter Integrationsmethoden ist das Simulationswerkzeug nicht nur bemerkenswert schnell in der Lösungsfindung, sondern skaliert auch quasi-linear mit der Gitterauflösung. Das Softwarepaket wurde unter einer Open-Source-Lizenz veröffentlicht,

Bei herkömmlichen Halbleiterdioden werden häufig Kapazitätsmessungen zur Bestimmung der Raumladungsdichte verwendet. Im ersten experimentellen Kapitel 5 wird gezeigt, dass dies zwar auch für die in Perowskiten vorhandene Ionenwanderung möglich ist, aber nicht direkt als dopingbedingt verstanden werden kann, da die Raumladungsverteilung stark von den Voraussetzungen abhängt und durch eine extern angelegte Spannung manipuliert werden kann. Die genaue Form dieses Verhaltens hängt von der Zusammensetzung des Perowskits ab. Dies zeigt u.a., dass experimentelle Ergebnisse nur sehr eingeschränkt im Rahmen konventioneller Halbleiter interpretiert werden können. Dennoch lässt sich das eingebaute Potenzial der Solarzelle bestimmen, wenn die Experimente richtig durchgeführt werden. Eine Aussage über die Art und Ladung der beweglichen Ionen ist ohne weiteren Aufwand nicht möglich, während ihre Anzahl bestimmt werden kann.

Die Simulationen wurden in Kapitel 6 auf experimentelle Daten angewandt. So konnte gezeigt werden, dass mobile Ionen einen wesentlichen Beitrag zur OCVD von Perowskit-Solarzellen leisten. j - V -Charakteristika und OCVD-Transienten, die in Abhängigkeit von Temperatur und Beleuchtungsintensität gemessen wurden, konnten mit einem einzigen globalen Parametersatz gleichzeitig quantitativ modelliert werden. Durch die Simulationen war es ferner möglich, ein einfaches experimentelles Verfahren zur Bestimmung der Konzentration und des Diffusionsvermögens der mobilen Ionen abzuleiten. Die Möglichkeit, verschiedene Experimente einheitlich und temperaturabhängig zu beschreiben, unterstützt das Modell der mobilen Ionen in Perowskiten sehr.

Zusammenfassend kann gesagt werden, dass diese Arbeit einen wichtigen Beitrag zur Aufklärung der ionischen Beiträge zu den (photo)elektrischen Eigenschaften von Perowskit-Solarzellen geleistet hat. Etablierte experimentelle Techniken für konventionelle Halbleiter wurden im Hinblick auf den ionischen Massentransport neu interpretiert, und es wurden neue Methoden vorgeschlagen, um Rückschlüsse auf die für den ionischen Transport charakteristischen Eigenschaften zu ziehen. Das Ergebnis ist, dass die veröffentlichten Simulationswerkzeuge für eine Reihe weiterer Studien genutzt werden können.

Bibliography

- [1] J. R. Flenley and S. M. King: Late Quaternary pollen records from Easter Island. *Nature* **307**(5946) (1984), 47–50. doi: [10.1038/307047a0](https://doi.org/10.1038/307047a0).
- [2] W. Mulloy: A Speculative Reconstruction of Techniques of Carving Transporting and Erecting Easter Island Statues. *Archaeology & Physical Anthropology in Oceania* **5**(1) (1970), 1–23.
- [3] P. S. Arrhenius: XXXI. On the influence of carbonic acid in the air upon the temperature of the ground. *The London, Edinburgh, and Dublin Philosophical Magazine and Journal of Science* **41**(251) (1896), 237–276. doi: [10.1080/14786449608620846](https://doi.org/10.1080/14786449608620846).
- [4] D. M. Etheridge, L. P. Steele, R. L. Langenfelds, et al.: Natural and anthropogenic changes in atmospheric CO₂ over the last 1000 years from air in Antarctic ice and firn. *Journal of Geophysical Research: Atmospheres* **101**(D2) (1996), 4115–4128. doi: [10.1029/95JD03410](https://doi.org/10.1029/95JD03410).
- [5] E. Dlugokencky and P. Tans: *Trends in Atmospheric Carbon Dioxide*. 2021. url: www.esrl.noaa.gov/gmd/ccgg/trends/ (visited on Mar. 4, 2021).
- [6] N. Lenssen, G. Schmidt, J. Hansen, et al.: Improvements in the GISTEMP uncertainty model. *J. Geophys. Res. Atmos.* **124**(12) (2019), 6307–6326. doi: [10.1029/2018JD029522](https://doi.org/10.1029/2018JD029522).
- [7] *Paris Agreement - Status of Ratification*. 2021. url: <https://unfccc.int/process/the-paris-agreement/status-of-ratification> (visited on Mar. 11, 2021).
- [8] M. A. Green: How Did Solar Cells Get So Cheap? *Joule* **3**(3) (2019). doi: [10.1016/j.joule.2019.02.010](https://doi.org/10.1016/j.joule.2019.02.010), 631–633. doi: [10.1016/j.joule.2019.02.010](https://doi.org/10.1016/j.joule.2019.02.010).
- [9] R. H. Wiser, M. Bolinger, B. Hoen, et al.: *Wind Technologies Market Report*. 2020. url: <https://emp.lbl.gov/wind-technologies-market-report> (visited on Mar. 11, 2021).
- [10] bp p.l.c, ed.: *Statistical Review of World Energy*. 2020. url: <https://www.bp.com/content/dam/bp/business-sites/en/global/corporate/pdfs/energy-economics/statistical-review/bp-stats-review-2020-full-report.pdf> (visited on Mar. 4, 2021).
- [11] P. Tipler: *Physics for Scientists and Engineers: Mechanics, Oscillations and Waves, Thermodynamics (Chapters 1-20)*. Macmillan Learning, 2007.

- [12] A. Belghachi: Theoretical Calculation of the Efficiency Limit for Solar Cells. *Solar Cells - New Approaches and Reviews*. InTech, Oct. 2015. doi: [10.5772/58914](https://doi.org/10.5772/58914).
- [13] N. Akhtar, B. Geyer, B. Rockel, P. S. Sommer, and C. Schrum: Accelerating deployment of offshore wind energy alter wind climate and reduce future power generation potentials. *Scientific Reports* **11**(1) (2021), 11826. doi: [10.1038/s41598-021-91283-3](https://doi.org/10.1038/s41598-021-91283-3).
- [14] A. Kleidon: Physical limits of wind energy within the atmosphere and its use as renewable energy: From the theoretical basis to practical implications. *Meteorologische Zeitschrift* (Mar. 2021). doi: [10.1127/metz/2021/1062](https://doi.org/10.1127/metz/2021/1062).
- [15] A. Betz: The Maximum of the Theoretically Possible Exploitation of Wind by Means of a Wind Motor. *Wind Engineering* **37**(4) (2013), 441–446.
- [16] *Best Research-Cell Efficiency Chart*. 2021. url: <https://www.nrel.gov/pv/assets/pdfs/best-research-cell-efficiencies.20200104.pdf> (visited on Mar. 11, 2021).
- [17] S. Bhattacharya and S. John: Beyond 30% Conversion Efficiency in Silicon Solar Cells: A Numerical Demonstration. *Scientific Reports* **9**(1) (Aug. 2019). doi: [10.1038/s41598-019-48981-w](https://doi.org/10.1038/s41598-019-48981-w).
- [18] K. Yoshikawa, H. Kawasaki, W. Yoshida, et al.: Silicon heterojunction solar cell with interdigitated back contacts for a photoconversion efficiency over 26%. *Nature Energy* **2**(5) (Mar. 2017). doi: [10.1038/nenergy.2017.32](https://doi.org/10.1038/nenergy.2017.32).
- [19] M. Green, E. Dunlop, J. Hohl-Ebinger, et al.: Solar cell efficiency tables (version 57). *Progress in Photovoltaics: Research and Applications* **29**(1) (Nov. 2020), 3–15. doi: [10.1002/pip.3371](https://doi.org/10.1002/pip.3371).
- [20] G. Giacchetta, M. Leporini, and B. Marchetti: Evaluation of the environmental benefits of new high value process for the management of the end of life of thin film photovoltaic modules. *Journal of Cleaner Production* **51** (July 2013), 214–224. doi: [10.1016/j.jclepro.2013.01.022](https://doi.org/10.1016/j.jclepro.2013.01.022).
- [21] B. O'Regan and M. Grätzel: A low-cost, high-efficiency solar cell based on dye-sensitized colloidal TiO₂ films. *Nature* **353**(6346) (Oct. 1991), 737–740. doi: [10.1038/353737a0](https://doi.org/10.1038/353737a0).
- [22] C. W. Tang: Two-layer organic photovoltaic cell. *Applied Physics Letters* **48**(2) (Jan. 1986), 183–185. doi: [10.1063/1.96937](https://doi.org/10.1063/1.96937).
- [23] K. Cnops, B. P. Rand, D. Cheyns, et al.: 8.4% efficient fullerene-free organic solar cells exploiting long-range exciton energy transfer. *Nature Communications* **5**(1) (Mar. 2014). doi: [10.1038/ncomms4406](https://doi.org/10.1038/ncomms4406).
- [24] Y. Lin, J. Wang, Z.-G. Zhang, et al.: An Electron Acceptor Challenging Fullerenes for Efficient Polymer Solar Cells. *Advanced Materials* **27**(7) (Jan. 2015), 1170–1174. doi: [10.1002/adma.201404317](https://doi.org/10.1002/adma.201404317).

- [25] Q. Liu, Y. Jiang, K. Jin, et al.: 18% Efficiency organic solar cells. *Science Bulletin* **65**(4) (Feb. 2020), 272–275. doi: [10.1016/j.scib.2020.01.001](https://doi.org/10.1016/j.scib.2020.01.001).
- [26] J. Jeong, M. Kim, J. Seo, et al.: Pseudo-halide anion engineering for α -FAPbI₃ perovskite solar cells. *Nature* **592**(7854) (Apr. 2021), 381–385. doi: [10.1038/s41586-021-03406-5](https://doi.org/10.1038/s41586-021-03406-5).
- [27] S. Kikkawa, S. Sun, Y. Masubuchi, Y. Nagamine, and T. Shihahara: Ferroelectric Response Induced in cis-Type Anion Ordered SrTaO₂N Oxynitride Perovskite. *Chemistry of Materials* **28**(5) (Feb. 2016), 1312–1317. doi: [10.1021/acs.chemmater.5b04149](https://doi.org/10.1021/acs.chemmater.5b04149).
- [28] R. M. Hazen, L. W. Finger, R. J. Angel, et al.: Crystallographic description of phases in the Y-Ba-Cu-O superconductor. *Physical Review B* **35**(13) (May 1987), 7238–7241. doi: [10.1103/physrevb.35.7238](https://doi.org/10.1103/physrevb.35.7238).
- [29] B. Szafraniak, J. Funik, J. Xu, et al.: Semiconducting Metal Oxides: SrTiO₃, BaTiO₃ and BaSrTiO₃ in Gas-Sensing Applications: A Review. *Coatings* **11**(2) (Feb. 2021), 185. doi: [10.3390/coatings11020185](https://doi.org/10.3390/coatings11020185).
- [30] V. M. Goldschmidt: Die Gesetze der Krystallochemie. *Die Naturwissenschaften* **14**(21) (May 1926), 477–485. doi: [10.1007/bf01507527](https://doi.org/10.1007/bf01507527).
- [31] C. Li, K. C. K. Soh, and P. Wu: Formability of ABO₃ perovskites. *Journal of Alloys and Compounds* **372**(1-2) (June 2004), 40–48. doi: [10.1016/j.jallcom.2003.10.017](https://doi.org/10.1016/j.jallcom.2003.10.017).
- [32] M. A. Green, A. Ho-Baillie, and H. J. Snaith: The emergence of perovskite solar cells. *Nature Photonics* **8**(7) (June 2014), 506–514. doi: [10.1038/nphoton.2014.134](https://doi.org/10.1038/nphoton.2014.134).
- [33] Q. Chen, N. D. Marco, Y. (Yang, et al.: Under the spotlight: The organic–inorganic hybrid halide perovskite for optoelectronic applications. *Nano Today* **10**(3) (June 2015), 355–396. doi: [10.1016/j.nantod.2015.04.009](https://doi.org/10.1016/j.nantod.2015.04.009).
- [34] H. Takaba, S. Kimura, and M. K. Alam: Crystal and electronic structures of substituted halide perovskites based on density functional calculation and molecular dynamics. *Chemical Physics* **485-486** (Mar. 2017), 22–28. doi: [10.1016/j.chemphys.2016.12.007](https://doi.org/10.1016/j.chemphys.2016.12.007).
- [35] V. L. Miller and S. C. Tidrow: Perovskites: Temperature and Coordination Dependent Ionic Radii. *Integrated Ferroelectrics* **148**(1) (Jan. 2013), 1–16. doi: [10.1080/10584587.2013.851576](https://doi.org/10.1080/10584587.2013.851576).
- [36] W. Sukmas, V. Sakulsupich, P. Tsuppayakorn-ae, et al.: Preferred oriented cation configurations in high pressure phases IV and V of methylammonium lead iodide perovskite. *Scientific Reports* **10**(1) (Dec. 2020). doi: [10.1038/s41598-020-77852-y](https://doi.org/10.1038/s41598-020-77852-y).
- [37] P. S. Whitfield, N. Herron, W. E. Guise, et al.: Structures, Phase Transitions and Tricritical Behavior of the Hybrid Perovskite Methyl Ammonium Lead Iodide. *Scientific Reports* **6**(1) (Oct. 2016). doi: [10.1038/srep35685](https://doi.org/10.1038/srep35685).

- [38] T. Wang, J. Fan, C.-L. Do-Thanh, et al.: Perovskite Oxide–Halide Solid Solutions: A Platform for Electrocatalysts. *Angewandte Chemie International Edition* **60**(18) (Mar. 2021), 9953–9958. doi: [10.1002/anie.202101120](https://doi.org/10.1002/anie.202101120).
- [39] X. Liang, L. Shi, R. Cao, et al.: Perovskite-Type Solid Solution Nano-Electrocatalysts Enable Simultaneously Enhanced Activity and Stability for Oxygen Evolution. *Advanced Materials* **32**(34) (July 2020), 2001430. doi: [10.1002/adma.202001430](https://doi.org/10.1002/adma.202001430).
- [40] A. Mancini, P. Quadrelli, C. Milanese, et al.: CH₃NH₃Sn_xPb_{1-x}Br₃ Hybrid Perovskite Solid Solution: Synthesis, Structure, and Optical Properties. *Inorganic Chemistry* **54**(18) (Sept. 2015), 8893–8895. doi: [10.1021/acs.inorgchem.5b01843](https://doi.org/10.1021/acs.inorgchem.5b01843).
- [41] C. Lin: Stabilizing Organic–Inorganic Lead Halide Perovskite Solar Cells With Efficiency Beyond 20%. *Frontiers in Chemistry* **8** (July 2020). doi: [10.3389/fchem.2020.00592](https://doi.org/10.3389/fchem.2020.00592).
- [42] E. Mosconi, A. Amat, M. K. Nazeeruddin, M. Grätzel, and F. D. Angelis: First-Principles Modeling of Mixed Halide Organometal Perovskites for Photovoltaic Applications. *The Journal of Physical Chemistry C* **117**(27) (July 2013), 13902–13913. doi: [10.1021/jp4048659](https://doi.org/10.1021/jp4048659).
- [43] A. Poglitsch and D. Weber: Dynamic disorder in methylammoniumtrihalogenoplumbates (II) observed by millimeter-wave spectroscopy. *The Journal of Chemical Physics* **87**(11) (Dec. 1987), 6373–6378. doi: [10.1063/1.453467](https://doi.org/10.1063/1.453467).
- [44] C. Ma, D. Shen, B. Huang, et al.: High performance low-dimensional perovskite solar cells based on a one dimensional lead iodide perovskite. *Journal of Materials Chemistry A* **7**(15) (2019), 8811–8817. doi: [10.1039/c9ta01859j](https://doi.org/10.1039/c9ta01859j).
- [45] R. K. Misra, B.-E. Cohen, L. Iagher, and L. Etgar: Low-Dimensional Organic-Inorganic Halide Perovskite: Structure, Properties, and Applications. *ChemSusChem* **10**(19) (Aug. 2017), 3712–3721. doi: [10.1002/cssc.201701026](https://doi.org/10.1002/cssc.201701026).
- [46] X. Hong, T. Ishihara, and A. Nurmikko: Photoconductivity and electroluminescence in lead iodide based natural quantum well structures. *Solid State Communications* **84**(6) (Nov. 1992), 657–661. doi: [10.1016/0038-1098\(92\)90210-z](https://doi.org/10.1016/0038-1098(92)90210-z).
- [47] J. Mizusaki, K. Arai, and K. Fueki: Ionic conduction of the perovskite-type halides. *Solid State Ionics* **11**(3) (Nov. 1983), 203–211. doi: [10.1016/0167-2738\(83\)90025-5](https://doi.org/10.1016/0167-2738(83)90025-5).
- [48] E. L. Unger, E. T. Hoke, C. D. Bailie, et al.: Hysteresis and transient behavior in current–voltage measurements of hybrid-perovskite absorber solar cells. *Energy Environ. Sci.* **7**(11) (2014), 3690–3698. doi: [10.1039/c4ee02465f](https://doi.org/10.1039/c4ee02465f).
- [49] H. J. Snaith, A. Abate, J. M. Ball, et al.: Anomalous Hysteresis in Perovskite Solar Cells. *The Journal of Physical Chemistry Letters* **5**(9) (Apr. 2014), 1511–1515. doi: [10.1021/jz500113x](https://doi.org/10.1021/jz500113x).

- [50] Q. Lin, A. Armin, R. C. R. Nagiri, P. L. Burn, and P. Meredith: Electro-optics of perovskite solar cells. *Nature Photonics* **9**(2) (Dec. 2014), 106–112. doi: [10.1038/nphoton.2014.284](https://doi.org/10.1038/nphoton.2014.284).
- [51] E. J. Juarez-Perez, R. S. Sanchez, L. Badia, et al.: Photoinduced Giant Dielectric Constant in Lead Halide Perovskite Solar Cells. *The Journal of Physical Chemistry Letters* **5**(13) (June 2014), 2390–2394. doi: [10.1021/jz5011169](https://doi.org/10.1021/jz5011169).
- [52] E. T. Hoke, D. J. Slotcavage, E. R. Dohner, et al.: Reversible photo-induced trap formation in mixed-halide hybrid perovskites for photovoltaics. *Chemical Science* **6**(1) (2015), 613–617. doi: [10.1039/c4sc03141e](https://doi.org/10.1039/c4sc03141e).
- [53] S. Bae, S. Kim, S.-W. Lee, et al.: Electric-Field-Induced Degradation of Methylammonium Lead Iodide Perovskite Solar Cells. *The Journal of Physical Chemistry Letters* **7**(16) (July 2016), 3091–3096. doi: [10.1021/acs.jpcclett.6b01176](https://doi.org/10.1021/acs.jpcclett.6b01176).
- [54] Y. Deng, Z. Xiao, and J. Huang: Light-Induced Self-Poling Effect on Organometal Trihalide Perovskite Solar Cells for Increased Device Efficiency and Stability. *Advanced Energy Materials* **5**(20) (Aug. 2015), 1500721. doi: [10.1002/aenm.201500721](https://doi.org/10.1002/aenm.201500721).
- [55] N. W. Ashcroft and N. D. Mermin: *Solid State Physics*. Vol. 9. 1. 1978, p. 620. 826 pp. doi: [10.1002/piuz.19780090109](https://doi.org/10.1002/piuz.19780090109). New York.
- [56] Z. Xiao, Y. Yuan, Y. Shao, et al.: Giant switchable photovoltaic effect in organometal trihalide perovskite devices. *Nature Materials* **14**(2) (Dec. 2014), 193–198. doi: [10.1038/nmat4150](https://doi.org/10.1038/nmat4150).
- [57] T. Leijtens, E. T. Hoke, G. Grancini, et al.: Mapping Electric Field-Induced Switchable Poling and Structural Degradation in Hybrid Lead Halide Perovskite Thin Films. *Advanced Energy Materials* **5**(20) (Sept. 2015), 1500962. doi: [10.1002/aenm.201500962](https://doi.org/10.1002/aenm.201500962).
- [58] C. Caddeo, M. I. Saba, S. Meloni, A. Filippetti, and A. Mattoni: Collective Molecular Mechanisms in the $\text{CH}_3\text{NH}_3\text{PbI}_3$ dissolution by Liquid Water. *ACS Nano* **11**(9) (Aug. 2017), 9183–9190. doi: [10.1021/acsnano.7b04116](https://doi.org/10.1021/acsnano.7b04116).
- [59] J. Höcker, M. Ozcan, S. Hammer, et al.: Seed crystal free growth of high-quality double cation – double halide perovskite single crystals for optoelectronic applications. *Journal of Materials Chemistry C* **8**(24) (2020), 8275–8283. doi: [10.1039/d0tc01617a](https://doi.org/10.1039/d0tc01617a).
- [60] Y. Yuan and J. Huang: Ion Migration in Organometal Trihalide Perovskite and Its Impact on Photovoltaic Efficiency and Stability. *Accounts of Chemical Research* **49**(2) (Jan. 2016), 286–293. doi: [10.1021/acs.accounts.5b00420](https://doi.org/10.1021/acs.accounts.5b00420).
- [61] N.-G. Park, M. Grätzel, and T. Miyasaka, eds.: *Organic-Inorganic Halide Perovskite Photovoltaics. From Fundamentals to Device Architectures*. Vol. 1. Springer International Publishing, 2016. Chap. 2, pp. 137–149. 366 pp. doi: [10.1007/978-3-319-35114-8](https://doi.org/10.1007/978-3-319-35114-8).

- [62] C. Eames, J. M. Frost, P. R. F. Barnes, et al.: Ionic transport in hybrid lead iodide perovskite solar cells. *Nature Communications* **6**(1) (June 2015). doi: [10.1038/ncomms8497](https://doi.org/10.1038/ncomms8497).
- [63] J. M. Azpiroz, E. Mosconi, J. Bisquert, and F. D. Angelis: Defect migration in methylammonium lead iodide and its role in perovskite solar cell operation. *Energy & Environmental Science* **8**(7) (2015), 2118–2127. doi: [10.1039/c5ee01265a](https://doi.org/10.1039/c5ee01265a).
- [64] J. Haruyama, K. Sodeyama, L. Han, and Y. Tateyama: First-Principles Study of Ion Diffusion in Perovskite Solar Cell Sensitizers. *Journal of the American Chemical Society* **137**(32) (Aug. 2015), 10048–10051. doi: [10.1021/jacs.5b03615](https://doi.org/10.1021/jacs.5b03615).
- [65] P. Delugas, C. Caddeo, A. Filippetti, and A. Mattoni: Thermally Activated Point Defect Diffusion in Methylammonium Lead Trihalide: Anisotropic and Ultrahigh Mobility of Iodine. *The Journal of Physical Chemistry Letters* **7**(13) (June 2016), 2356–2361. doi: [10.1021/acs.jpcllett.6b00963](https://doi.org/10.1021/acs.jpcllett.6b00963).
- [66] S. Meloni, T. Moehl, W. Tress, et al.: Ionic polarization-induced current–voltage hysteresis in $\text{CH}_3\text{NH}_3\text{PbX}_3$ perovskite solar cells. *Nature Communications* **7**(1) (Feb. 2016). doi: [10.1038/ncomms10334](https://doi.org/10.1038/ncomms10334).
- [67] S. Maheshwari, M. B. Fridriksson, S. Seal, J. Meyer, and F. C. Grozema: The Relation between Rotational Dynamics of the Organic Cation and Phase Transitions in Hybrid Halide Perovskites. *The Journal of Physical Chemistry C* **123**(23) (May 2019), 14652–14661. doi: [10.1021/acs.jpcc.9b02736](https://doi.org/10.1021/acs.jpcc.9b02736).
- [68] R. Garca-Rodrguez, D. Ferdani, S. Pering, P. J. Baker, and P. J. Cameron: Influence of bromide content on iodide migration in inverted $\text{MAPb}(\text{I}_{1-x}\text{Br}_x)_3$ perovskite solar cells. *Journal of Materials Chemistry A* **7**(39) (2019), 22604–22614. doi: [10.1039/c9ta08848b](https://doi.org/10.1039/c9ta08848b).
- [69] Y.-C. Zhao, W.-K. Zhou, X. Zhou, et al.: Quantification of light-enhanced ionic transport in lead iodide perovskite thin films and its solar cell applications. *Light: Science & Applications* **6**(5) (Oct. 2016), e16243–e16243. doi: [10.1038/lsa.2016.243](https://doi.org/10.1038/lsa.2016.243).
- [70] W. Zhou, S. Chen, Y. Zhao, et al.: Constructing CsPbBr_3 Cluster Passivated-Triple Cation Perovskite for Highly Efficient and Operationally Stable Solar Cells. *Advanced Functional Materials* **29**(14) (Feb. 2019), 1809180. doi: [10.1002/adfm.201809180](https://doi.org/10.1002/adfm.201809180).
- [71] T. Zhang, S. H. Cheung, X. Meng, et al.: Pinning Down the Anomalous Light Soaking Effect toward High-Performance and Fast-Response Perovskite Solar Cells: The Ion-Migration-Induced Charge Accumulation. *The Journal of Physical Chemistry Letters* **8**(20) (Oct. 2017), 5069–5076. doi: [10.1021/acs.jpcllett.7b02160](https://doi.org/10.1021/acs.jpcllett.7b02160).

- [72] H. Lee, S. Gaiaschi, P. Chapon, et al.: Effect of Halide Ion Migration on the Electrical Properties of Methylammonium Lead Tri-Iodide Perovskite Solar Cells. *The Journal of Physical Chemistry C* **123**(29) (July 2019), 17728–17734. doi: [10.1021/acs.jpcc.9b04662](https://doi.org/10.1021/acs.jpcc.9b04662).
- [73] C.-S. Jiang, M. Yang, Y. Zhou, et al.: Carrier separation and transport in perovskite solar cells studied by nanometre-scale profiling of electrical potential. *Nature Communications* **6**(1) (Sept. 2015). doi: [10.1038/ncomms9397](https://doi.org/10.1038/ncomms9397).
- [74] K. Tvingstedt, K. Vandewal, F. Zhang, and O. Inganäs: On the Dissociation Efficiency of Charge Transfer Excitons and Frenkel Excitons in Organic Solar Cells: A Luminescence Quenching Study. *The Journal of Physical Chemistry C* **114**(49) (Nov. 2010), 21824–21832. doi: [10.1021/jp107587h](https://doi.org/10.1021/jp107587h).
- [75] S.-J. Park and M.-K. Seo: Interface Applications in Nanomaterials. *Interface Science and Composites*. Elsevier, 2011, 333–429. doi: [10.1016/b978-0-12-375049-5.00005-0](https://doi.org/10.1016/b978-0-12-375049-5.00005-0).
- [76] X. Chen, H. Lu, Y. Yang, and M. C. Beard: Excitonic Effects in Methylammonium Lead Halide Perovskites. *The Journal of Physical Chemistry Letters* **9**(10) (May 2018), 2595–2603. doi: [10.1021/acs.jpcclett.8b00526](https://doi.org/10.1021/acs.jpcclett.8b00526).
- [77] Y. Yamada, T. Nakamura, M. Endo, A. Wakamiya, and Y. Kanemitsu: Photoelectronic Responses in Solution-Processed Perovskite $CH_3NH_3PbI_3$ Solar Cells Studied by Photoluminescence and Photoabsorption Spectroscopy. *IEEE Journal of Photovoltaics* **5**(1) (Jan. 2015), 401–405. doi: [10.1109/jphotov.2014.2364115](https://doi.org/10.1109/jphotov.2014.2364115).
- [78] J. Even, L. Pedesseau, and C. Katan: Analysis of Multivalley and Multibandgap Absorption and Enhancement of Free Carriers Related to Exciton Screening in Hybrid Perovskites. *The Journal of Physical Chemistry C* **118**(22) (May 2014), 11566–11572. doi: [10.1021/jp503337a](https://doi.org/10.1021/jp503337a).
- [79] A. Miyata, A. Mitoglu, P. Plochocka, et al.: Direct measurement of the exciton binding energy and effective masses for charge carriers in organic–inorganic tri-halide perovskites. *Nature Physics* **11**(7) (June 2015), 582–587. doi: [10.1038/nphys3357](https://doi.org/10.1038/nphys3357).
- [80] F. Ruf, A. Magin, M. Schultes, et al.: Excitonic nature of optical transitions in electroabsorption spectra of perovskite solar cells. *Applied Physics Letters* **112**(8) (Feb. 2018), 083902. doi: [10.1063/1.5017943](https://doi.org/10.1063/1.5017943).
- [81] B. Li, Y. Zhang, L. Fu, et al.: Two-dimensional black phosphorous induced exciton dissociation efficiency enhancement for high-performance all-inorganic $CsPbI_3$ perovskite photovoltaics. *Journal of Materials Chemistry A* **7**(39) (2019), 22539–22549. doi: [10.1039/c9ta06016b](https://doi.org/10.1039/c9ta06016b).
- [82] J.-P. Yang, M. Meissner, T. Yamaguchi, et al.: Band Dispersion and Hole Effective Mass of Methylammonium Lead Iodide Perovskite. *Solar RRL* **2**(10) (July 2018), 1800132. doi: [10.1002/solr.201800132](https://doi.org/10.1002/solr.201800132).

- [83] S. Colella, E. Mosconi, P. Fedeli, et al.: MAPbI₃ – xCl_x Mixed Halide Perovskite for Hybrid Solar Cells: The Role of Chloride as Dopant on the Transport and Structural Properties. *Chemistry of Materials* **25**(22) (Nov. 2013), 4613–4618. doi: [10.1021/cm402919x](https://doi.org/10.1021/cm402919x).
- [84] M. M. Lee, J. Teuscher, T. Miyasaka, T. N. Murakami, and H. J. Snaith: Efficient Hybrid Solar Cells Based on Meso-Superstructured Organometal Halide Perovskites. *Science* **338**(6107) (Oct. 2012), 643–647. doi: [10.1126/science.1228604](https://doi.org/10.1126/science.1228604).
- [85] F. Staub, H. Hempel, J.-C. Hebig, et al.: Beyond Bulk Lifetimes: Insights into Lead Halide Perovskite Films from Time-Resolved Photoluminescence. *Physical Review Applied* **6**(4) (Oct. 2016). doi: [10.1103/physrevapplied.6.044017](https://doi.org/10.1103/physrevapplied.6.044017).
- [86] E. Menéndez-Proupin, P. Palacios, P. Wahnón, and J. C. Conesa: Self-consistent relativistic band structure of the CH₃NH₃PbI₃ perovskite. *Physical Review B* **90**(4) (July 2014). doi: [10.1103/physrevb.90.045207](https://doi.org/10.1103/physrevb.90.045207).
- [87] D. Ompong, G. Inkoom, and J. Singh: Effective mass of heavy, light, and spin split-off band electron and hole g-factor in cubic perovskite materials. *Journal of Applied Physics* **128**(23) (Dec. 2020), 235109. doi: [10.1063/5.0028266](https://doi.org/10.1063/5.0028266).
- [88] T. M. Brenner, D. A. Egger, L. Kronik, G. Hodes, and D. Cahen: Hybrid organic—inorganic perovskites: low-cost semiconductors with intriguing charge-transport properties. *Nature Reviews Materials* **1**(1) (Jan. 2016). doi: [10.1038/natrevmats.2015.7](https://doi.org/10.1038/natrevmats.2015.7).
- [89] F. Brivio, K. T. Butler, A. Walsh, and M. van Schilfgaarde: Relativistic quasiparticle self-consistent electronic structure of hybrid halide perovskite photovoltaic absorbers. *Physical Review B* **89**(15) (Apr. 2014). doi: [10.1103/physrevb.89.155204](https://doi.org/10.1103/physrevb.89.155204).
- [90] J. R. Harwell, T. K. Baikie, I. D. Baikie, et al.: Probing the energy levels of perovskite solar cells via Kelvin probe and UV ambient pressure photoemission spectroscopy. *Physical Chemistry Chemical Physics* **18**(29) (2016), 19738–19745. doi: [10.1039/c6cp02446g](https://doi.org/10.1039/c6cp02446g).
- [91] J. Haddad, B. Krogmeier, B. Klingebiel, et al.: Analyzing Interface Recombination in Lead-Halide Perovskite Solar Cells with Organic and Inorganic Hole-Transport Layers. *Advanced Materials Interfaces* **7**(16) (June 2020), 2000366. doi: [10.1002/admi.202000366](https://doi.org/10.1002/admi.202000366).
- [92] F. Brivio, A. B. Walker, and A. Walsh: Structural and electronic properties of hybrid perovskites for high-efficiency thin-film photovoltaics from first-principles. *APL Materials* **1**(4) (Oct. 2013), 042111. doi: [10.1063/1.4824147](https://doi.org/10.1063/1.4824147).
- [93] C. Quarti, E. Mosconi, and F. D. Angelis: Interplay of Orientational Order and Electronic Structure in Methylammonium Lead Iodide: Implications for Solar Cell Operation. *Chemistry of Materials* **26**(22) (Nov. 2014), 6557–6569. doi: [10.1021/cm5032046](https://doi.org/10.1021/cm5032046).

- [94] C. Motta, F. El-Mellouhi, S. Kais, et al.: Revealing the role of organic cations in hybrid halide perovskite $\text{CH}_3\text{NH}_3\text{PbI}_3$. *Nature Communications* **6**(1) (Apr. 2015). doi: [10.1038/ncomms8026](https://doi.org/10.1038/ncomms8026).
- [95] F. Zheng, L. Z. Tan, S. Liu, and A. M. Rappe: Rashba Spin–Orbit Coupling Enhanced Carrier Lifetime in $\text{CH}_3\text{NH}_3\text{PbI}_3$. *Nano Letters* **15**(12) (Nov. 2015), 7794–7800. doi: [10.1021/acs.nanolett.5b01854](https://doi.org/10.1021/acs.nanolett.5b01854).
- [96] T. Wang, B. Daiber, J. M. Frost, et al.: Indirect to direct bandgap transition in methylammonium lead halide perovskite. *Energy & Environmental Science* **10**(2) (2017), 509–515. doi: [10.1039/c6ee03474h](https://doi.org/10.1039/c6ee03474h).
- [97] P. Nandi, S. K. Pandey, C. Giri, et al.: Probing the Electronic Structure of Hybrid Perovskites in the Orientationally Disordered Cubic Phase. *The Journal of Physical Chemistry Letters* **11**(14) (July 2020), 5719–5727. doi: [10.1021/acs.jpcclett.0c01386](https://doi.org/10.1021/acs.jpcclett.0c01386).
- [98] L. Calió, S. Kazim, M. Grätzel, and S. Ahmad: Hole-Transport Materials for Perovskite Solar Cells. *Angewandte Chemie International Edition* **55**(47) (Oct. 2016), 14522–14545. doi: [10.1002/anie.201601757](https://doi.org/10.1002/anie.201601757).
- [99] J. E. N. Swallow, B. A. D. Williamson, T. J. Whittles, et al.: Self-Compensation in Transparent Conducting F-Doped SnO_2 . *Advanced Functional Materials* **28**(4) (Nov. 2017), 1701900. doi: [10.1002/adfm.201701900](https://doi.org/10.1002/adfm.201701900).
- [100] S. Bhattarai, A. Sharma, D. Muchahary, M. Gogoi, and T. Das: Carrier transport layer free perovskite solar cell for enhancing the efficiency: A simulation study. *Optik* **243** (Oct. 2021), 167492. doi: [10.1016/j.jjleo.2021.167492](https://doi.org/10.1016/j.jjleo.2021.167492).
- [101] M. Jin, S. S. Kim, M. Yoon, et al.: Mesoporous Inverse Opal TiO_2 Film as Light Scattering Layer for Dye-Sensitized Solar Cell. *Journal of Nanoscience and Nanotechnology* **12**(1) (Jan. 2012), 815–821. doi: [10.1166/jnn.2012.5372](https://doi.org/10.1166/jnn.2012.5372).
- [102] H. Tian, B. Xu, H. Chen, E. M. J. Johansson, and G. Boschloo: Solid-State Perovskite-Sensitized p-Type Mesoporous Nickel Oxide Solar Cells. *ChemSusChem* **7**(8) (Apr. 2014), 2150–2153. doi: [10.1002/cssc.201402032](https://doi.org/10.1002/cssc.201402032).
- [103] H. Abdy, A. Aletayeb, M. Kolahdouz, and E. A. Soleimani: Investigation of metal-nickel oxide contacts used for perovskite solar cell. *AIP Advances* **9**(1) (Jan. 2019), 015216. doi: [10.1063/1.5063475](https://doi.org/10.1063/1.5063475).
- [104] P. Lenard: Ueber die lichtelektrische Wirkung. *Annalen der Physik* **313**(5) (1902), 149–198. doi: [10.1002/andp.19023130510](https://doi.org/10.1002/andp.19023130510).
- [105] A. Einstein: Über einen die Erzeugung und Verwandlung des Lichtes betreffenden heuristischen Gesichtspunkt. *Annalen der Physik* **322**(6) (1905), 132–148. doi: [10.1002/andp.19053220607](https://doi.org/10.1002/andp.19053220607).

- [106] S. Sze and K. K. Ng: *Physics of Semiconductor Devices*. John Wiley & Sons, Inc., Apr. 2006. doi: [10.1002/0470068329](https://doi.org/10.1002/0470068329).
- [107] P. Würfel and U. Würfel: *Physics of Solar Cells - From Basic Principles to Advanced Concepts*. New York: John Wiley & Sons, 2016.
- [108] P. Caprioglio, M. Stolterfoht, C. M. Wolff, et al.: On the Relation between the Open-Circuit Voltage and Quasi-Fermi Level Splitting in Efficient Perovskite Solar Cells. *Advanced Energy Materials* **9**(33) (July 2019), 1901631. doi: [10.1002/aenm.201901631](https://doi.org/10.1002/aenm.201901631).
- [109] M. Stolterfoht, C. M. Wolff, J. A. Márquez, et al.: Visualization and suppression of interfacial recombination for high-efficiency large-area pin perovskite solar cells. *Nature Energy* **3**(10) (July 2018), 847–854. doi: [10.1038/s41560-018-0219-8](https://doi.org/10.1038/s41560-018-0219-8).
- [110] W. B. Joyce and R. W. Dixon: Analytic approximations for the Fermi energy of an ideal Fermi gas. *Applied Physics Letters* **31**(5) (Sept. 1977), 354–356. doi: [10.1063/1.89697](https://doi.org/10.1063/1.89697).
- [111] U. Rau, U. W. Paetzold, and T. Kirchartz: Thermodynamics of light management in photovoltaic devices. *Physical Review B* **90**(3) (July 2014). doi: [10.1103/physrevb.90.035211](https://doi.org/10.1103/physrevb.90.035211).
- [112] W. Raja, M. D. Bastiani, T. G. Allen, et al.: Photon recycling in perovskite solar cells and its impact on device design. *Nanophotonics* **10**(8) (June 2020), 2023–2042. doi: [10.1515/nanoph-2021-0067](https://doi.org/10.1515/nanoph-2021-0067).
- [113] R. Brenes, M. Laitz, J. Jean, D. W. deQuilletes, and V. Bulovi: Benefit from Photon Recycling at the Maximum-Power Point of State-of-the-Art Perovskite Solar Cells. *Physical Review Applied* **12**(1) (July 2019). doi: [10.1103/physrevapplied.12.014017](https://doi.org/10.1103/physrevapplied.12.014017).
- [114] C. Wehrenfennig, G. E. Eperon, M. B. Johnston, H. J. Snaith, and L. M. Herz: High Charge Carrier Mobilities and Lifetimes in Organolead Trihalide Perovskites. *Advanced Materials* **26**(10) (Dec. 2013), 1584–1589. doi: [10.1002/adma.201305172](https://doi.org/10.1002/adma.201305172).
- [115] C.-t. Sah, R. Noyce, and W. Shockley: Carrier Generation and Recombination in P-N Junctions and P-N Junction Characteristics. *Proceedings of the IRE* **45**(9) (Sept. 1957), 1228–1243. doi: [10.1109/jrproc.1957.278528](https://doi.org/10.1109/jrproc.1957.278528).
- [116] W. Shockley and W. T. Read: Statistics of the Recombinations of Holes and Electrons. *Physical Review* **87**(5) (Sept. 1952), 835–842. doi: [10.1103/physrev.87.835](https://doi.org/10.1103/physrev.87.835).
- [117] H. F. Haneef, A. M. Zeidell, and O. D. Jurchescu: Charge carrier traps in organic semiconductors: a review on the underlying physics and impact on electronic devices. *Journal of Materials Chemistry C* **8**(3) (2020), 759–787. doi: [10.1039/c9tc05695e](https://doi.org/10.1039/c9tc05695e).
- [118] W. Shockley: The Theory of p-n Junctions in Semiconductors and p-n Junction Transistors. *Bell System Technical Journal* **28**(3) (July 1949), 435–489. doi: [10.1002/j.1538-7305.1949.tb03645.x](https://doi.org/10.1002/j.1538-7305.1949.tb03645.x).

- [119] W. Shockley and H. J. Queisser: Detailed Balance Limit of Efficiency of p-n Junction Solar Cells. *Journal of Applied Physics* **32**(3) (Mar. 1961), 510–519. doi: [10.1063/1.1736034](https://doi.org/10.1063/1.1736034).
- [120] J. H. Lambert: *Photometria sive de mensura et gradibus luminis, colorum et umbrae*. la. sumptibus vidvae Eberhardi Klett..., 1760. doi: [10.3931/E-RARA-9488](https://doi.org/10.3931/E-RARA-9488).
- [121] A. Höpe and K.-O. Hauer: Three-dimensional appearance characterization of diffuse standard reflection materials. *Metrologia* **47**(3) (Apr. 2010), 295–304. doi: [10.1088/0026-1394/47/3/021](https://doi.org/10.1088/0026-1394/47/3/021).
- [122] *Tables for Reference Solar Spectral Irradiances: Direct Normal and Hemispherical on 37 Tilted Surface*. doi: [10.1520/g0173-03r20](https://doi.org/10.1520/g0173-03r20).
- [123] E. L. Unger, A. Czudek, H.-S. Kim, and W. Tress: Current-voltage analysis: lessons learned from hysteresis. *Characterization Techniques for Perovskite Solar Cell Materials*. Elsevier, 2020, 81–108. doi: [10.1016/b978-0-12-814727-6.00004-9](https://doi.org/10.1016/b978-0-12-814727-6.00004-9).
- [124] O. Almora, I. Zarazua, E. Mas-Marza, et al.: Capacitive Dark Currents, Hysteresis, and Electrode Polarization in Lead Halide Perovskite Solar Cells. *The Journal of Physical Chemistry Letters* **6**(9) (Apr. 2015), 1645–1652. doi: [10.1021/acs.jpcllett.5b00480](https://doi.org/10.1021/acs.jpcllett.5b00480).
- [125] N. E. Courtier, J. M. Cave, J. M. Foster, A. B. Walker, and G. Richardson: How transport layer properties affect perovskite solar cell performance: insights from a coupled charge transport/ion migration model. *Energy & Environmental Science* **12**(1) (2019), 396–409. doi: [10.1039/c8ee01576g](https://doi.org/10.1039/c8ee01576g).
- [126] H.-S. Kim and N.-G. Park: Parameters Affecting I–V Hysteresis of CH₃NH₃PbI₃ Perovskite Solar Cells: Effects of Perovskite Crystal Size and Mesoporous TiO₂ Layer. *The Journal of Physical Chemistry Letters* **5**(17) (Aug. 2014), 2927–2934. doi: [10.1021/jz501392m](https://doi.org/10.1021/jz501392m).
- [127] R. S. Sanchez, V. Gonzalez-Pedro, J.-W. Lee, et al.: Slow Dynamic Processes in Lead Halide Perovskite Solar Cells. Characteristic Times and Hysteresis. *The Journal of Physical Chemistry Letters* **5**(13) (June 2014), 2357–2363. doi: [10.1021/jz5011187](https://doi.org/10.1021/jz5011187).
- [128] T. J. Jacobsson, J.-P. Correa-Baena, M. Pazoki, et al.: Exploration of the compositional space for mixed lead halogen perovskites for high efficiency solar cells. *Energy & Environmental Science* **9**(5) (2016), 1706–1724. doi: [10.1039/c6ee00030d](https://doi.org/10.1039/c6ee00030d).
- [129] S. N. Habisreutinger, N. K. Noel, and H. J. Snaith: Hysteresis Index: A Figure without Merit for Quantifying Hysteresis in Perovskite Solar Cells. *ACS Energy Letters* **3**(10) (Sept. 2018), 2472–2476. doi: [10.1021/acsenergylett.8b01627](https://doi.org/10.1021/acsenergylett.8b01627).
- [130] A. Dualeh, T. Moehl, N. Tétreault, et al.: Impedance Spectroscopic Analysis of Lead Iodide Perovskite-Sensitized Solid-State Solar Cells. *ACS Nano* **8**(1) (Dec. 2013), 362–373. doi: [10.1021/nn404323g](https://doi.org/10.1021/nn404323g).

- [131] K. T. Butler, J. M. Frost, and A. Walsh: Ferroelectric materials for solar energy conversion: photoferroics revisited. *Energy & Environmental Science* **8**(3) (2015), 838–848. doi: [10.1039/c4ee03523b](https://doi.org/10.1039/c4ee03523b).
- [132] J. Carrillo, A. Guerrero, S. Rahimnejad, et al.: Ionic Reactivity at Contacts and Aging of Methylammonium Lead Triiodide Perovskite Solar Cells. *Advanced Energy Materials* **6**(9) (Feb. 2016), 1502246. doi: [10.1002/aenm.201502246](https://doi.org/10.1002/aenm.201502246).
- [133] J. Carrillo, A. Guerrero, S. Rahimnejad, et al.: Ionic Reactivity at Contacts and Aging of Methylammonium Lead Triiodide Perovskite Solar Cells. *Advanced Energy Materials* **6**(9) (Feb. 2016), 1502246. doi: [10.1002/aenm.201502246](https://doi.org/10.1002/aenm.201502246).
- [134] S. Kim, S. Bae, S.-W. Lee, et al.: Relationship between ion migration and interfacial degradation of CH₃NH₃PbI₃ perovskite solar cells under thermal conditions. *Scientific Reports* **7**(1) (Apr. 2017). doi: [10.1038/s41598-017-00866-6](https://doi.org/10.1038/s41598-017-00866-6).
- [135] P. Calado, A. M. Telford, D. Bryant, et al.: Evidence for ion migration in hybrid perovskite solar cells with minimal hysteresis. *Nature Communications* **7**(1) (Dec. 2016). doi: [10.1038/ncomms13831](https://doi.org/10.1038/ncomms13831).
- [136] N. E. Courtier, J. M. Cave, A. B. Walker, G. Richardson, and J. M. Foster: IonMonger: a free and fast planar perovskite solar cell simulator with coupled ion vacancy and charge carrier dynamics. *Journal of Computational Electronics* **18**(4) (Sept. 2019), 1435–1449. doi: [10.1007/s10825-019-01396-2](https://doi.org/10.1007/s10825-019-01396-2).
- [137] J. Wu, Y. Li, Y. Li, et al.: Using hysteresis to predict the charge recombination properties of perovskite solar cells. *Journal of Materials Chemistry A* **9**(10) (2021), 6382–6392. doi: [10.1039/d0ta12046d](https://doi.org/10.1039/d0ta12046d).
- [138] Y. Yi, J. E. Lyon, M. M. Beerbom, and R. Schlaf: Characterization of indium tin oxide surfaces and interfaces using low intensity x-ray photoemission spectroscopy. *Journal of Applied Physics* **100**(9) (Nov. 2006), 093719. doi: [10.1063/1.2361089](https://doi.org/10.1063/1.2361089).
- [139] H. Kim, C. M. Gilmore, A. Piqué, et al.: Electrical, optical, and structural properties of indium–tin–oxide thin films for organic light-emitting devices. *Journal of Applied Physics* **86**(11) (Dec. 1999), 6451–6461. doi: [10.1063/1.371708](https://doi.org/10.1063/1.371708).
- [140] R. Schlaf, H. Murata, and Z. Kafafi: Work function measurements on indium tin oxide films. *Journal of Electron Spectroscopy and Related Phenomena* **120**(1-3) (Oct. 2001), 149–154. doi: [10.1016/s0368-2048\(01\)00310-3](https://doi.org/10.1016/s0368-2048(01)00310-3).
- [141] K. Masumura, T. Oka, K. Kinashi, W. Sakai, and N. Tsutsumi: Photorefractive dynamics in poly(triarylamine)-based polymer composite: an approach utilizing a second electron trap to reduce the photoconductivity. *Optical Materials Express* **8**(2) (Jan. 2018), 401. doi: [10.1364/ome.8.000401](https://doi.org/10.1364/ome.8.000401).

- [142] M. D. Irwin, D. B. Buchholz, A. W. Hains, R. P. H. Chang, and T. J. Marks: p-Type semiconducting nickel oxide as an efficiency-enhancing anode interfacial layer in polymer bulk-heterojunction solar cells. *Proceedings of the National Academy of Sciences* **105**(8) (Feb. 2008), 2783–2787. doi: [10.1073/pnas.0711990105](https://doi.org/10.1073/pnas.0711990105).
- [143] J. H. Heo, S. H. Im, J. H. Noh, et al.: Efficient inorganic–organic hybrid heterojunction solar cells containing perovskite compound and polymeric hole conductors. *Nature Photonics* **7**(6) (May 2013), 486–491. doi: [10.1038/nphoton.2013.80](https://doi.org/10.1038/nphoton.2013.80).
- [144] J. Endres, M. Kulbak, L. Zhao, et al.: Electronic structure of the CsPbBr₃/polytriarylamine (PTAA) system. *Journal of Applied Physics* **121**(3) (Jan. 2017), 035304. doi: [10.1063/1.4974471](https://doi.org/10.1063/1.4974471).
- [145] S. Tsarev, I. K. Yakushchenko, S. Y. Luchkin, et al.: A new polytriarylamine derivative for dopant-free high-efficiency perovskite solar cells. *Sustainable Energy & Fuels* **3**(10) (2019), 2627–2632. doi: [10.1039/c9se00448c](https://doi.org/10.1039/c9se00448c).
- [146] J. Panidi, A. F. Paterson, D. Khim, et al.: Remarkable Enhancement of the Hole Mobility in Several Organic Small-Molecules, Polymers, and Small-Molecule:Polymer Blend Transistors by Simple Admixing of the Lewis Acid p-Dopant B(C₆F₅)₃. *Advanced Science* **5**(1) (Oct. 2017), 1700290. doi: [10.1002/advs.201700290](https://doi.org/10.1002/advs.201700290).
- [147] S. Schols, L. V. Willigenburg, S. Steudel, J. Genoe, and P. Heremans: Pulsed Excitation of OLEDs With a Remote Metallic Cathode. *IEEE Journal of Quantum Electronics* **46**(1) (Jan. 2010), 62–67. doi: [10.1109/jqe.2009.2027136](https://doi.org/10.1109/jqe.2009.2027136).
- [148] Q. J. Sun, J. H. Hou, C. H. Yang, Y. F. Li, and Y. Yang: Enhanced performance of white polymer light-emitting diodes using polymer blends as hole-transporting layers. *Applied Physics Letters* **89**(15) (Oct. 2006), 153501. doi: [10.1063/1.2360248](https://doi.org/10.1063/1.2360248).
- [149] M.-B. Madec, J. J. Morrison, M. Rabjohns, M. L. Turner, and S. G. Yeates: Effect of poly(triarylamine) molar mass distribution on organic field effect transistor behaviour. *Organic Electronics* **11**(4) (Apr. 2010), 686–691. doi: [10.1016/j.orgel.2009.12.015](https://doi.org/10.1016/j.orgel.2009.12.015).
- [150] A. Intaniwet, J. L. Keddie, M. Shkunov, and P. J. Sellin: High charge-carrier mobilities in blends of poly(triarylamine) and TIPS-pentacene leading to better performing X-ray sensors. *Organic Electronics* **12**(11) (Nov. 2011), 1903–1908. doi: [10.1016/j.orgel.2011.08.003](https://doi.org/10.1016/j.orgel.2011.08.003).
- [151] B. Dänekamp, N. Droseros, D. Tsokkou, et al.: Influence of hole transport material ionization energy on the performance of perovskite solar cells. *Journal of Materials Chemistry C* **7**(3) (2019), 523–527. doi: [10.1039/c8tc05372c](https://doi.org/10.1039/c8tc05372c).
- [152] C. Momblona, L. Gil-Escrig, E. Bandiello, et al.: Efficient vacuum deposited p-i-n and n-i-p perovskite solar cells employing doped charge transport layers. *Energy Environ. Sci.* **9**(11) (2016), 3456–3463. doi: [10.1039/c6ee02100j](https://doi.org/10.1039/c6ee02100j).

- [153] S. S. Dalal, D. M. Walters, I. Lyubimov, J. J. de Pablo, and M. D. Ediger: Tunable molecular orientation and elevated thermal stability of vapor-deposited organic semiconductors. *Proceedings of the National Academy of Sciences* **112**(14) (Mar. 2015), 4227–4232. doi: [10.1073/pnas.1421042112](https://doi.org/10.1073/pnas.1421042112).
- [154] H. W. Kroto, J. R. Heath, S. C. O'Brien, R. F. Curl, and R. E. Smalley: C60: Buckminsterfullerene. *Nature* **318**(6042) (Nov. 1985), 162–163. doi: [10.1038/318162a0](https://doi.org/10.1038/318162a0).
- [155] T. E. Saraswati, U. H. Setiawan, M. R. Ihsan, I. Isnaeni, and Y. Herbani: The Study of the Optical Properties of C60 Fullerene in Different Organic Solvents. *Open Chemistry* **17**(1) (Dec. 2019), 1198–1212. doi: [10.1515/chem-2019-0117](https://doi.org/10.1515/chem-2019-0117).
- [156] P. Peumans and S. R. Forrest: Very-high-efficiency double-heterostructure copper phthalocyanine/C60 photovoltaic cells. *Applied Physics Letters* **79**(1) (July 2001), 126–128. doi: [10.1063/1.1384001](https://doi.org/10.1063/1.1384001).
- [157] S. Engmann, A. J. Barito, E. G. Bittle, et al.: Higher order effects in organic LEDs with sub-bandgap turn-on. *Nature Communications* **10**(1) (Jan. 2019). doi: [10.1038/s41467-018-08075-z](https://doi.org/10.1038/s41467-018-08075-z).
- [158] H. Derouiche, S. Saidi, and A. B. Mohamed: The Effect of Energy Levels of the Electron Acceptor Materials on Organic Photovoltaic Cells. *Smart Grid and Renewable Energy* **02**(03) (2011), 278–281. doi: [10.4236/sgre.2011.23031](https://doi.org/10.4236/sgre.2011.23031).
- [159] T. Golubev, D. Liu, R. Lunt, and P. Duxbury: Understanding the impact of C60 at the interface of perovskite solar cells via drift-diffusion modeling. *AIP Advances* **9**(3) (Mar. 2019), 035026. doi: [10.1063/1.5068690](https://doi.org/10.1063/1.5068690).
- [160] T. Rabenau, A. Simon, R. K. Kremer, and E. Sohmen: The energy gaps of fullerene C60 and C70 determined from the temperature dependent microwave conductivity. *Zeitschrift für Physik B Condensed Matter* **90**(1) (Mar. 1993), 69–72. doi: [10.1007/bf01321034](https://doi.org/10.1007/bf01321034).
- [161] D. Boucher and J. Howell: Solubility Characteristics of PCBM and C60. *The Journal of Physical Chemistry B* **120**(44) (Oct. 2016), 11556–11566. doi: [10.1021/acs.jpcc.6b09273](https://doi.org/10.1021/acs.jpcc.6b09273).
- [162] J. C. Hummelen, B. W. Knight, F. LePeq, et al.: Preparation and Characterization of Fulleroid and Methanofullerene Derivatives. *The Journal of Organic Chemistry* **60**(3) (Feb. 1995), 532–538. doi: [10.1021/jo00108a012](https://doi.org/10.1021/jo00108a012).
- [163] G. D. Sharma, T. S. Shanap, K. R. Patel, and M. K. El-Mansy: Photovoltaic properties of bulk heterojunction devices based on CuI-PVA as electron donor and PCBM and modified PCBM as electron acceptor. *Materials Science-Poland* **30**(1) (Mar. 2012), 10–16. doi: [10.2478/s13536-012-0003-6](https://doi.org/10.2478/s13536-012-0003-6).

- [164] A. Ergete, F. K. Sabir, Y. Li, and T. Yohannes: Effect of solvent additives and P3HT on PDTSTTz/PCBM-based bulk heterojunction solar cells. *Journal of Photonics for Energy* **5**(1) (Jan. 2015), 057209. doi: [10.1117/1.jpe.5.057209](https://doi.org/10.1117/1.jpe.5.057209).
- [165] P. P. Khlyabich, B. Burkhart, A. E. Rudenko, and B. C. Thompson: Optimization and simplification of polymer–fullerene solar cells through polymer and active layer design. *Polymer* **54**(20) (Sept. 2013), 5267–5298. doi: [10.1016/j.polymer.2013.07.053](https://doi.org/10.1016/j.polymer.2013.07.053).
- [166] Y.-J. Huang, W.-C. Lo, S.-W. Liu, et al.: Unified assay of adverse effects from the varied nanoparticle hybrid in polymer–fullerene organic photovoltaics. *Solar Energy Materials and Solar Cells* **116** (Sept. 2013), 153–170. doi: [10.1016/j.solmat.2013.03.031](https://doi.org/10.1016/j.solmat.2013.03.031).
- [167] B. Lüssem, M. Riede, and K. Leo: Doping of organic semiconductors. *physica status solidi (a)* **210**(1) (Dec. 2012), 9–43. doi: [10.1002/pssa.201228310](https://doi.org/10.1002/pssa.201228310).
- [168] F. Zhang and A. Kahn: Investigation of the High Electron Affinity Molecular Dopant F6-TCNNQ for Hole-Transport Materials. *Advanced Functional Materials* **28**(1) (Nov. 2017), 1703780. doi: [10.1002/adfm.201703780](https://doi.org/10.1002/adfm.201703780).
- [169] D. Kiefer, R. Kroon, A. I. Hofmann, et al.: Double doping of conjugated polymers with monomer molecular dopants. *Nature Materials* **18**(2) (Jan. 2019), 149–155. doi: [10.1038/s41563-018-0263-6](https://doi.org/10.1038/s41563-018-0263-6).
- [170] C. Chen, S. Zhang, S. Wu, et al.: Effect of BCP buffer layer on eliminating charge accumulation for high performance of inverted perovskite solar cells. *RSC Advances* **7**(57) (2017), 35819–35826. doi: [10.1039/c7ra06365b](https://doi.org/10.1039/c7ra06365b).
- [171] M. Li, W. Zhang, H. Wang, et al.: Effect of organic cathode interfacial layers on efficiency and stability improvement of polymer solar cells. *RSC Advances* **7**(50) (2017), 31158–31163. doi: [10.1039/c7ra04586g](https://doi.org/10.1039/c7ra04586g).
- [172] A. L. Toumi, A. Khelil, K. Tobel, et al.: On the exciton blocking layer at the interface organic/cathode in planar multiheterojunction organic solar cells. *Solid-State Electronics* **104** (Feb. 2015), 1–5. doi: [10.1016/j.sse.2014.11.006](https://doi.org/10.1016/j.sse.2014.11.006).
- [173] J. Burschka, N. Pellet, S.-J. Moon, et al.: Sequential deposition as a route to high-performance perovskite-sensitized solar cells. **499**(7458) (July 2013), 316–319. doi: [10.1038/nature12340](https://doi.org/10.1038/nature12340).
- [174] Z. Xiao, C. Bi, Y. Shao, et al.: Efficient, high yield perovskite photovoltaic devices grown by interdiffusion of solution-processed precursor stacking layers. **7**(8) (2014), 2619–2623. doi: [10.1039/c4ee01138d](https://doi.org/10.1039/c4ee01138d).
- [175] M. Xiao, F. Huang, W. Huang, et al.: A Fast Deposition-Crystallization Procedure for Highly Efficient Lead Iodide Perovskite Thin-Film Solar Cells. **53**(37) (July 2014), 9898–9903. doi: [10.1002/anie.201405334](https://doi.org/10.1002/anie.201405334).

- [176] J. Ávila, C. Momblona, P. P. Boix, M. Sessolo, and H. J. Bolink: Vapor-Deposited Perovskites: The Route to High-Performance Solar Cell Production? *1*(3) (Nov. 2017), 431–442. doi: [10.1016/j.joule.2017.07.014](https://doi.org/10.1016/j.joule.2017.07.014).
- [177] E. H. Hellen: Verifying the diode–capacitor circuit voltage decay. *71*(8) (Aug. 2003), 797–800. doi: [10.1119/1.1578070](https://doi.org/10.1119/1.1578070).
- [178] N. Courtier, G. Richardson, and J. Foster: A fast and robust numerical scheme for solving models of charge carrier transport and ion vacancy motion in perovskite solar cells. *Applied Mathematical Modelling* **63** (Nov. 2018), 329–348. doi: [10.1016/j.apm.2018.06.051](https://doi.org/10.1016/j.apm.2018.06.051).
- [179] N. E. Courtier, J. M. Foster, S. E. J. O’Kane, A. B. Walker, and G. Richardson: Systematic derivation of a surface polarisation model for planar perovskite solar cells. *European Journal of Applied Mathematics* **30**(3) (Apr. 2018), 427–457. doi: [10.1017/s0956792518000207](https://doi.org/10.1017/s0956792518000207).
- [180] R. D. Skeel and M. Berzins: A Method for the Spatial Discretization of Parabolic Equations in One Space Variable. *11*(1) (Jan. 1990), 1–32. doi: [10.1137/0911001](https://doi.org/10.1137/0911001).
- [181] P. K. Mogensen, K. Carlsson, S. Villemot, et al.: *JuliaNLSolvers/NLsolve.jl: v4.5.1*. 2020. doi: [10.5281/ZENODO.4404703](https://doi.org/10.5281/ZENODO.4404703).
- [182] A. H. Gebremedhin, F. Manne, and A. Pothen: What Color Is Your Jacobian? Graph Coloring for Computing Derivatives. *47*(4) (Jan. 2005), 629–705. doi: [10.1137/s0036144504444711](https://doi.org/10.1137/s0036144504444711).
- [183] J. Revels, M. Lubin, and T. Papamarkou: Forward-Mode Automatic Differentiation in Julia. *arXiv:1607.07892 [cs.MS]* (2016).
- [184] M. Fischer: *AnnA.jl*. Version 0.3.0. July 2021. doi: [10.5281/zenodo.4733024](https://doi.org/10.5281/zenodo.4733024).
- [185] C. Rackauckas and Q. Nie: Differentialequations.jl—a performant and feature-rich ecosystem for solving differential equations in julia. *Journal of Open Research Software* **5**(1) (2017).
- [186] J. Lang and J. Verwer: *An Accurate Third-Order Rosenbrock Solver Designed for Parabolic Problems*. 2001, pp. 731–738. doi: [10.1023/a:1021900219772](https://doi.org/10.1023/a:1021900219772).
- [187] G. Steinebach: Improvement of Rosenbrock-Wanner Method RODASP. *Progress in Differential-Algebraic Equations II*. Springer International Publishing, 2020, 165–184. doi: [10.1007/978-3-030-53905-4_6](https://doi.org/10.1007/978-3-030-53905-4_6).
- [188] G. Di Marzo: RODAS5 (4)-Méthodes de Rosenbrock d’ordre 5 (4) adaptées aux problèmes différentiels-algébriques. *MSc Mathematics Thesis* (1993).
- [189] L. F. Shampine and M. W. Reichelt: The matlab ode suite. *SIAM journal on scientific computing* **18**(1) (1997), 1–22.

- [190] E. Hairer and G. Wanner: Stiff differential equations solved by Radau methods. *Journal of Computational and Applied Mathematics* **111**(1-2) (1999), 93–111.
- [191] O. Almora, C. Aranda, E. Mas-Marzá, and G. Garcia-Belmonte: On Mott-Schottky analysis interpretation of capacitance measurements in organometal perovskite solar cells. *Applied Physics Letters* **109**(17) (Oct. 2016), 173903. doi: [10.1063/1.4966127](https://doi.org/10.1063/1.4966127).
- [192] D. Meggiolaro, S. G. Motti, E. Mosconi, et al.: Iodine chemistry determines the defect tolerance of lead-halide perovskites. *Energy & Environmental Science* **11**(3) (2018), 702–713. doi: [10.1039/c8ee00124c](https://doi.org/10.1039/c8ee00124c).
- [193] E. Mosconi and F. D. Angelis: Mobile Ions in Organohalide Perovskites: Interplay of Electronic Structure and Dynamics. *ACS Energy Letters* **1**(1) (June 2016), 182–188. doi: [10.1021/acseenergylett.6b00108](https://doi.org/10.1021/acseenergylett.6b00108).
- [194] T. S. Sherkar, C. Momblona, L. Gil-Escrig, H. J. Bolink, and L. J. A. Koster: Improving Perovskite Solar Cells: Insights From a Validated Device Model. *Advanced Energy Materials* **7**(13) (Feb. 2017), 1602432. doi: [10.1002/aenm.201602432](https://doi.org/10.1002/aenm.201602432).
- [195] R. A. Belisle, W. H. Nguyen, A. R. Bowring, et al.: Interpretation of inverted photocurrent transients in organic lead halide perovskite solar cells: proof of the field screening by mobile ions and determination of the space charge layer widths. *Energy & Environmental Science* **10**(1) (2017), 192–204. doi: [10.1039/c6ee02914k](https://doi.org/10.1039/c6ee02914k).
- [196] W. Tress, N. Marinova, T. Moehl, et al.: Understanding the rate-dependent J–V hysteresis, slow time component, and aging in CH₃NH₃PbI₃ perovskite solar cells: the role of a compensated electric field. *Energy & Environmental Science* **8**(3) (2015), 995–1004. doi: [10.1039/c4ee03664f](https://doi.org/10.1039/c4ee03664f).
- [197] S. van Reenen, M. Kemerink, and H. J. Snaith: Modeling Anomalous Hysteresis in Perovskite Solar Cells. *The Journal of Physical Chemistry Letters* **6**(19) (Sept. 2015), 3808–3814. doi: [10.1021/acs.jpcllett.5b01645](https://doi.org/10.1021/acs.jpcllett.5b01645).
- [198] R. Gottesman, E. Haltzi, L. Gouda, et al.: Extremely Slow Photoconductivity Response of CH₃NH₃PbI₃ Perovskites Suggesting Structural Changes under Working Conditions. *The Journal of Physical Chemistry Letters* **5**(15) (July 2014), 2662–2669. doi: [10.1021/jz501373f](https://doi.org/10.1021/jz501373f).
- [199] Y. Cheng, H.-W. Li, J. Qing, et al.: The detrimental effect of excess mobile ions in planar CH₃NH₃PbI₃ perovskite solar cells. *Journal of Materials Chemistry A* **4**(33) (2016), 12748–12755. doi: [10.1039/c6ta05053k](https://doi.org/10.1039/c6ta05053k).
- [200] A. Zohar, M. Kulbak, I. Levine, et al.: What Limits the Open-Circuit Voltage of Bromide Perovskite-Based Solar Cells? *ACS Energy Letters* **4**(1) (Nov. 2018), 1–7. doi: [10.1021/acseenergylett.8b01920](https://doi.org/10.1021/acseenergylett.8b01920).

- [201] Y. Zhang, M. Liu, G. E. Eperon, et al.: Charge selective contacts, mobile ions and anomalous hysteresis in organic–inorganic perovskite solar cells. *Materials Horizons* **2**(3) (2015), 315–322. doi: [10.1039/c4mh00238e](https://doi.org/10.1039/c4mh00238e).
- [202] A. Senocrate, I. Moudrakovski, G. Y. Kim, et al.: The Nature of Ion Conduction in Methylammonium Lead Iodide: A Multimethod Approach. *Angewandte Chemie International Edition* **56**(27) (May 2017), 7755–7759. doi: [10.1002/anie.201701724](https://doi.org/10.1002/anie.201701724).
- [203] A. Senocrate, T.-Y. Yang, G. Gregori, et al.: Charge carrier chemistry in methylammonium lead iodide. *Solid State Ionics* **321** (Aug. 2018), 69–74. doi: [10.1016/j.ssi.2018.03.029](https://doi.org/10.1016/j.ssi.2018.03.029).
- [204] D. Li, F. Sun, C. Liang, and Z. He: Effective approach for reducing the migration of ions and improving the stability of organic–inorganic perovskite solar cells. *Journal of Alloys and Compounds* **741** (Apr. 2018), 489–494. doi: [10.1016/j.jallcom.2018.01.082](https://doi.org/10.1016/j.jallcom.2018.01.082).
- [205] M. Salado, L. Contreras-Bernal, L. Calìò, et al.: Impact of moisture on efficiency-determining electronic processes in perovskite solar cells. *Journal of Materials Chemistry A* **5**(22) (2017), 10917–10927. doi: [10.1039/c7ta02264f](https://doi.org/10.1039/c7ta02264f).
- [206] S. Ravishankar, S. Gharibzadeh, C. Roldán-Carmona, et al.: Influence of Charge Transport Layers on Open-Circuit Voltage and Hysteresis in Perovskite Solar Cells. *Joule* **2**(4) (Apr. 2018), 788–798. doi: [10.1016/j.joule.2018.02.013](https://doi.org/10.1016/j.joule.2018.02.013).
- [207] A. Baumann, K. Tvingstedt, M. C. Heiber, et al.: Persistent photovoltage in methylammonium lead iodide perovskite solar cells. *APL Materials* **2**(8) (Aug. 2014), 081501. doi: [10.1063/1.4885255](https://doi.org/10.1063/1.4885255).
- [208] R. Gottesman, P. Lopez-Varo, L. Gouda, et al.: Dynamic Phenomena at Perovskite/Electron-Selective Contact Interface as Interpreted from Photovoltage Decays. *Chem* **1**(5) (Nov. 2016), 776–789. doi: [10.1016/j.chempr.2016.10.002](https://doi.org/10.1016/j.chempr.2016.10.002).
- [209] A. Pockett, G. E. Eperon, T. Peltola, et al.: Characterization of Planar Lead Halide Perovskite Solar Cells by Impedance Spectroscopy, Open-Circuit Photovoltage Decay, and Intensity-Modulated Photovoltage/Photocurrent Spectroscopy. *The Journal of Physical Chemistry C* **119**(7) (Feb. 2015), 3456–3465. doi: [10.1021/jp510837q](https://doi.org/10.1021/jp510837q).
- [210] S. Lederhandler and L. Giacoletto: Measurement of Minority Carrier Lifetime and Surface Effects in Junction Devices. *Proceedings of the IRE* **43**(4) (1955), 477–483. doi: [10.1109/jrproc.1955.277857](https://doi.org/10.1109/jrproc.1955.277857).
- [211] A. Zaban, M. Greenshtein, and J. Bisquert: Determination of the Electron Lifetime in Nanocrystalline Dye Solar Cells by Open-Circuit Voltage Decay Measurements. *ChemPhysChem* **4**(8) (Aug. 2003), 859–864. doi: [10.1002/cphc.200200615](https://doi.org/10.1002/cphc.200200615).

- [212] D. Kiermasch, A. Baumann, M. Fischer, V. Dyakonov, and K. Tvingstedt: Revisiting lifetimes from transient electrical characterization of thin film solar cells; a capacitive concern evaluated for silicon, organic and perovskite devices. *Energy & Environmental Science* **11**(3) (2018), 629–640. doi: [10.1039/c7ee03155f](https://doi.org/10.1039/c7ee03155f).
- [213] J. Mahan and D. Barnes: Depletion layer effects in the open-circuit- voltage-decay lifetime measurement. *Solid-State Electronics* **24**(10) (Oct. 1981), 989–994. doi: [10.1016/0038-1101\(81\)90124-6](https://doi.org/10.1016/0038-1101(81)90124-6).
- [214] A. Pockett, G. E. Eperon, N. Sakai, et al.: Microseconds, milliseconds and seconds: deconvoluting the dynamic behaviour of planar perovskite solar cells. *Physical Chemistry Chemical Physics* **19**(8) (2017), 5959–5970. doi: [10.1039/c6cp08424a](https://doi.org/10.1039/c6cp08424a).
- [215] O. J. Sandberg, K. Tvingstedt, P. Meredith, and A. Armin: Theoretical Perspective on Transient Photovoltage and Charge Extraction Techniques. *The Journal of Physical Chemistry C* **123**(23) (May 2019), 14261–14271. doi: [10.1021/acs.jpcc.9b03133](https://doi.org/10.1021/acs.jpcc.9b03133).
- [216] C. Deibel, A. Wagenpfahl, and V. Dyakonov: Origin of reduced polaron recombination in organic semiconductor devices. *Physical Review B* **80**(7) (Aug. 2009). doi: [10.1103/physrevb.80.075203](https://doi.org/10.1103/physrevb.80.075203).
- [217] T. Kirchartz and J. Nelson: Device Modelling of Organic Bulk Heterojunction Solar Cells. *Topics in Current Chemistry*. Springer Berlin Heidelberg, 2013, pp. 279–324.
- [218] W. Tress, K. Leo, and M. Riede: Optimum mobility, contact properties, and open-circuit voltage of organic solar cells: A drift-diffusion simulation study. *Physical Review B* **85**(15) (Apr. 2012). doi: [10.1103/physrevb.85.155201](https://doi.org/10.1103/physrevb.85.155201).
- [219] L. Bertoluzzi, C. C. Boyd, N. Rolston, et al.: Mobile Ion Concentration Measurement and Open-Access Band Diagram Simulation Platform for Halide Perovskite Solar Cells. *Joule* **4**(1) (Jan. 2020), 109–127. doi: [10.1016/j.joule.2019.10.003](https://doi.org/10.1016/j.joule.2019.10.003).
- [220] D. Li, L. Song, Y. Chen, and W. Huang: Modeling Thin Film Solar Cells: From Organic to Perovskite. *Advanced Science* **7**(1) (Nov. 2019), 1901397. doi: [10.1002/advs.201901397](https://doi.org/10.1002/advs.201901397).
- [221] T. S. Sherkar, C. Momblona, L. Gil-Escrig, et al.: Recombination in Perovskite Solar Cells: Significance of Grain Boundaries, Interface Traps, and Defect Ions. *ACS Energy Letters* **2**(5) (May 2017), 1214–1222. doi: [10.1021/acsenergylett.7b00236](https://doi.org/10.1021/acsenergylett.7b00236).
- [222] B. Krogmeier, F. Staub, D. Grabowski, U. Rau, and T. Kirchartz: Quantitative analysis of the transient photoluminescence of CH₃NH₃PbI₃/PC₆₁BM heterojunctions by numerical simulations. *Sustainable Energy & Fuels* **2**(5) (2018), 1027–1034. doi: [10.1039/c7se00603a](https://doi.org/10.1039/c7se00603a).

- [223] M. T. Neukom, A. Schiller, S. Züfle, et al.: Consistent Device Simulation Model Describing Perovskite Solar Cells in Steady-State, Transient, and Frequency Domain. *ACS Applied Materials & Interfaces* **11**(26) (June 2019), 23320–23328. doi: [10.1021/acsami.9b04991](https://doi.org/10.1021/acsami.9b04991).
- [224] S. E. J. O’Kane, G. Richardson, A. Pockett, et al.: Measurement and modelling of dark current decay transients in perovskite solar cells. *Journal of Materials Chemistry C* **5**(2) (2017), 452–462. doi: [10.1039/c6tc04964h](https://doi.org/10.1039/c6tc04964h).
- [225] G. Richardson, S. E. J. O’Kane, R. G. Niemann, et al.: Can slow-moving ions explain hysteresis in the current–voltage curves of perovskite solar cells? *Energy & Environmental Science* **9**(4) (2016), 1476–1485. doi: [10.1039/c5ee02740c](https://doi.org/10.1039/c5ee02740c).
- [226] J. Bezanson, A. Edelman, S. Karpinski, and V. B. Shah: Julia: A fresh approach to numerical computing. *SIAM Review* **59**(1) (Sept. 2017), 65–98. doi: [10.1137/141000671](https://doi.org/10.1137/141000671).
- [227] T. Kirchartz, J. A. Márquez, M. Stolterfoht, and T. Unold: PhotoluminescenceBased Characterization of Halide Perovskites for Photovoltaics. *Advanced Energy Materials* **10**(26) (May 2020), 1904134. doi: [10.1002/aenm.201904134](https://doi.org/10.1002/aenm.201904134).
- [228] K. Tvingstedt, O. Malinkiewicz, A. Baumann, et al.: Radiative efficiency of lead iodide based perovskite solar cells. *Scientific Reports* **4**(1) (Aug. 2014). doi: [10.1038/srep06071](https://doi.org/10.1038/srep06071).
- [229] Y. Zhai, K. Wang, F. Zhang, et al.: Individual Electron and Hole Mobilities in Lead-Halide Perovskites Revealed by Noncontact Methods. *ACS Energy Letters* **5**(1) (Nov. 2019), 47–55. doi: [10.1021/acsenenergylett.9b02310](https://doi.org/10.1021/acsenenergylett.9b02310).
- [230] P. Löper, M. Stuckelberger, B. Niesen, et al.: Complex Refractive Index Spectra of CH₃NH₃PbI₃ Perovskite Thin Films Determined by Spectroscopic Ellipsometry and Spectrophotometry. *The Journal of Physical Chemistry Letters* **6**(1) (Dec. 2014), 66–71. doi: [10.1021/jz502471h](https://doi.org/10.1021/jz502471h).
- [231] J. N. Wilson, J. M. Frost, S. K. Wallace, and A. Walsh: Dielectric and ferroic properties of metal halide perovskites. *APL Materials* **7**(1) (Jan. 2019), 010901. doi: [10.1063/1.5079633](https://doi.org/10.1063/1.5079633).
- [232] D. Kiermasch, L. Gil-Escrig, A. Baumann, et al.: Unravelling steady-state bulk recombination dynamics in thick efficient vacuum-deposited perovskite solar cells by transient methods. *Journal of Materials Chemistry A* **7**(24) (2019), 14712–14722. doi: [10.1039/c9ta04367e](https://doi.org/10.1039/c9ta04367e).
- [233] M. Stolterfoht, P. Caprioglio, C. M. Wolff, et al.: The impact of energy alignment and interfacial recombination on the internal and external open-circuit voltage of perovskite solar cells. *Energy & Environmental Science* **12**(9) (2019), 2778–2788. doi: [10.1039/c9ee02020a](https://doi.org/10.1039/c9ee02020a).

- [234] U. Würfel, A. Cuevas, and P. Würfel: Charge Carrier Separation in Solar Cells. *IEEE Journal of Photovoltaics* **5**(1) (Jan. 2015), 461–469. doi: [10.1109/jphotov.2014.2363550](https://doi.org/10.1109/jphotov.2014.2363550).
- [235] K. Tvingstedt, L. Gil-Escrig, C. Momblona, et al.: Removing Leakage and Surface Recombination in Planar Perovskite Solar Cells. *ACS Energy Letters* **2**(2) (Jan. 2017), 424–430. doi: [10.1021/acsenergylett.6b00719](https://doi.org/10.1021/acsenergylett.6b00719).
- [236] T.-H.-Y. Vu, W. Chen, X. Deng, et al.: Visualizing the Impact of Light Soaking on Morphological Domains in an Operational Cesium Lead Halide Perovskite Solar Cell. *The Journal of Physical Chemistry Letters* **11**(1) (Dec. 2019), 136–143. doi: [10.1021/acs.jpcclett.9b03210](https://doi.org/10.1021/acs.jpcclett.9b03210).
- [237] D. Kim, J. S. Yun, P. Sharma, et al.: Light- and bias-induced structural variations in metal halide perovskites. *Nature Communications* **10**(1) (Jan. 2019). doi: [10.1038/s41467-019-08364-1](https://doi.org/10.1038/s41467-019-08364-1).
- [238] S. T. Birkhold, J. T. Precht, H. Liu, et al.: Interplay of Mobile Ions and Injected Carriers Creates Recombination Centers in Metal Halide Perovskites under Bias. *ACS Energy Letters* **3**(6) (May 2018), 1279–1286. doi: [10.1021/acsenergylett.8b00505](https://doi.org/10.1021/acsenergylett.8b00505).
- [239] M. H. Futscher, J. M. Lee, L. McGovern, et al.: Quantification of ion migration in CH₃NH₃PbI₃ perovskite solar cells by transient capacitance measurements. *Materials Horizons* **6**(7) (2019), 1497–1503. doi: [10.1039/c9mh00445a](https://doi.org/10.1039/c9mh00445a).
- [240] S. A. L. Weber, I. M. Hermes, S.-H. Turren-Cruz, et al.: How the formation of interfacial charge causes hysteresis in perovskite solar cells. *Energy & Environmental Science* **11**(9) (2018), 2404–2413. doi: [10.1039/c8ee01447g](https://doi.org/10.1039/c8ee01447g).
- [241] T. Heiser and A. Mesli: Determination of the copper diffusion coefficient in silicon from transient ion-drift. *Applied Physics A Solids and Surfaces* **57**(4) (Oct. 1993), 325–328. doi: [10.1007/bf00332285](https://doi.org/10.1007/bf00332285).
- [242] J. R. Macdonald: Theory of ac Space-Charge Polarization Effects in Photoconductors, Semiconductors, and Electrolytes. *Physical Review* **92**(1) (Oct. 1953), 4–17. doi: [10.1103/physrev.92.4](https://doi.org/10.1103/physrev.92.4).
- [243] R. J. Klein, S. Zhang, S. Dou, et al.: Modeling electrode polarization in dielectric spectroscopy: Ion mobility and mobile ion concentration of single-ion polymer electrolytes. *The Journal of Chemical Physics* **124**(14) (Apr. 2006), 144903. doi: [10.1063/1.2186638](https://doi.org/10.1063/1.2186638).

Abbreviations

Materials

Abrev.	Name	IUPAC Name / Sum. Formular	Page
C ₆₀	Buckminsterfullerene	C ₆₀	37
CaTiO ₃	Calcium titanate	CaTiO ₃	5
CdTe	Cadmium telluride	CdTe	4
CH ₄	Methane	CH ₄	1
CIGS	Copper indium gallium (di)selenide	CuIn _x Ga _{1-x} Se ₂	4
CO ₂	Carbon dioxide	CO ₂	1
FAI	Formamidinium iodide	CH ₅ NI	41
FAPbI ₃	Formamidinium lead iodide	CH ₅ N ₂ PbI ₃	40
FA / FA ⁺	Formamidinium (cation)	[CH ₅ N ₂] ⁺	40
GaAs	Gallium arsenide	GaAs	4
MAI	Methylammonium iodide	CH ₃ NH ₃ I	40
MAPbBr ₃	Methylammonium lead bromide	CH ₃ NH ₃ PbBr ₃	7
MAPbI ₃	Methylammonium lead iodide	CH ₃ NH ₃ PbI ₃	6
MA / MA ⁺	Methylammonium (cation)	[CH ₃ NH ₃] ⁺	10
PbI ₂	Lead(II) iodide	PbI ₂	40
Si	Silicon	Si	3
TiO ₂	Titanium dioxide	TiO ₂	14
Au	Gold	Au	42
BCP	Bathocuproin	2,9-Dimethyl-4,7-diphenyl-1,10-phenanthroline	38
CB	Chlorbenzene	C ₆ H ₅ Cl	41
DCB	Dichlorbenzene	C ₆ H ₄ Cl ₂	42
DMF	Dimethylformamide	C ₃ H ₇ NO	40
DMSO	Dimethyl sulfoxide	C ₂ H ₆ OS	40
F6-TCNQ	2,2'-(Perfluoronaphthalene-2,6-diylidene) dimalononitrile	2,2'-(perfluoronaphthalene-2,6-diylidene) dimalononitrile	38
FTO	Fluorine doped tin oxide		14
ITO	Indium tin oxide	[In ₂ O ₃] _x [SnO ₂] _{1-x}	14
PC ₆₁ BM	[6,6]-Phenyl-C ₆₁ -butyric acid methyl ester	[6,6]-Phenyl-C ₆₁ -butyric acid methyl ester	37
PhIm	N1,N4-bis(tri-p-tolylphosphoranylidene) benzene-1,4-diamine	N1,N4-bis(tri-p-tolylphosphoranylidene) benzene-1,4-diamine	38

Abrev.	Name	IUPAC Name / Sum. Formular	Page
PTAA	Poly[bis(4-phenyl)(2,4,6-trimethylphenyl)amine]	Poly[bis(4-phenyl)(2,4,6-trimethylphenyl)amine]	36
TaTm	N ₄ ,N ₄ ,N ₄ '',N ₄ '-tetra([1,10-biphenyl]-4-yl)-[1,1':4',1''-terphenyl]-4,4''-diamine	N ₄ ,N ₄ ,N ₄ '',N ₄ '-tetra([1,10-biphenyl]-4-yl)-[1,1':4',1''-terphenyl]-4,4''-diamine	36

Symbols

Symbol	Description	Unit	Page
α	Absorption coefficient	m^{-1}	52
ΔE_E	Electron energy barrier at the ETM-perovskite interface	eV	80
ΔE_H	Hole energy barrier at the HTM-perovskite interface	eV	80
\hat{N}	Charge carrier density	cm^{-3}	50
\hat{n}	Effective n -doping concentration	m^{-3}	50
\hat{p}	Effective p -doping concentration	m^{-3}	50
λ_D	Debye length	m	93
μ	Mobility	$\text{cm}^2 \text{V}^{-1} \text{s}^{-1}$	9
μ_O	Octahedral factor		6
μ_{ion}	Ionic mobility	$\text{cm}^2 \text{V}^{-1} \text{s}^{-1}$	9
ν_d	Drift velocity	m s^{-1}	50
ν_{ion}	Ionic (diffusion) velocity	m s^{-1}	93
ν_n	Electron recombination velocity	m s^{-1}	25
ν_p	Hole recombination velocity	m s^{-1}	25
ω	Angular frequency	s^{-1}	43
Φ	Electrostatic potential	V	50
Φ_{BI}	Built in potential	V	52
σ_{ion}	Ionic conductivity	$\text{m}^2 \Omega^{-1}$	9
τ_{ion}	Characteristic time constant of the ionic relaxation	s	93
ϵ	Dielectric constant	F m^{-1}	50
ϵ_E	Relative permittivity of the ETM		54
ϵ_H	Relative permittivity of the HTM		54
ϵ_P	Relative permittivity of perovskite		54
A	Area	m^2	44
C	Capacitance	F	30
C_p	Parallel capacitance	F	46
C_s	Series capacitance	F	
d	Layer thickness	m	44
D	Diffusion coefficient	$\text{m}^2 \text{s}^{-1}$	9
d_E	ETM layer thickness	m	51

Symbol	Description	Unit	Page
d_H	HTM layer thickness	m	51
D_n	Electron diffusion coefficient	$\text{m}^2 \text{s}^{-1}$	25
D_p	Hole diffusion coefficient	$\text{m}^2 \text{s}^{-1}$	25
D_{det}	Calculated (determined) diffusivity resulting from $C(t)$ peak position and Equation 6.2	$\text{m}^2 \text{s}^{-1}$	94
D_{ion}	Ionic diffusivity	$\text{m}^2 \text{s}^{-1}$	9
D_{ion}^0	Ionic diffusion constant	$\text{m}^2 \text{s}^{-1}$	9
E_C	Energy conduction band minimum	eV	19
E_g	Band gap energy	eV	7
E_V	Energy of valence band maximum	eV	19
E_{F_n}	Electron quasi Fermi level	eV	20
E_{F_p}	Hole quasi Fermi level	eV	20
E_F	Fermi level	eV	19
E_{ion}^D	Activation energy of ionic diffusion	eV	9
E_{ion}^F	Formation energy of ionic vacancies	eV	9
f	Ordinary frequency	Hz	
F_{ph}	Irradiated photon flux	$\text{m}^{-2} \text{s}^{-1}$	52
F_{ph}^0	Photon flux from AM1.5 irradiation	$\text{m}^{-2} \text{s}^{-1}$	54
G_{ph}	Photon induced generation rate	$\text{cm}^{-3} \text{s}^{-1}$	27
G_{th}	Thermal charge carrier generation rate	$\text{cm}^{-3} \text{s}^{-1}$	22
I	Current	A	43
I_C	Capacitive current	A	30
j_0	Dark saturation current density	A cm^{-2}	27
j_n	Electron current density	A cm^{-2}	
j_P	Ionic current density	A cm^{-2}	
j_p	Hole current density	A cm^{-2}	
j_d	Dark current density	A cm^{-2}	79
j_{SC}	Short circuit current density	A cm^{-2}	27
k_{rad}	Radiative rate constant	$\text{cm}^{-3} \text{s}^{-1}$	22
k_{rad}^{ext}	External radiative rate constant	$\text{cm}^{-3} \text{s}^{-1}$	23
k_{rad}^{int}	Internal radiative rate constant	$\text{cm}^{-3} \text{s}^{-1}$	23
m_e^*	Effective electron mass	m_0	
m_h^*	Effective hole mass	m_0	
m_{eff}^*	Joint effective mass	m_0	12
N	Number of grid points in perovskite layer		54
N_C	Conduction band effective density of states	cm^{-3}	20

Symbol	Description	Unit	Page
N_L	Density of lattice sites	cm^{-3}	9
N_V	Valence band effective density of states	cm^{-3}	20
n_0	Electron density in thermal equilibrium	cm^{-2}	19
N_{det}	Calculated (determined) ionic densities resulting from $C(V)$ integration	cm^{-3}	
n_{id}	Diode ideality factor		27
N_{ion}	Density of mobile ionic charge carrier	cm^{-3}	9
n_i	Intrinsic carrier concentration	cm^{-2}	19
N_{SC}	Space charge concentration	cm^{-3}	65
p_0	Hole density in thermal equilibrium	cm^{-3}	19
Q	Total number of charge	C	88
$q_{\{A,B,X\}}$	Charge of the A, B or X ion	q	6
R	Excess charge carrier recombination rate	$\text{m}^{-3} \text{s}^{-1}$	21
R_P	Parallel resistance	Ωcm^2	27
R_S	Series resistance	Ωcm^2	27
$r_{\{A,B,X\}}$	Radius of the A, B or X ion	m	6
R_{rad}	Radiative charge carrier recombination rate	$\text{cm}^{-3} \text{s}^{-1}$	
R_{sur}	Surface recombination flux	$\text{cm}^{-2} \text{s}^{-1}$	25
T	Temperature	K	9
t_G	Goldschmidt tolerance factor		6
t_{on}	On time	s	46
V	Voltage	cm^{-3}	26
V_{BI}	Built-in potential in Volts	V	65
V_{OC}	Open circuit voltage	V	26
Z	Complex impedance	Ω	43
N_L'	Density of interstitial sites	cm^{-3}	9

Constants

Symbol	Description	Value	Page
k_B	Boltzmann constant	$8.617\,333\,262\,145 \times 10^{-5} \text{ eV K}^{-1}$	9
q	Elementary charge	$1.602\,176\,634 \times 10^{-19} \text{ C}$	9
m_0	Free electron mass	$9.109\,383\,701\,5 \times 10^{-31} \text{ kg}$	12
c	Speed of light in vacuum	$299\,792\,458 \text{ m s}^{-1}$	17
h	Plank's constant	$4.135\,667\,696 \times 10^{-15} \text{ eV Hz}^{-1}$	17
\hbar	Reduced Plank's constant	$6.582\,119\,569 \times 10^{-16} \text{ eV s}$	12
ϵ_0	Vacuum permittivity	$8.854\,187\,812\,8 \times 10^{-12} \text{ F m}^{-1}$	44

Publications and Conference Contribution



Peer-reviewed Publications

- D. Kiermasch, **M. Fischer**, L. Gil-Escrig, A. Baumann, H.J. Bolink, V. Dyakonov and K. Tvingstedt. Reduced Recombination Losses in Evaporated Perovskite Solar Cells by Postfabrication Treatment. *Solar RRL*, 5: 2100400. (2021)
DOI: [10.1002/solr.202100400](https://doi.org/10.1002/solr.202100400)
- **M. Fischer**, D. Kiermasch, L. Gil-Escrig, H. J. Bolink, V. Dyakonov and K. Tvingstedt. Assigning ionic properties in perovskite solar cells; a unifying transient simulation/experimental study. *Sustainable Energy Fuels*, 5, 3578 (2021)
DIO: [10.1039/d1se00369k](https://doi.org/10.1039/d1se00369k)
- J. Höcker, M. Ozcan, S. Hammer, **M. Fischer**, B. Bichler, M. Armer, P. Rieder, V. Drach, J. Pflaum, B. Nickel and V. Dyakonov. Seed crystal free growth of high-quality double cation - double halide perovskite single crystals for optoelectronic applications. *Journal of Materials Chemistry C*, 8 ,24, 8275-8283, (2020)
DOI: [10.1039/D0TC01617A](https://doi.org/10.1039/D0TC01617A)
- V. M. Caselli, **M. Fischer**, D. Meggiolaro, E. Mosconi, F. De Angelis, S. D. Stranks, A. Baumann, V. Dyakonov, E. M. Hutter, T. J. Savenije. Charge Carriers Are Not Affected by the Relatively Slow-Rotating Methylammonium Cations in Lead Halide Perovskite Thin Films. *The journal of physical chemistry letters*, 10, 17, 5128-5134, (2019)
DOI: [10.1021/acs.jpcllett.9b02160](https://doi.org/10.1021/acs.jpcllett.9b02160)
- **M. Fischer**, K. Tvingstedt, A. Baumann and V. Dyakonov. Doping Profile in Planar Hybrid Perovskite Solar Cells Identifying Mobile Ions. *ACS Applied Energy Materials*, 1, 10, 5129-5134, (2018)
DIO: [10.1021/acsaem.8b01119](https://doi.org/10.1021/acsaem.8b01119)

- D. Kiermasch, A. Baumann, **M. Fischer**, V. Dyakonov and K. Tvingstedt. Revisiting lifetimes from transient electrical characterization of thin film solar cells; a capacitive concern evaluated for silicon, organic and perovskite devices. *Energy Environmental Science*, 11, 629-640, (2018)
DOI:[10.1039/c7ee03155f](https://doi.org/10.1039/c7ee03155f)

Danksagung

B

Es war nicht immer klar, dass mein Leben diesen Pfad einschlagen würde, daher möchte ich an dieser Stelle meinem tiefen Wunsch nach gehen, etlichen Personen die dies ermöglicht haben meinen Dank aus zu sprechen.

- Prof. Dr. Vladimir Dyakonov für die Möglichkeit am Lehrstuhl für Experimentelle Physik VI meine Promotion durch zu führen. Die äußerst fruchtbare Umgebung, vertrauensvolle Zusammenarbeit und herausragende Betreuung die ich hier vorfand, bildeten ein verlässliches Fundament für dieses Unterfangen. Dein Input zu Publikationen so wie die zahlreichen Diskussionsrunden mit dir waren von unschätzbarem Wert dies gilt insbesondere auch für die unbequemen Fragen die du zu stellen vermochtest. Aber vor allem möchte ich dir für die Freiheiten und Geduld insbesondere auch bei explorativen und schwierigen Themen aufbrachtest danken, ich weiß das wirklich zu schätzen. Die Zeit mit und bei dir war mir eine große Freude und Lebensinhalt zu gleich!
- Dr. Kristofer Tvingstedt für wissenschaftliche Expertise auf dem Feld der Photovoltaik. Ich möchte dir Danken dass du mir gezeigt hast wie lohnend und notwendig zu gleich es ist auch die kleinen Details vollumfänglich verstehen zu wollen. Ich habe die Unterhaltung mir dir im Fachlichen wie Privatem immer sehr genossen.
- Dr. Andreas Baumann der es stets verstand mich zu motivieren und auch in augenscheinlichen Fehlschlägen die Chancen zu sehen. Danke für diene ansteckende Begeisterungsfähigkeit und dein weit über deine Pflichten hinaus reichendes Engagement.
- Philipp Rieder, Dr. David Kiermarsch, Dr. Julian Höcker, Patrick Dörflinger, Melina Armer. Ich wahrte die letzten Jahre verlässliche Begleiter und Unterstützer im Labor, Büro und überhaupt im Alltagsgeschäft. Auf eure Unterstützung im kleinen wie im Großen auf war stets verlass.

- André Thiem-Riebe und Diep Phan die beiden Seelen bei denen ich schon zur Zeit meiner Bachelor Arbeit dafür dankbar war, dass sie die technische und organisatorische Kerninfrastruktur des Lehrstuhl bereit stellen und am Laufen halten. Ohne euch wäre ich sicher nicht in der Lage gewesen den Alltag so meistern wie es erforderlich gewesen wäre, danke!
- Danke auch an alle die Bachelor und Masterstudenten für eure zuarbeiten. Florian Schwarz, Markus Jakob, Jonathan Henzel und Valentin Schmid für eure gute und kurzweilige Unterstützung.
- Dr. Andreas Sperlich, Valentin Baianov, Stephan Braxmeier und Jens Pflaum. Ihr wahrt stets eine verlässliche, engagierte und kompetente Anlaufstelle für die verschiedensten Fragestellungen die einem mal so durch den Kopf gehen.
- Udo Dölling der ganz genau weiß wofür.

Wann immer man sich im Leben wieder sieht, ich kann diesen Moment kaum erwarten! Der finale Danke geht natürlich an meine Familie. An meine Eltern für die unendliche Geduld und die stets verlässliche und bedingungslose Unterstützung auf die ich mich immer verlassen konnte und ohne deren Entbehrungen dieses Schriftstück niemals entstanden wäre. Meinem Bruder dessen Hilfsbereitschaft immer willkommen ist. Meiner Schwester welche sich nie zu schade war mir einen Gefallen zu erfüllen, auch wenn er noch so einer Strafarbeit glich. Einen riesiger Dank geht an meine Frau die sich in den letzten Jahren so manches von mir gefallen lassen musste und ich mir dennoch stets ihrer Unterstützung sicher sein konnte. Anna du bist mir Hafen und Schiff zu gleich... ich liebe dich! Dann wären da noch meine beiden Kinder, welche mich ständig daran erinnern haben, dass andere Dinge auch wichtig sind wodurch es mir vergönnt war diese Promotion in voller Länge zu genießen.